Elisabete Dinora Caldas de Freitas

Studies on high pressure xenon scintillation and photosensor alternatives for the NEXT experiment

Trabalho realizado sob a orientação do
Professor Doutor Joaquim Marques Ferreira dos Santos
e do Doutor Luís Manuel Panchorrinha Fernandes

2013

Universidade de Coimbra

Elisabete Dinora Caldas de Freitas

Studies on high pressure xenon scintillation and photosensor alternatives for the NEXT experiment

Dissertation submitted to Faculdade de Ciências e Tecnologia da Universidade de Coimbra for the degree of *Phylosophiae Doctor* in Technological Physics, under the supervision of Prof. Dr. Joaquim Marques Ferreira dos Santos and of Dr. Luís Manuel Panchorrinha Fernandes

2013

UNIVERSIDADE DE COIMBRA

This work was supported by *Fundação para a Ciência e Tecnologia* and by the European Social Fund, through *Programa Operacional Potencial Humano* (POHP) through the grant SFRH / BD / 46711 / 2008.

To my parents

to Inês

ACKNOWLEDGEMENTS

First and foremost I would like to thank Professor Dr. Joaquim Marques Ferreira dos Santos for his orientation. He took me into the group when I was an undergraduate student and had no research experience. He has been a constant source of advice and encouragement throughout the years.

To Doctor Luís Manuel Panchorrinha Fernandes for his orientation, insightful discussions, suggestions and friendship throughout the present work.

To Doctor Juan José Gómez-Cadenas and NEXT Collaboration, for accepting me as a member of the collaboration.

To all the colleagues, within the *Grupo de Instrumentação Atómica e Nuclear*, for their friendship and solidarity that made GIAN a successful and excellent working place. Special thanks to João Veloso, José Matias, Daniel Covita, Luís Fernandes, Hugo Luz, Fernando Amaro, Cristina Monteiro, Artur Coimbra, Andrea Gouvea and Catalin Balan.

To all the colleagues, within the NEXT Collaboration, I had the pleasure to work with. Their availability, enthusiasm, guidance and support have allowed me to carry out the present work.

To Cris and Quim for their friendship.

To Pedro for making me believe again.

To Inês for all the rough times and difficulties that we have been through and for the time that the present work may have stolen from us.

And especially to my parents for the effort, care and help they gave me, for believing in me and for always being present, in the good and rough times, throughout all my life.

LIST OF ABBREVIATIONS

0νββ - Neutrinoless double-beta decay

APD – Avalanche PhotoDiode

COBRA – Cadmium Zinc Telluride 0-neutrino double-Beta Research Apparatus

EL – Electroluminescence

EXO - Enriched Xenon Observatory

GERDA - GERmanium Detector Array

GIAN - Atomic and Nuclear Instrumentation Group, Coimbra, Portugal

GPSC – Gas Proportional Scintillation Counter

HPGXe – High pressure gaseous xenon

ICARUS – Imaging Cosmic And Rare Underground Signals

ICMOL - Instituto de Ciência Molecular

IFAE - Institute for High Energy Physics, Barcelona, Spain

IFIC – Instituto de Física Corpuscular, Valencia, Spain

IGEX - International Germanium Experiment

LAAPD – Large Area Avalanche Photodiode

LAr - Liquid Argon

LNGS - Gran Sasso National Laboratory

LSC - Laboratorio Subterráneo de Canfranc, Spain

LXe – Liquid Xenon

Micromegas - MICRO-MEsh-Gaseous Structure

MM - Micromegas

MPPC -Multi Pixel Photon Counter

NEMO - Neutrino Ettore Majorana Observatory

NEXT - *Neutrino Experiment with a Xenon TPC*

PDE - Photon Detection Efficiency

PMT – Photomultiplier Tube

QE – Quantum Efficiency

SiPM – Silicon photomultiplier

SNO - Sudbury Neutrino Observatory

SOFT -Separated Optimized Function for Tracking

SM – Standard Model of particle physics

THGEM – Thick Gas Electron Multiplier

TPB - Tetraphenyl Butadiene

TPC – Time Projection Chamber

UNIZAR - University of Zaragoza, Spain

VUV - Vacuum UltraViolet

WLS - Wavelength-Shifter

ABSTRACT

Neutrinoless double beta decay searches are promising experimental methods to determine the neutrino nature. If neutrinos are Majorana particles, then neutrinoless double beta decays can be observed. This has become an important topic in contemporary physics with many active experiments. Recent developments in detector technologies made the observation of this type of decay achievable with the sensitivity required to perform the experiment.

The NEXT collaboration project considers the use of a high pressure gaseous xenon TPC, based on electroluminescence, in order to search for the neutrinoless double beta decay in the ^{136}Xe isotope. The studies presented in this thesis represent a contribution to the R&D effort of the NEXT collaboration to achieve a final technology and design of the NEXT TPC.

The performance of the photosensor alternatives to use in NEXT TPC, for detection of the xenon secondary scintillation light, are presented in this work, together with xenon electroluminescence yield studies in the pressure range of 2 to 10 bar.

Two different alternatives for the energy and the tracking planes have been considered for NEXT, an electroluminescence readout using photosensors and a charge avalanche amplification readout using Micromegas. We have studied the performance obtained with a MM in pure xenon, with pressures in the range of 1-10 bar to evaluate the suitability of using a MM inside the NEXT TPC.

The photosensor studies developed in the scope of this thesis include the electroluminescence response of a Hamamatsu S8664-SPL APD and the response of Hamamatsu S10362 and S10362-SPL MPPCs to VUV light either by using direct VUV photon incidence or by using an organic wavelength shifter. The performance of the Hamamatsu R8520-06SEL Photomultiplier, also used by the XENON collaboration at cryogenic temperatures, was accessed for the detection of the primary and the secondary scintillation produced inside a GPSC, for pressures up to 3 bar, and the

possibility of calibrating PMTs inside the chamber, by using their response to single photoelectron, was evaluated.

RESUMO

A procura do decaimento duplo beta sem emissão de neutrino é um método experimental promissor para determinar a natureza do neutrino. Se os neutrinos forem partículas Majorana, então o decaimento duplo beta existe. Este assunto tornou-se num tópico importante na física contemporânea, com muitas experiências activas nesta área. Os desenvolvimentos tecnológicos recentes irão permitir que a observação deste tipo de decaimento seja possível com a sensibilidade necessária para a realização da experiência.

No projecto da colaboração NEXT optou-se por utilizar um TPC a alta pressão com xénon em estado gasoso, baseado em electroluminescência para a amplificação do sinal da ionização primária, a fim de procurar o decaimento duplo beta sem emissão de neutrino no isótopo ^{136}Xe.

O estudo de diferentes alternativas de fotossensores que podem ser usados no TPC para a detecção da electroluminescência do xénon é apresentado neste trabalho, em conjunto com estudos sobre o rendimento de electroluminescência do xénon na gama de pressões de 2 a 10 bar.

No contexto do NEXT, foram consideradas duas alternativas diferentes para a leitura da energia e da topologia dos sinais relativos às interações ocorridas dentro do detector: amplificação do sinal de ionização primária através da amplificação da electroluminescência produzida no xénon, utilizando fotossensores para ler a cintilação, ou através da amplificação da carga por avalanche electrónica e respectiva leitura, utilizando como eléctrodos a microestrutura Micromegas. Foi estudado o desempenho de uma destas estruturas a operar em xénon puro, para pressões entre 1 e 10 bar, com o intuito de avaliar a sua adequabilidade, para o TPC a usar pelo NEXT.

Os estudos desenvolvidos no âmbito desta tese ao nível dos fotossensores envolveram a determinação da eficiência quântica do APD S8664-SPL da empresa Hamamatsu e a resposta dos MPPCs S10362 e S10362-SPL da mesma empresa para a detecção de luz VUV incidente directamente no fotossensor ou convertida por um *wavelenght shifter* orgânico, TPB. O fotomultiplicador R8520-06SEL, da mesma empresa, já utilizado a

temperaturas criogéneas pela colaboração XENON, foi considerado como um potencial fotossensor a utilizar no NEXT, pelo que foi avaliado o seu desempenho na detecção da cintilação primária e secundária produzidas no interior de um GPSC, para pressões de xénon até 3 bar. Foi igualmente estudada a possibilidade de os PMTs serem calibrados *in-situ*, dentro do detector, utilizando a cintilação primária para promover a emissão de fotão único, no fotocátodo dos PMTs, e ajustando uma função exponencial na região das altas energias da distribuição obtida no PMT que permite obter o ganho do PMT.

CONTENTS

LIST OF FIGURES

1.

INTRODUCTION

NEXT, *Neutrino Experiment with a Xenon TPC,* is an international collaboration that aims to search for the neutrinoless double beta decay in ^{136}Xe at the Canfranc Underground Laboratory (LSC) in Spain [1]. NEXT has the collaboration of 14 different institutions and around 80 investigators to carry out the conception, development and construction of a 100 kg high-pressure xenon gas (HPGXe) Time Projection Chamber (TPC) to be able to perform the experiment.

A promising experimental method to reveal the neutrino nature is the search for neutrinoless double beta decays (0νββ). If neutrinos are Majorana particles then neutrinoless double beta decays can be observed. An observation of this type of decay would not only establish that neutrinos are, as a matter of fact, Majorana particles, neutral particles identical to their antiparticles, but would have further implications in physics and cosmology.

The first evidence of neutrinoless double beta decay was claimed in 2001 by the Heidelberg-Moscow experiment [2], a German-Russian collaboration that searchs for neutrinoless double beta decay on ^{76}Ge in the Gran Sasso Underground Laboratory (LNGS), Italy. From the data taken on the measuring period of August 1990 to May 2000, they obtained in 2001 a value between 0.8 and 18.3 x 10^{25} years for the half-life of the neutrinoless double beta decay, $T_{1/2}^{0\nu}$, with the best value of 1.5 x 10^{25} years, and an effective neutrino mass between 0.11 and 0.56 eV, with the best value of 0.39 eV [3]. This result was very controversial and the results obtained showed big uncertainties, implying that a new generation of experiments was required

to make significant improvements in sensitivity. No other double beta experiment was yet able to refute or confirm this observation.

There are experiments like the ICARUS [4], SNO [5] and the BOREXINO [6] that study the interactions of solar neutrinos in liquid Argon (LAr), heavy water (D_2O) and in a liquid organic scintillator, respectively, in order to better understand the properties of neutrinos.

Others experiments search for neutrinoless double beta decays in other isotopes. For example, Heidelberg-Moscow [7], IGEX [8], GEM [9], GENIUS [10], MAJORANA [11] and GERDA [12], are experiments searching for neutrinoless doube beta decay with germanium based detectors, enriched with the isotope ^{76}Ge. The CUORE [13] experiment, and its former smaller prototype CUORICINO [14] are based on tellurium dioxide (TeO_2) crystals, where they want to search for neutrinoless double beta decays on ^{130}Te. The COBRA [15] experiment will use CdZnTe semiconductor detectors to search for rare double beta decay processes. Others include tracking, such as the NEMO series [16], using a 3-D readout wire drift chamber. The EXO [17] experiment has measured for the first time the two-neutrino mode of double beta decay of ^{136}Xe [18] and will continue working in order to potentially discover the neutrinoless double beta decay using liquid Xenon (LXe).

The search for 0νββ processes is being carried out with different techniques. NEXT proposed a novel detection concept for neutrinoless double beta decay searches, based on a TPC filled with gaseous xenon at high pressure, to be installed in the Canfranc Underground Laboratory, Spain. This kind of xenon TPC provides excellent energy resolution, and together with powerful background rejection provided by the distinct double-beta decay topological signature, NEXT promises to be competitive in the next generation of neutrinoless double-beta decay experiments.

1.1. Neutrino

Neutrinos are one of the most interesting fundamental particles, they were proposed in 1930 by Wolfgang Pauli [19]. Pauli hypothetical particle was created to explain how beta decay could conserve energy and momentum, with the emission of a neutral particle, called neutrino. The neutrino was directly detected in 1956 by Reines and Cowan [20] and since then neutrinos have been the subject of numerous theoretical and experimental studies and have influenced many fields of research, including fundamental particle physics, cosmology, astrophysics and geology. In 1995 Frederick Reines was honored with the Nobel Prize for his work on neutrino physics.

Neutrinos are neutral particles with spin 1/2. They are not influenced by the electromagnetic force and due to their small masses are mostly unaffected by gravity. The only force through which neutrinos interact is the weak nuclear force, whose small interaction strength makes neutrinos extremely difficult to detect.

Neutrinos come in three distinct flavours. Each flavour corresponds to one of the charged leptons and they are referred to as electron (ν_e), muon (ν_μ) and tau (ν_τ) neutrinos. Another interesting property of neutrinos is the fact that the eigenstates of the weak interaction (ν_e , ν_μ and ν_τ) do not coincide with the mass eigenstates (ν_1 , ν_2 and ν_3). This difference between the basis states leads to the phenomenon of neutrino oscillations, that have been observed by numerous independent experiments, in which neutrinos are observed to change flavours as they propagate between weak interactions, that is, the probability of measuring a particular flavour for a neutrino varies periodically as it propagates.

The helicity of a particle represents the projection of the particle spin in the direction of motion. Chirality and helicity are very closely related ideas. Just as we say that a particle can have left- or right-handed helicity, we also say that a particle can have left- or right-handed chirality. So chirality is an intrinsic property of the particle and is the same as the helicity operator when the particle mass is zero or it can be neglected. For

massless particles the chirality and helicity are the same, that is, a massless left-chiral particle also has left-helicity.

The relative orientations of spin and linear momentum for neutrinos and antineutrinos are apparently fixed and intrinsic to the particles. For neutrinos the spin is always opposite the linear momentum and they are referred to as "left-handed", whereas the antineutrinos are always "right-handed" (see figure 1.1).

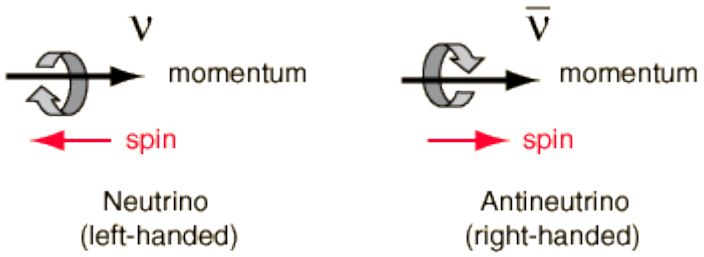

Figure 1.1. Relative orientations of spin and linear momentum for left-handed neutrinos and right-handed antineutrinos.

Neutrinos were defined in the Standard Model (SM) of particle physics as fermions, neutral and massless particles. Moreover, the Standard Model says that there are only left-handed neutrinos and right-handed antineutrinos. Lepton number L is conserved in the Standard Model because neutrinos are assumed to be massless and there is no chirally right-handed neutrino field. From the results of neutrino oscillation experiments [21-24], it was proven that neutrinos have a small, but non-zero, mass. The neutrino being a massive particle, it is necessary to extend the model to accommodate them.

The principles for extending the Standard Model are the conservation of electroweak isospin and renormalizability, which do not prevent each neutrino mass eigenstate ν_1 to be identical to its anti-particle $\bar{\nu}_1$, or a Majorana particle. However, the lepton number L is no longer conserved if $\nu_1 = \bar{\nu}_1$. The other Standard Model fermions, being electrically charged, are Dirac particles, distinguishable from their own antiparticles but neutrinos could be Majorana particles. Theoretical models, such as the “seesaw mechanism”, can explain the smallness of the neutrino mass and support this scenario.

The discovery of Majorana neutrinos would have profound theoretical implications in the formation of a new Standard Model while yielding insights into the origin of mass itself. If neutrinos are Majorana particles, they may fit into the leptogenesis scenario for creating the baryon asymmetry, and hence ordinary matter, of the Universe.

1.2. The double beta decays (2νββ and 0νββ) and the importance of 0νββ searches

The observation that neutrinos have mass has prompted an increased interest in investigating their intrinsic properties. Understanding the neutrino mass generation mechanism, the absolute neutrino mass scale and the neutrino mass spectrum are some of the main focuses of actual and future neutrino experiments. Another un-resolved question is the Majorana or Dirac nature of neutrinos, where the investigation of neutrinoless double beta decay can play a crucial part solving the neutrino nature issue.

Neutrinoless double beta decay is a hypothetical nuclear transition in which two neutrons undergo β-decay simultaneously, without the emission of neutrinos. In particular, the observation of the 0νββ decay is the most efficient method for solving the problem whether the neutrino is a Dirac or a Majorana particle because the process is only possible if the neutrino is a massive Majorana particle. Therefore, the search for this type of decay is considered as one of the most important issues to be solved due to his deep implications on particle physics and cosmology.

If the neutrino is the same as its own antiparticle, the neutrinoless double beta nuclear decay is allowed. In a double beta decay, two neutrons in the same nucleus convert into protons, each one emitting an electron and an antineutrino. If the neutrino is the same particle as the antineutrino, the two antineutrinos can annihilate and only two electrons are emitted.

The double beta decay (ββ) is a rare nuclear transition in which a nucleus with Z protons decays into a nucleus with Z+2 protons and the same mass number A. This kind of decay can only be observed in absence of a rival process, two successive single beta decays. The double beta decay can only happen if the mass of the intermediate nucleus is larger than that of the initial one, or if the single beta decay to the intermediate nucleus is highly suppressed. This happens in isotopes in which the initial nucleus is less bound than the final nucleus and both more bound than the intermediate one and the decay to the Z+1 isobar is forbidden or highly suppressed.

Single beta decay of many heavy even-even nuclei is energetically forbidden. However, a process in which a nucleus changes its atomic number by two while simultaneously emitting two beta particles is energetically possible for some even-even nuclei. Two double beta decay modes are possible. The standard two-neutrino double beta decay (2νββ),

$$ {}^{A}_{Z}X \rightarrow {}^{A}_{Z+2}Y + e_1^- + e_2^- + \bar{\nu}_{e1} + \bar{\nu}_{e2} \qquad (1.1) $$

proposed in 1935 by Goeppert-Mayer [25], has been observed in several isotopes, such as ^{76}Ge, ^{48}Ca, ^{100}Mo, ^{82}Se or ^{150}Nd [26]. In the 2νββ mode, total lepton number is conserved and this process is allowed by the Standard Model. The 2νββ rate is extremely low, half-lives for this decay mode have been measured at ~10^{19} years or longer in several nuclei.

The more interesting process, the neutrinoless double beta decay (0νββ),

$$ {}^{A}_{Z}X \rightarrow {}^{A}_{Z+2}Y + e_1^- + e_2^- \qquad (1.2) $$

was proposed in 1937 by Racah [27] and Majorana [28] and in 1939 by Furry [29]. Unlike 2νββ, 0νββ violates lepton number conservation and hence requires physics beyond the Standard Model. The 0νββ decay can be seen as an exchange of a virtual neutrino between two neutrons within the nucleus. By the Standard Model of weak interactions, the first neutron emits a right-handed antineutrino and the second neutron requires the absorption of a left-handed neutrino. This implies that the

neutrino must have mass and the neutrino and antineutrino have to be indistinguishable. This decay can be explained by mechanisms beyond the SM, all of them implying a Majorana mass term for the neutrino [30].

The two different decay modes, 2νββ and 0νββ, can be distinguishable by the shape of the spectrum of the electron sum energy (figure 1.2.). The 0νββ mode exhibits a mono-energetic line at the endpoint energy ($Q_{\beta\beta}$), that is, the signal of a neutrinoless double beta decay is a peak in the kinetic energy of the outcoming electrons. For the 2νββ mode, and because neutrinos are present, part of the available energy is also carried by them, so the spectrum is a continuous distribution with endpoint at $Q_{\beta\beta}$, in constrast with the neutrinoless case for which the electrons have all the available energy of the decay.

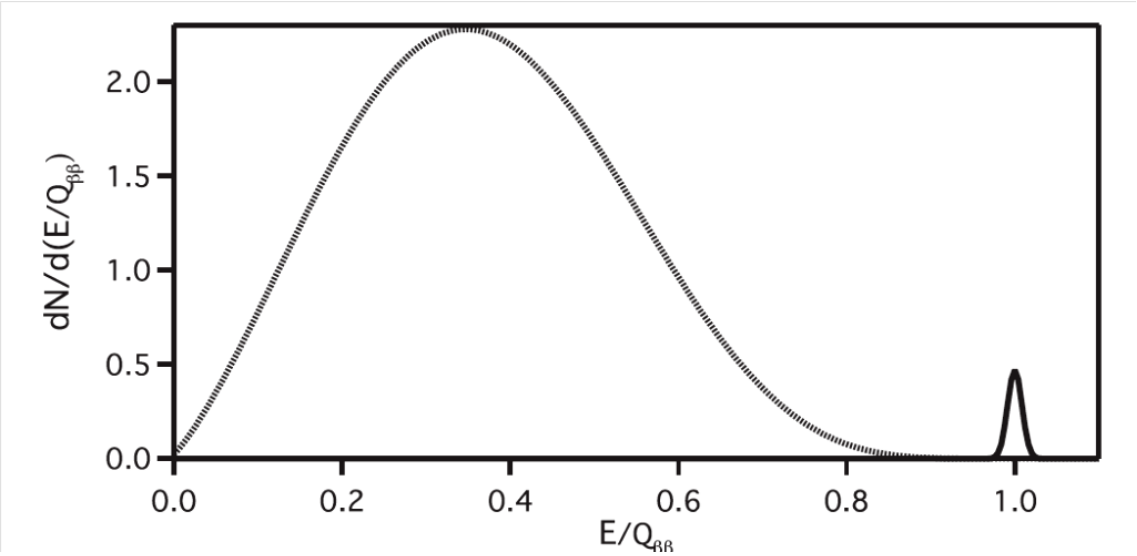

Figure 1.2. Typical distribution of kinetic energy of electrons in a standard double beta decay (2νββ) and in a neutrinoless double beta decay. A single peak (line in bold) at the $Q_{\beta\beta}$ endpoint is exhibited for 0νββ.

In double beta decay experiments, it is necessary to measure the sum of the energy of the radiation emitted by a ββ source (full spectra). As seen in figure 1.2 and for 0νββ searches, the sum of the kinetic energies of the two released electrons is always the

same, $Q_{\beta\beta}$, and given by the difference between the masses of the parent M(Z,A) and the daughter nuclei M(Z+2,A):

$$Q_{\beta\beta} = M(Z,A) - M(Z+2,A) \tag{1.3}$$

The distribution of 0νββ events is typically gaussian, with a non-zero energy range centered around $Q_{\beta\beta}$ due to the finite energy resolution of any detector. Moreover, other processes can occur in the detector (background) and fall in that energy region, compromising the sensitivity of the experiment [31]. Backgrounds from cosmic origin force these type of experiments to go underground to suppress this contribution and backgrounds from natural radioactivity of the detector materials components require a careful selection of radiopure materials.

1.3. NEXT choice for 0νββ searches

Since the Heidelberg-Moscow experiment results for neutrinoless double beta decay on ^{76}Ge, the new generation of double beta decay experiments try to make significant improvements to be sensitive to lifetimes longer than 10^{25} years and, therefore, sensitive to effective neutrino masses smaller than 0.1 eV.

Because to design, create and carry out a project that meets all the double beta decay experiment requirements is truly an experimental challenge, usually a figure of merit is used, the sensitivity to the effective neutrino mass ($m_{\beta\beta}$), in order to compare different proposed techniques [31]:

$$m_{\beta\beta} \propto \sqrt{1/\varepsilon}\left(\frac{b\,\Delta E}{M\,t}\right)^{1/4}, \tag{1.4}$$

where ε is the signal detection efficiency, b is the background rate in the region around $Q_{\beta\beta}$ (region of interest), ΔE is the energy resolution, M is the isotope mass and t is the data taking time.

The NEXT experiment aims to search for neutrinoless double beta decay in ^{136}Xe using a high-pressure xenon gas electroluminescence TPC, combining a good energy resolution and a low background rate using event discrimination through pattern recognition, resulting in excellent sensitivity to $m_{\beta\beta}$. For a total exposure of 500 kg.year, the expected sensitivity is better than 0.1 eV, of the order of other experiments in the same field [31].

Xenon gas was the detector medium choice of the NEXT experiment because this noble gas acts simultaneously as target and detector. Among the noble gases, xenon is the only one that has two natural ββ decaying isotopes, ^{134}Xe and ^{136}Xe, with $Q_{\beta\beta}$ values of 825 keV [1] and 2458 keV [32], respectively. ^{136}Xe, whose natural abundance is rather high (9 %), is a better choice since its $Q_{\beta\beta}$ value is higher and the radioactive backgrounds are less abundant at higher energies with the exception of the 2615 keV γ-ray from ^{208}Tl. Also, it can be enriched by centrifugation to high concentrations in a relatively easy and not so expensive way, compared to other isotopes, because xenon is a gas at standard temperature and pressure and hence easy to process in ultracentrifuges.

Other advantage of xenon is the non-existence of other long-lived radioactive isotopes that could became part of the background. Xenon can be continuously purified during the lifetime of the experiment and gaseous xenon can provide high energy resolution, better than 0.5% at 2500 keV [33].

The 2νββ lifetime of ^{136}Xe was already measured. A value of 2.11 x 10^{21} years was obtained by the EXO-200 experiment [34] and the KamLAND-Zen Collaboration measured a value of 2.38 x 10^{21} years [35], in agreement with the result of the EXO collaboration. In comparision, the 0νββ lifetime of ^{136}Xe is predicted to be in the same order of magnitude as other commonly used 0νββ isotopes, like ^{76}Ge [31, 36].

One of the most attractive features of using a TPC is the fact that it can be scaled up to large masses. Using the same material as double beta decay source and detection medium, the background and the energy loss of the decay electrons are minimized. Some of the most recent experiments are using large TPCs, not only for neutrinoless double beta decays but also for dark matter search. Dual-phase xenon TPCS are used by XENON [37] and LUX [38] experiments. In the search for neutrinoless double beta decays, EXO is using a liquid Xe TPC.

The Gotthard Experiment [39] was the only double beta decay experiment before NEXT which considered using gaseous Xe TPC. The Gotthard Experiment consisted in a small xenon gas TPC (5.3 kg of ^{136}Xe enriched to 68%) operated at 5 bar, with no observable results due to poor energy resolution and large backgrounds [40].

Because the density of liquid xenon (about 3 g/cm^3) [41] is higher compared to the density of 1 bar gaseous xenon (about 0.005 g/cm^3) [41], LXe TPCs are more compact detectors over high pressure Xe TPCs. On the other hand, because gaseous detectors are larger than LXe detectors, they present a smaller surface to volume ratio which is favorable to reduce the background, like the γ-rays emanated by the detector vessel.

An advantage of using a HPGXe TPC is that a neutrinoless double beta decay event leaves in the gaseous xenon a distinctive topological signature of an ionization track (figure 1.3), a twisted track due to multiple scattering of the photoelectron, with larger energy depositions at both ends [1] when compared to the point charge deposition in LXe detectors.

Because of the high density of Xe in the liquid state, the electrons in a LXe TPC will deposit all their energy in a blob, making hard for the LXe TPCs to distinguish between a 0νββ event and a gamma interaction that could deposit energy in the vicinity of $Q_{\beta\beta}$ by photoelectric or Compton effects. On the other hand, the characteristic signature from a 0νββ event, with two electrons whose energies add up to $Q_{\beta\beta}$ (2458 keV for ^{136}Xe), can be revealed in gaseous Xe. Since the average energy of the two electrons is about 1250 keV and at 10 bar each electron travels about 15 cm [1]. Electrons in this energy range can be easily tracked in the gas, having trajectories completely

dominated by multiple scattering and resulting in a twisted ionization track (figure 1.3) with a larger charge density at its end.

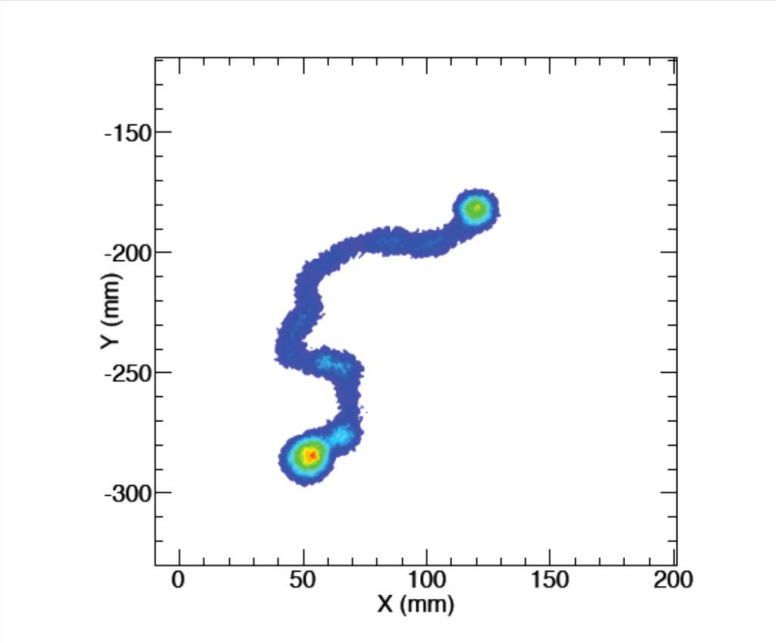

Figure 1.3. Monte Carlo simulation of the topological signature of a ^{136}Xe neutrinoless double beta event in a 10 bar HPGXe TPC. This track is tortuous and ends in two large depositions of energy (blobs), and is about 30 cm long for 10 bar of Xe [1].

Therefore, the NEXT choice for a HPGXe over a LXe TPC reflects the fact that a gas xenon TPC offers not just better energy resolution but also a distinct kinematical signature for 0νββ events and simultaneously a better capability for rejecting backgrounds. To achieve a better energy resolution, the primary ionization signal is amplified in the HPXe detector using the electroluminescence of xenon instead of charge avalanche amplification.

1.4. Electroluminescence

Conde and Policarpo [42] in 1967 and Charpak [43] in 1975 started to develop detectors for high-resolution spectrometry of low-energy X-rays, exploiting electroluminescence (EL) in noble gases.

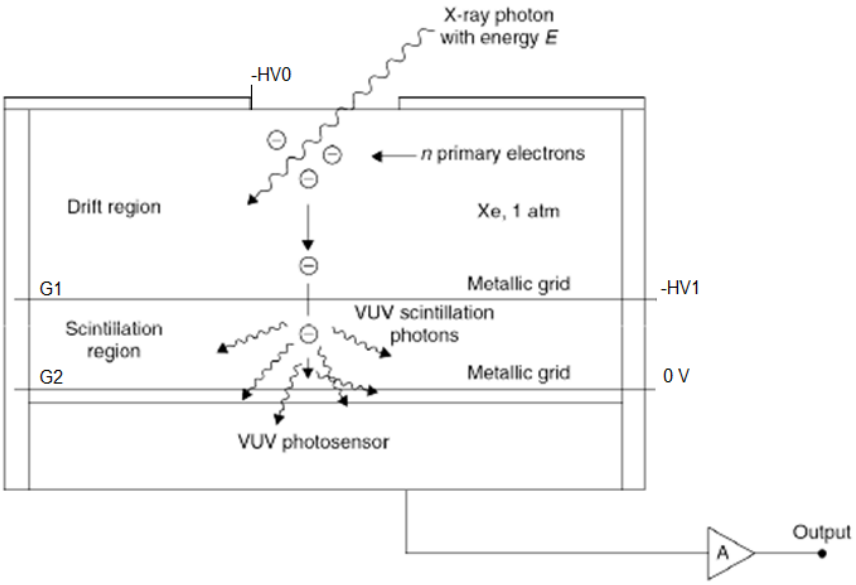

Figure 1.4. The GPSC operation principle.

In a standard GPSC (figure 1.4), when the incident radiation is absorbed in the drift region, the ionisation of the noble gas produces primary electrons. In addition, upon the interaction of the ionising radiation with the noble gas, scintillation is also produced, the so-called primary scintillation.

If we make the primary electrons drift to a region with a suitable electric field, with intensity between the gas scintillation and ionization thresholds for electron impact, the scintillation region, electrons gain enough energy from the electric field to excite but not ionize the gas atoms by electron impact. Gas scintillation results from the

subsequent excited atoms going through excimer formation and de-excitation processes. This is the so-called secondary scintillation or electroluminescence.

For Xe pressures above a few tenths of bar the electroluminescence spectrum of xenon consists of a narrow line peaking at 172 nm, with 5 nm FWHM [44], the second continuum. For a constant electric field applied in the scintillation region, the number of secondary scintillation photons produced by a single primary electron is nearly constant and can reach values as large as 1000, depending on the electric field applied [45, and references therein]. These VUV photons are detected by a suitable VUV photosensor, usually a photomultiplier tube. The VUV photosensor signal amplitude is proportional to the number of detected VUV photons, thus to the number of primary electrons crossing the scintillation region and, therefore, to the energy deposited by the incident X-ray, hence the name of gas proportional scintillation counter (GPSC) for this device.

The secondary scintillation photons are two or three orders of magnitude higher than the primary scintillation photons. On the other hand, the secondary scintillation rise time is much slower (a few μs) than for primary scintillation (a few ns) [46].

For half a century it has been known that secondary scintillation provides signals with much larger amplitudes, minimal fluctuations in gain and negligible electronic noise. The secondary scintillation process available in noble gases permits large amplification with negligible statistical fluctuations, offering the prospect of detector energy resolution approaching the Fano factor limit, making it the best amplification technique for dark matter and neutrinoless double beta decay experiments [47].

Therefore, especially in experiments with very low event rates and/or high background levels, as the 0νββ experiments, it is of great importance to use the secondary scintillation signal rather than the signal from either unamplified primary ionization or secondary ionization [47]. This is the technique to be used in NEXT, with a nominal xenon pressure of 10 bar [1, 48].

1.5. The NEXT TPC

There are some requirements that must be accomplished for the NEXT TPC in order to be able to search for 0νββ decay in ^{136}Xe. The TPC must be able to detect efficiently the weak primary scintillation light that occurs in the drift region in order to define the start-of the-event, t_0, and determine the spatial localization of the event along the drift direction. Moreover, it needs to track ββ decay electrons in order to determine the event topology (0νββ or 2νββ), suppressing backgrounds, determine the spatial localization of the event in the plane perpendicular to the drift direction and be able to determine the total energy of the event with an energy resolution of 1% or better at $Q_{\beta\beta}$ (2458 keV) [1].

Two different configurations of TPC were considered: a symmetric TPC with a centralized, transparent cathode and two anode planes at both end-caps equipped with photosensors (figure 1.5) and an asymmetric TPC, where the cathode is near to one end cap and the anode is placed at the opposite one (figure 1.6).

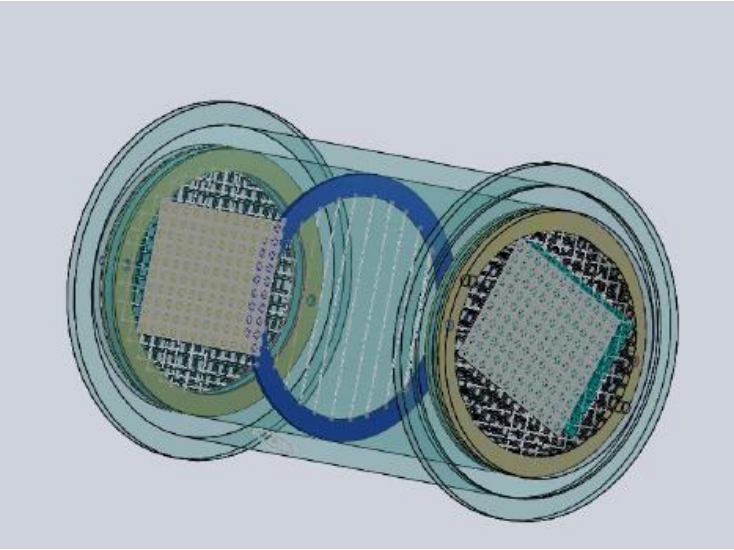

Figure 1.5. A symmetric, conventional TPC, with a central, transparent cathode and two anode planes at both end-caps equipped with photosensors [48].

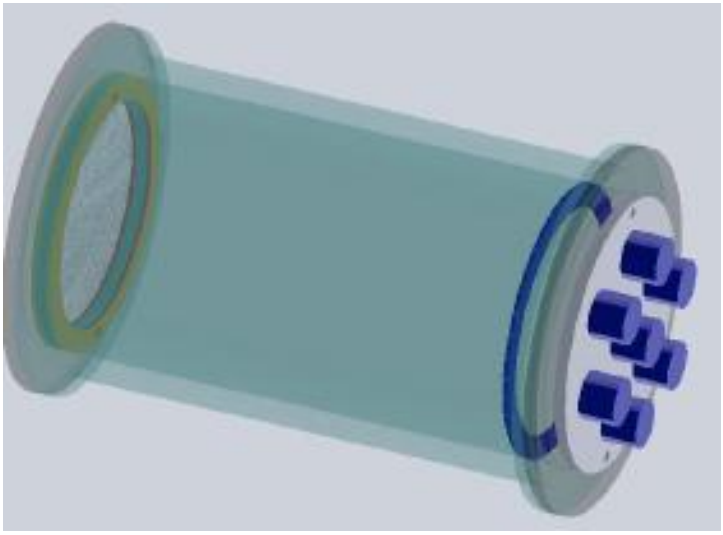

Figure 1.6. An asymmetric TPC in which the cathode plane performs the energy function and the anode plane performs the tracking function [48].

For the optimization of the TPC design, it is necessary to study the optimal chamber layout, different readout configurations and technologies in order to meet the necessary requirements.

Xenon is a suitable detection medium that provides both scintillation and ionization signals. To achieve optimal energy resolution, the ionization signal is amplified in the TPC using the electroluminescence of xenon. The detector chamber will have separated detection systems for tracking and calorimetry, the so-called SOFT (*Separate, Optimized Functions for Tracking*) concept [1], shown in figure 1.7.

In figure 1.7, when a particle interacts in the HPGXe, it transfers its energy to the gas through ionization and excitation. The excitation energy results in the prompt emission of VUV (~172 nm) photons, called primary scintillation. On the other hand, the ionization tracks (positive ions and free electrons) created by the particle interaction are prevented from recombination by an electric drift field (0.3–0.5 $kVcm^{-1}$). When the ionization electrons drift towards the TPC anode, they enter a small region, defined by two highly-transparent meshes, where it is applied a higher electric field (about 3 $kV\ cm^{-1}\ bar^{-1}$) in order to produce secondary scintillation light, and so more VUV photons are isotropically generated by electroluminescence.

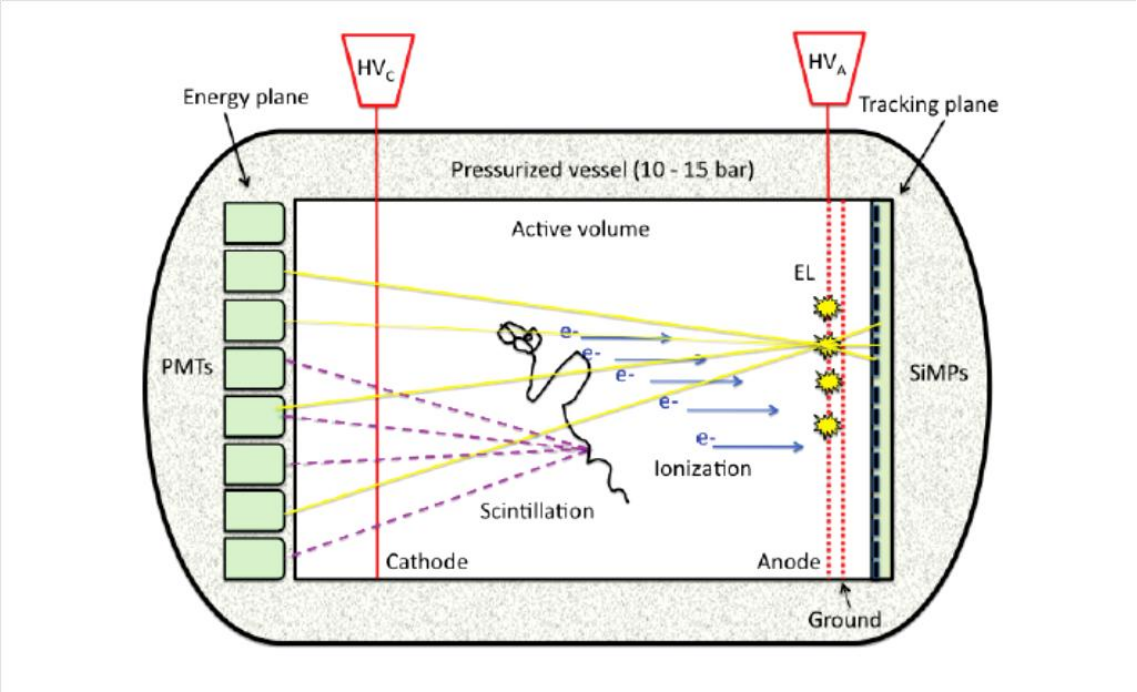

Figure 1.7. The SOFT concept in the NEXT TPC [1].

In the SOFT concept, both scintillation and ionization produce optical signals that are detected by photomultiplier tubes (PMTs) located on the energy plane, behind the cathode. The start-of-event t_0, is given by the detection of the primary scintillation light. The electroluminescence light provides energy measurement and tracking since EL light produced near the anode plane is also detected in the tracking plane by an array of Silicon Photomultipliers (SiPMs) (figure 1.7).

The asymmetric TPC is not the only possibility to implement a SOFT concept. Figure 1.8 shows a SOFT concept for a symmetric TPC. The energy readout plane is provided by a large circumferential array of wavelength-shifting scintillator bars to detect both primary scintillation and EL. The most important disadvantage is the poor scintillation photon detection efficiency since a substantial fraction of the wavelength-shifting light is not captured.

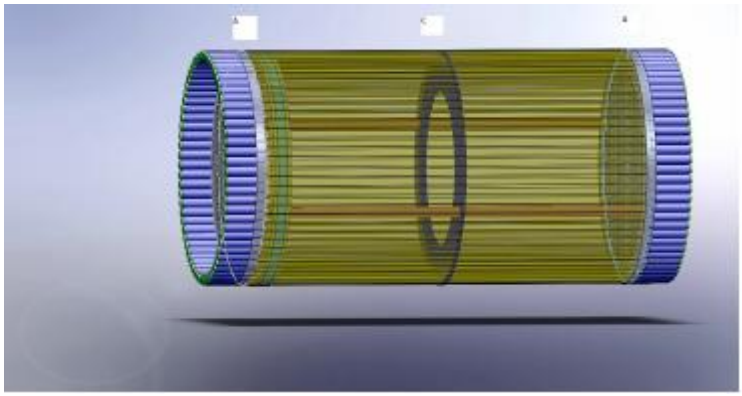

Figure 1.8. A symmetric TPC with wavelength-shifting scintillator bars for the energy function [48].

In SOFT concept, the energy function will be provided by the detection of the EL light by an array of photosensors. In order to meet the energy resolution requirement and other signal characteristics, together with the need for calibration of photosensor devices, the PMTs are ideal for the energy measurement. Also, the detection of the primary scintillation light, and then t_0, is obtained by the same energy readout plane. This primary scintillation light signal is very small compared to the El light, but is well separated in time from the signal of the secondary scintillation light. PMTs are ideal for this purpose as well since they can detect faint light levels.

For the tracking function, it is necessary that the array of photosensors is able to detect the EL light produced in the region near the anode plane. The tracking plane needs a photosensor with better pixelization than the one of the energy plane. Also, the energy resolution of the tracking photosensors does not need to be as good as the one of the energy plane since the purpose of the tracking plane is to be able to distinguish the topological signature of the event.

For the tracking plane, there were some proposals to be explored, like the use of silicon photosensor devices (like Avalanche Photodiodes and Silicon Photomultipliers) for the EL light detection, and also the possibility to perform the tracking function using micro-pattern devices, like Micromegas.

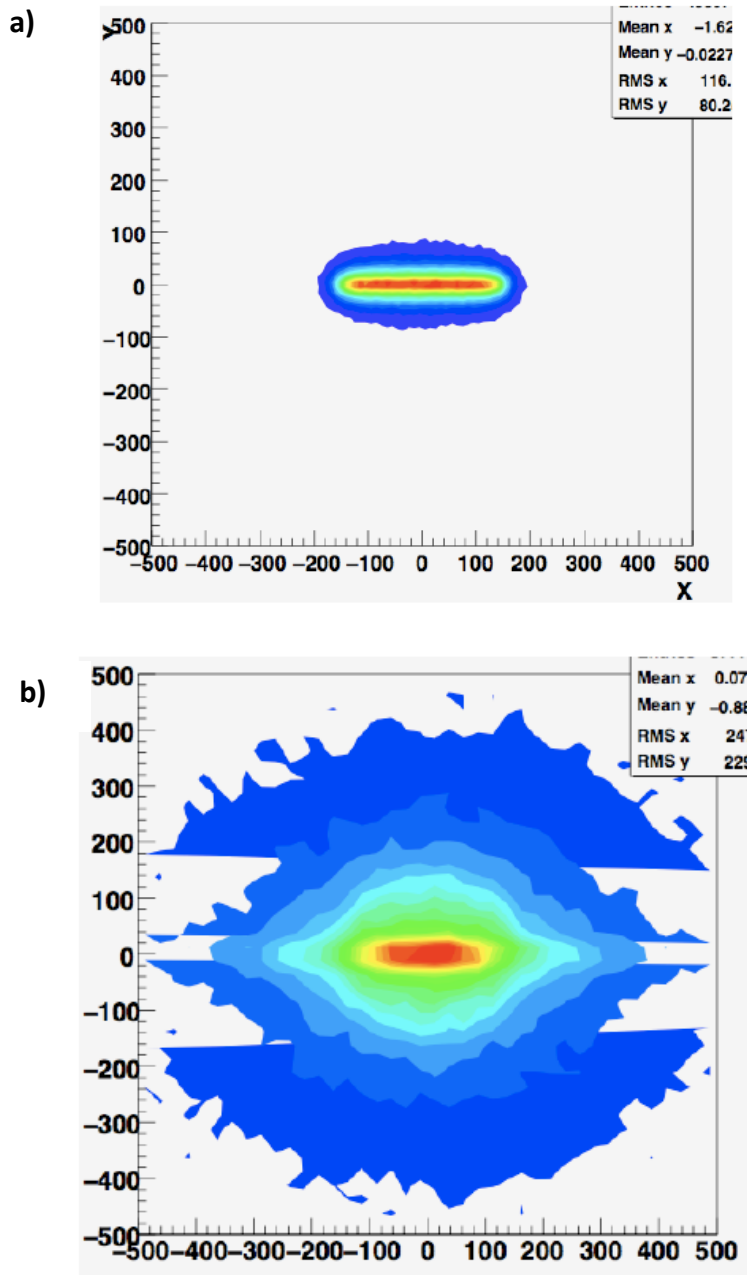

Figure 1.9. Simulation of the EL light detected by the different readout planes, considering a 30 cm long horizontal track generated near the EL region. (a) EL light detected in the tracking readout plane, immediately behind the EL region. (b) EL light detected in the energy readout plane, in the opposite direction. Spatial dimensions are given in mm [48].

When the ionization electrons arrive to the anode and cross the region between the two parallel meshes (figure 1.7), electroluminescence light can be produced if a moderate high electric field is applied in that region.

The EL light is not distributed in the same way in the tracking readout plane immediately behind the EL region and in the energy readout plane opposite to the EL region. Figures 1.9(a) and 1.9(b) show the simulation of the EL light detected by the different readout planes, considering a horizontal track generated near the EL region. In the tracking plane (figure 1.9(a)), the light is distributed following the track path, while the light recorded by the opposite plane (figure 1.9 (b)) is much more spread.

1.6. Photosensors for the NEXT experiment

For the NEXT experiment, the baseline design of the HPGXe TPC contemplates two different arrays of photosensors, each of them with a specific contribution and specific requirements that need to be satisfied in order to meet the TPC performance needed for the neutrinoless double beta decay search in ^{136}Xe. For this purpose, it is important to study the available technologies of photosensors.

1.6.1. Photomultipliers tubes

A photomultiplier tube (PMT) is a vacuum tube consisting of an input window, a photocathode, focusing electrodes, several dynodes and an anode, as illustrated in figure 1.10.

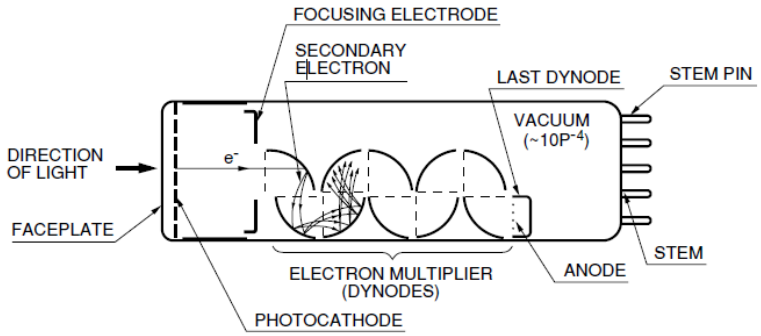

Figure 1.10. Schematic of a photomultiplier tube [49].

To be detected in a PMT, a photon needs to pass through the input window and hit the photocathode so that photoelectrons are emitted from the photocathode surface by photoelectric effect. The photoelectrons are then accelerated and focused by the focusing electrodes to the first dynode, where they are multiplied by secondary electron emission. This multiplication is repeated at each of the successive dynodes. When the final electrons are emitted from the last dynode, they are collected by the anode, producing the output signal.

Photomultipliers are widely used in several types of experiments. For the NEXT purpose, photomultipliers will be used to detect the primary scintillation light and also to measure the total energy deposition in the detector, through the detection of the secondary scintillation. A good candidate for NEXT PMTs is the Hamamatsu Photonics R8520 prototype (figure 1.11), with 2.5 cm size, square-shaped photocathode. Because of the relative small size and square shape of the photocathode, these PMTs permit an optimal packing for the readout planes. In addition, they have good sensitivity to the VUV light (20% - 30% quantum efficiency at 170 nm, depending on the series), low background (around 0.5 mBq per PMT plus base on average) and have been largely tested at cryogenic temperatures (LXe temperatures around -90ºC). On the other hand, the R8520 PMTs can withstand pressures only up to 5 bar [49].

Figure 1.11. The R8520 Hamamatsu PMT [49].

Another important feature when using a PMT in the NEXT experiment is to provide operation at a sufficiently high gain such that single photoelectron detection is efficient. This feature is necessary for both primary scintillation and EL light detection.

Because an array of PMTs is needed for the readout plane and each of them has different quantum efficiency and gain, for a successful PMT calibration between the array it is sufficient to know the relative quantum efficiencies and to determine the relative gains by using a single photoelectron pulse height distribution of each PMT at the same bias voltage applied.

1.6.2. Silicon photosensors

Silicon photosensors can be used as tracking devices in the tracking readout plane of the HPGXe NEXT TPC. As example of silicon photosensors, alternatives like avalanche photodiodes (APDs) and silicon photomultipliers (SiPMs) have been studied as tracking devices for NEXT.

Avalanche photodiodes (figure 1.12) are compact and low power consumption devices made of silicon p-n junctions, where the electric field can reach values high enough to allow ionization by electron impact, with subsequent avalanche multiplication. They are able to detect light from the infrared region to the VUV region, and X-rays with

energy up to about 25 keV, depending on the internal structure. Typical gains for an APD are in the range of ten to a few hundred [50].

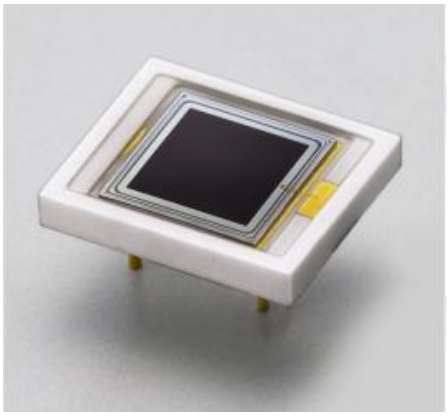

Figure 1.12. Hamamatsu silicon avalanche photodiode [49].

In silicon devices, there is conversion of light into an electrical signal. When a photon hits the active area of the silicon device and is absorbed by photoelectric effect, electron-hole pairs are produced if the photon energy is higher than the band-gap energy of silicon. When electron-hole pairs are produced in the depletion layer of a photodiode with reverse voltage applied to the PN junction, the electrons drift towards the N^+ side, while the holes drift towards the opposite direction, the P^+ side, due to the electric field across the PN junction. The drift speed and energy of these charge carriers depend on the electric field applied. In the depletion region, the electric field intensity is low, increasing towards the PN junction, achieving its maximum around this junction. The electrons are then accelerated towards the PN junction where they undergo an avalanche multiplication due to the intense electric field in this region (figure 1.13).

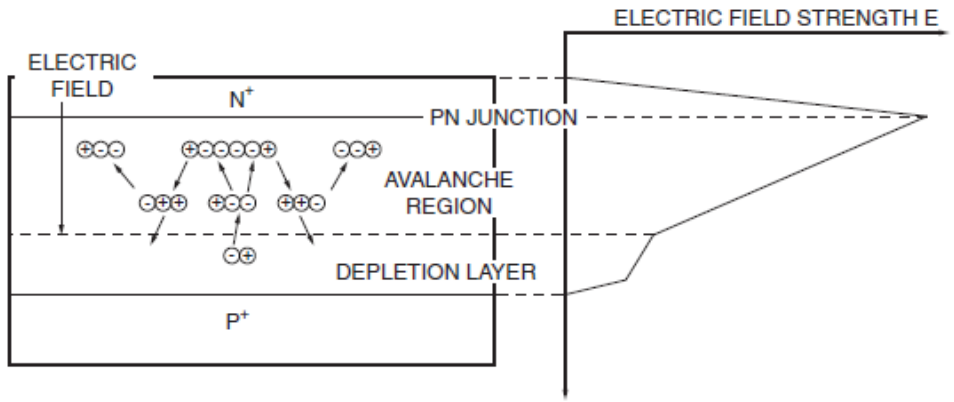

Figure 1.13. Schematic of the avalanche process that occurs in an APD, showing the typical profile of the electric field [49].

Although their performance in the response to direct X-rays can be similar or even better than that of proportional counters, low-energy X-ray detection techniques with APDs were mainly developed to measure the number of charge carriers released by X-rays.

Figure 1.14 shows several SiPMs, also called Multi Pixel Photon Counters (MPPCs). They are photon-counting devices consisting of multiple APD pixels, connected in parallel, that can operate in two different modes: normal and Geiger. The normal mode is when the reverse voltage applied is set below the breakdown voltage; in this case the MPPC maximum gain is of the order of several hundred. The Geiger mode operation is achieved when the reverse voltage is higher than the breakdown voltage, increasing the gain of an APD to a significantly higher level (more than 10^5).

Above some breakdown voltage, the APD remains stable only until an electron enters the avalanche region, resulting in the avalanche region breaking down and the APD becoming a conductor, this is known as a Geiger discharge. Because the current flow produced by the breakdown is large the output signal is even larger. If a resistor is placed in series with the detector, when the junction breaks down, large current flows through the resistor, resulting in a voltage drop across the resistor and the APD. If the

voltage drop is enough, the APD voltage will drop below the breakdown voltage and will be reset.

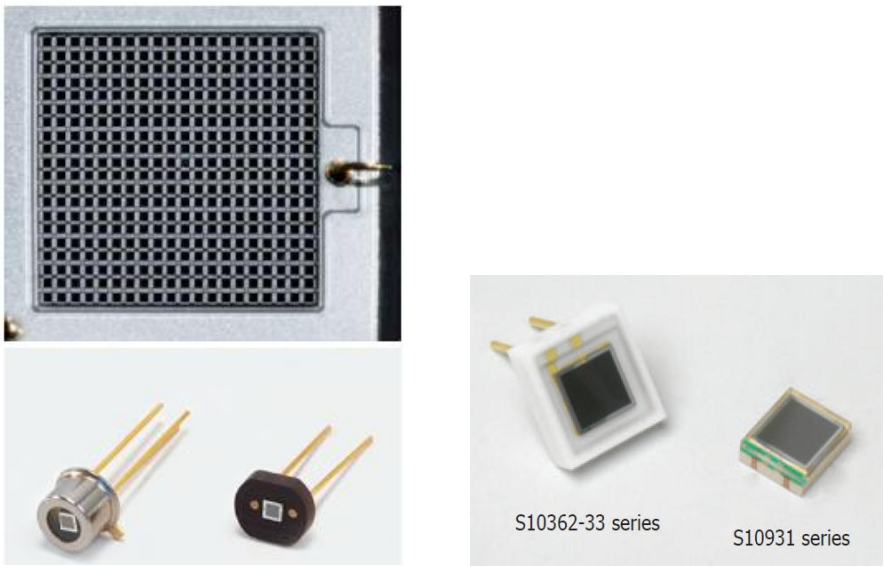

Figure 1.14. Top: Detail of a multi-pixel photon counter (MPPC), showing the multiple APD pixels. Bottom: examples of Hamamatsu MPPCs with 1 mm^2 and 9 mm^2 active areas [49].

Recently developed MPPC arrays can distinguish multi-photon from single-photon light levels, being suitable to single photoelectron detection.

Photon detection efficiency (PDE) is a parameter that determines which percentage of the incident photons is detected. Not all carriers produced by the incident photons will create pulses large enough to be detected. The PDE is the product of the APD quantum efficiency, the fill factor (ratio between the effective and the total pixel size) and the Geiger avalanche probability (ratio between the number of excited pixels and the number of photon-incident pixels).

MPPCs offer advantages over other photosensors. They are compact, rugged, easy to use, operated at room temperature with low bias (the operating voltage at Geiger mode is below 100 V), and have low cost. This new type of device is also suitable for detecting light at the photon-counting level with excellent detection efficiency

(figure 1.15). Other important advantages of these devices are high gain (10^5-10^6), low multiplication noise, insensitivity to magnetic fields and excellent time resolution.

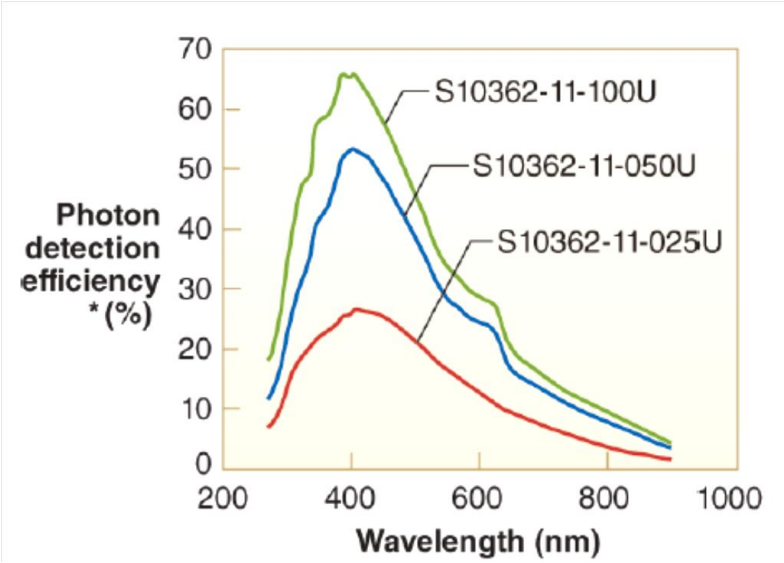

Figure 1.15. Photon detection efficiency as a function of the wavelength for three Hamamatsu multi-pixel photon counters with different numbers of pixels [49].

One disadvantage is the MPPC sensitivity to temperature changes. The MPPC gain is temperature dependent. As the temperature rises, at a constant voltage applied to the MPPC, the lattice vibrations in the crystal become stronger, decreasing the probability that the accelerated carrier could strike the crystal with enough energy in order to continue ionizing, dropping the gain at that reverse voltage. Therefore, to keep a stable operation output, if temperature stabilization is not possible, it is necessary to change the reverse voltage applied, in order to keep the gain constant. The reverse bias voltage needed to apply to MPPCs to maintain a constant value of gain, increases with temperature.

1.6.3. Micromegas

The use of Micromegas (MM), a micropatterned electron multiplier, for the tracking plane as well as for the energy plane, was also evaluated for the NEXT experiment.

Micromegas (MICRO-MEsh-Gaseous Structure) was conceived and developed by I. Giomataris at CEA-Saclay [50]. It consists of two parallel plates, a metallic micromesh suspended over an anode plane, with insulator spacers (pillars) defining a precise and high electric field gap of 50-150 µm [50, 51] (figure 1.16).

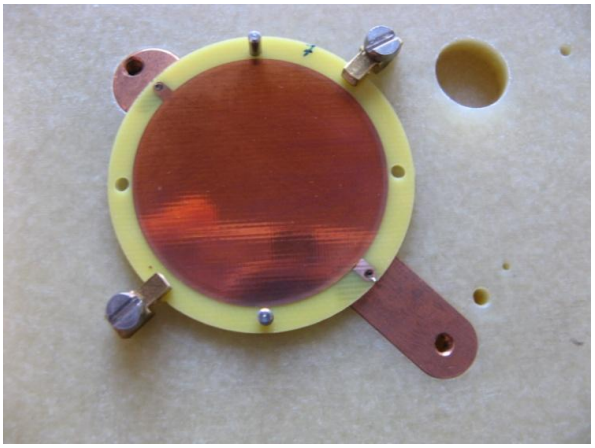

Figure 1.16. Micromega with 3.5 cm diameter.

Micromegas are used in many experiments, with good performance in spatial, temporal and energy resolution, and many other advantages like robustness, homogeneity and operation stability.

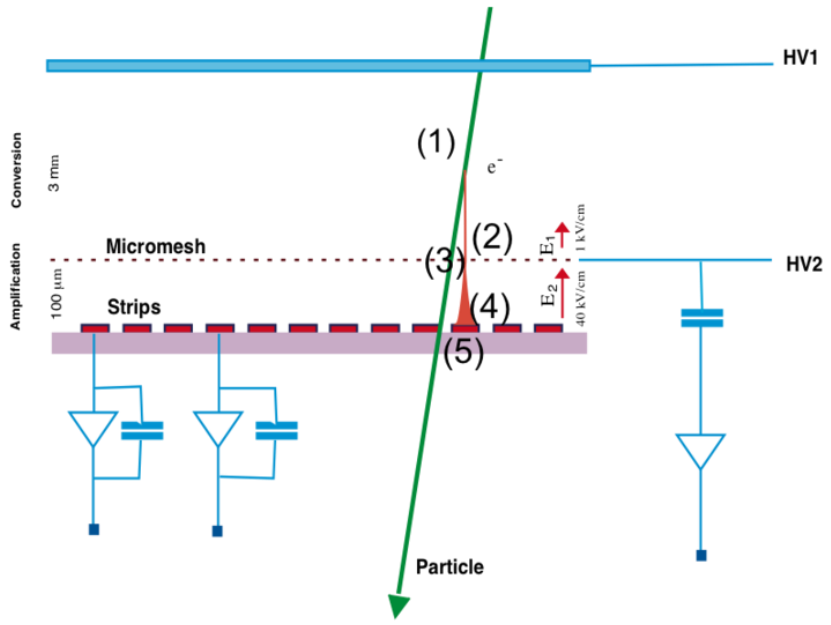

Figure 1.17. Micromegas operation principle.

Figure 1.17 illustrates the operation principle of Micromega. While passing through the detector, a particle can ionise the gas atoms, producing an electron/ion pair (1) in the conversion gap. The free electron will drift (2), within the influence of a small electric field (typically 10^2-10^3 V cm^{-1}) towards the amplification gap. When the electron arrives to the micromesh (3), enters an intense electric field region (typically 10^4-10^5 V cm^{-1}) and is accelerated by this field, the electron gains enough energy to produce another electron/ion pairs that will also ionise the gas, creating an avalanche (4). The readout electrode (5) is usually segmented in strips or pixels in order to obtain the position of the particle impinging in the detector.

The accumulation of positive ions in the amplification gap can modify locally the electric field and hence, decrease the gain achieved by the microstructure. But, because of the high intensity electric field on the amplification gap, the ion cloud can be efficiently collected in the micromesh.

Figure 1.18 shows the typical electric field lines in a Micromegas structure and the trajectories of the primary electrons and ions created in the avalanche process. Due to

the fast evacuation of positive ions and the electric-field configuration, Micromegas can work under high irradiation exposures [52].

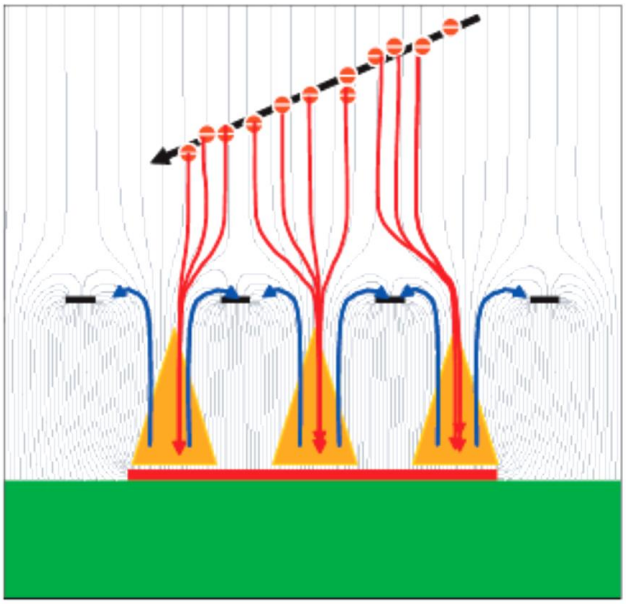

Figure 1.18. Scheme of the typical electric field lines in a Micromegas and the drift trajectories of the primary electrons entering the amplification gap (red lines) and ions created in the avalanche drifting towards the mesh(blue lines) [48].

The homogeneity of the gain over large surfaces of Micromegas readout plane makes it one of the micro-pattern concepts with better prospects for scaling up. In terms of tracking position, resolution, pixelization and capability for covering large surfaces with reduced costs, Micromegas is a competitive possibility to use in the NEXT TPC. They can be used in the tracking plane, keeping the energy plane of the TPC with an array of photosensors.

1.7. Motivation

This thesis presents a contribution to the R&D effort performed under the NEXT collaboration to decide on the technology to be used in the TPC, e.g. either using EL readout with photosensors for the topology and energy planes or using charge avalanche amplification with Micromegas for topological and energy readout planes, and to decide the photosensor to be used in the topological readout plane. In addition, a contribution for the study of the EL yield that could be achieved in pure Xe for gas pressures up to 10 bar and the study of the performance of the Hamamatsu R8520 PMT at room temperature, for the detection of primary and secondary scintillation, was also performed in order to supply the collaboration with important information. The EL yield is an important parameter to be known, e.g. for correct detector simulation.

Chapter 2 presents the studies performed for the determination of the electroluminescence yield, at room temperature, as a function of electric field, in the gas scintillation region for pressures ranging from 2 to 10 bar of xenon, using a Large Area Avalanche Photodiode to collect the VUV secondary scintillation produced in the detector by 22.1 keV and 59.6 keV X-rays.

The operation and the quantum efficiency of a Hamamatsu S8664-SPL Avalanche Photodiode for xenon scintillation detection, is presented in chapter 3. The work presented was performed in Coimbra, with the exception of the non-linear response to X-rays and the solid angle simulation, which were obtained by our colleagues at IFAE, Barcelona, within the NEXT Collaboration.

Chapter 4 evaluates the performance of the Hamamatsu R8520-06SEL Photomultiplier, at room temperature, for the detection of primary and secondary scintillation produced inside a GPSC, as a result of the interaction of 5.9 keV X-rays in gaseous xenon, at pressures up to 3 bar. This PMT was a candidate for the primary and EL

readout in the energy plane and the evaluation of its performance at room temperature was necessary as part of the overall evaluation of this PMT.

In Chapter 5 the performance of a Micromegas is presented, in the pressure range of 1 to 10 bar of xenon. Studies include the charge amplification of the primary ionization charge, e.g. considering the MM for the energy readout plane or for its use as a VUV photosensor when combined with a CsI phtocathode, and the VUV secondary scintillation light produced in the charge avalanches of the MM. The assembly of the detector and the Xe purification system, the initial studies at 1 bar of xenon and the study of the dependence of the relative amplitude of the Micromegas charge avalanche and EL output as a function of reduced electric field in the drift region, for 6 and 10 bar, have been performed under this thesis, while the study of the charge avalanche gain and EL output for other pressures have been performed under the master thesis of Catalin Balan.

The evaluation of the performance of Hamamatsu S10362 and S10362-SPL Silicon Photomultipliers is described in chapter 6. The response of these photosensors in the detection of xenon electroluminescence light either by using direct VUV photon incidence or by using an organic wavelength shifter, was investigated. The coatings were all performed at Instituto de Ciencia Molecular (ICMOL), Valencia. Due to TPB degradation to light and air, the studies were performed at IFIC by colleagues of the NEXT collaboration.

Chapter 7 presents the possibility of calibrating PMTs as scintillation detectors, *in-situ,* using primary scintillation produced by X-rays to induce a single photoelectron response. The data “SER - Standard Method” were obtained by our colleagues at IFIC, Valencia, while the data obtained with the primary scintillation and the studies relative to the exponential fit were performed under this PhD work.

The work developed under this thesis was carried out in the Atomic and Nuclear Instrumentation Group (GIAN) of the University of Coimbra, and resulted in the publications listed below:

Secondary scintillation yield in high-pressure xenon gas for neutrinoless double beta decay (0νββ) search
E.D.C. Freitas, C.M.B. Monteiro, M. Ball, J.J. Gómez-Cadenas, J.A.M. Lopes, T. Lux, F. Sánchez and J.M.F. dos Santos
Physics Letters B 684 (2010) 205–210.

Primary and secondary scintillation measurements in a Xenon Gas Proportional Scintillation Counter
L.M.P. Fernandes**,** E.D.C. Freitas, M. Ball, J.J. Gomez-Cadenas, C.M.B. Monteiro, N. Yahlali, D. Nygren and J.M.F. dos Santos
Journal of Instrumentation, JINST 5 P09006 (2010).
Journal of Instrumentation, JINST 5 A12001 (2010).

Micromegas operation in high pressure xenon: charge and scintillation readout
C. Balan, E.D.C. Freitas, T. Papaevangelou, I. Giomataris, H. Natal da Luz, C.M.B. Monteiro and J.M.F. dos Santos
Journal of Instrumentation, JINST 6 P02006 (2011).

Characterization of the Hamamatsu S8664 Avalanche Photodiode for X-Ray and VUV-light detection
T. Lux, E.D.C. Freitas, F.D. Amaro, O. Ballester, G.V. Jover-Manas, C. Martín, C.M.B. Monteiro, F. Sánchez and J.Rico;
Nucl. Instr. Meth. A 685 (2012) 11-15.

In Situ calibration of a PMT inside a scintillation detector by means of primary scintillation detection
NEXT Collaboration
submitted to JINST

References

[1] NEXT Collaboration*, NEXT-100 Technical Design Report (TDR)*, 2012 JINST 7 T06001; http://next.ific.uv.es/next/

[2] H. Klapdor-Kleingrothaus *et al.*, *Latest results from the Heidelberg-Moscow double beta decay experiment*, Eur. Phys. J. A12 (2001) 147-154.

[3] H.V. Klapdor-Kleingrothaus *et al.*, *Evidence for neutrinoless double beta decay*, Modern Physics Letters A, Vol. 16, No. 37 (2001) 2409-2420.

[4] ICARUS Collaboration, *ICARUS Liquid Argon Imaging Chamber: a novel detector technology*, 13th International Conference on Neutrino Physics and Astrophysics, Boston, MA, USA, 5 - 11 Jun (1988) 280-288.

[5] SNO Collaboration, *The Sudbury Neutrino Observatory*, Nucl. Instrum. Meth. A449 (2000) 172-207.

[6] Borexino Collaboration, *Science and Technology of Borexino: A Real Time Detector for Low Energy Solar Neutrinos,* Astroparticle Physics 16 (2002) 205-234.

[7] H.V. Klapdor-Kleingrothaus *et al.*, *Latest results from the Heidelberg-Moscow double beta decay experiment*, Eur. Phys. J. A 12 (2001) 147-154.

[8] C.E. Aalseth *et al., The IGEX experiment reexamined: A response to the critique of Klapdor-Kleingrothaus, Dietz, and Krivosheina*, Phys. Rev. D 70 (2004) 078302.

[9] Yu.G. Zdesenko *et al., High sensitivity GEM experiment on 2β decay of* ^{76}*Ge*, J. Phys. G 27 (2001) 2129-2146.

[10] H.V. Klapdor-Kleingrothaus, *GENIUS - A New Underground Observatory for Non-Accelerator Particle Physics*, Nucl. Phys. Proc. Suppl. 110 (2002) 364-368.

[11] Majorana Collaboration, *The MAJORANA neutrinoless double-beta decay experiment*, IEEE Nucl. Sci. Symp. Conf. Rec., NSS'08 (2008) 1793-1798.

[12] I. Abt *et al.*, *A new Ge-76 double beta decay experiment at LNGS*, Letter of Intent, [arXiv:hep-ex/0404039].

[13] C. Arnaboldi *et al.* [CUORE Collaboration], *CUORE: a cryogenic underground observatory for rare events*, Nucl. Instrum. Meth. A518 (2004) 775-798.

[14] C. Arnaboldi *et al., Results from a search for the 0νββ-decay of* ^{130}*Te*, Phys. Rev. C 78 (2008) 035502.

[15] K. Zuber, *COBRA—double beta decay searches using CdTe detectors*, Phys. Lett. B, 519 (2001) 1-7.

[16] R. Arnold *et al., Technical design and performance of the NEMO 3 detector*, Nucl. Instrum. Meth. A536 (2005), 79-122.

[17] M. Breidenbach *et al., EXO an advanced Enriched Xenon double-beta decay Observatory*, Letter of Intent, 2001, http://www-project.slac.stanford.edu/exo/docs/EXO_LOI_v3.pdf

[18] N. Ackerman *et al., Observation of Two-Neutrino Double-Beta Decay in ^{136}Xe with the EXO-200 Detector*, Phys. Rev. Lett. 107 (2011) 212501.

[19] Letter from W. Pauli to L. Meitner, Pauli Letter Collection, 4/December/1930, http://cds.cern.ch/record/83282/files/meitner_0393.pdf

[20] C. L. Cowan *et al., Detection of the Free Neutrino: a Confirmation*, Science 124 (1956) 103-104.

[21] M. C. Gonzalez-Garcia and M. Maltoni, *Phenomenology with massive neutrinos*, Physics Reports 460 (2008) 1-129.

[22] Y. Ashie *et al*., *Evidence for an Oscillatory Signature in Atmospheric Neutrino Oscillations*, Phys.Rev.Lett. 93 (2004) 101801.

[23] Q. R. Ahmad *et al., Measurement of Day and Night Neutrino Energy Spectra at SNO and Constraints on Neutrino Mixing Parameters*, Phys.Rev.Lett. 89 (2002) 011302.

[24] T. Araki *et al*. (KamLAND Collaboration), *Measurement of Neutrino Oscillation with KamLAND: Evidence of Spectral Distortion*, Phys.Rev.Lett. 94 (2005) 081801.

[25] M. Goeppert-Mayer*, Double Beta-Disintegration*, Phys. Rev. 48 (1935) 512-516.

[26] J. J. Gómez-Cadenas *et al., The search for neutrinoless double beta decay,* Riv. Nuovo Cim. 35 (2012) 29-98.

[27] Giulio Racah, *Sulla simmetria tra particelle e antiparticelle,* Nuovo Cim. 14 (1937) 322-328.

[28] Ettore Majorana, *Teoria simmetrica dell'elettrone e del positrone,* Nuovo Cim. 14 (1937) 171-184.

[29] W. H Furry, *On Transition Probabilities in Double Beta-Disintegration*, Phys. Rev. 56 (1939) 1184-1193.

[30] J. Schechter and J. W. F. Valle, *Neutrinoless double-β decay in SU(2)×U(1) theories*, Physical Review D25 (1982) 2951-2954.

[31] J. J. Gómez-Cadenas *et al., Sense and sensitivity of double beta decay experiments,* JCAP 06 (2011) 007.

[32]M. Redshaw *et al., Mass and Double-Beta-Decay Q Value of* ^{136}*Xe*, Phys. Rev. Lett. 98 (2007) 053003.

[33] D. Nygren, *High-pressure xenon gas electroluminescent TPC for 0-ν bb-decay search*, Nucl. Instrum. Meth. A603 (2009) 337–348.

[34] N. Ackerman *et al.* (EXO Collaboration), *Observation of Two-Neutrino Double-Beta Decay in* ^{136}*Xe with EXO-200 Detector*, Phys. Rev. Lett. 107 (2011) 212501.

[35] A. Gando *et al.* (KamLAND-Zen Collaboration), *Measurement of the double-beta decay half-life of* ^{136}*Xe with the KamLAND-Zen experiment*, Phys. Rev. C 85 (2012) 045504.

[36] F. T. Avignone, G. S. King and Yu. G. Zdesenko, *Next generation double-beta decay experiments: Metrics for their evaluation*, New J. Phys. 7 (2005) 6.

[37] XENON100 Collaboration, *The XENON100 dark matter experiment*, Astropart. Phys. 35 (2012), 573-590.

[38] D.S. Akerib *et al.,The Large Underground Xenon (LUX) Experiment*, Nucl. Instrum. Meth. A 704 (2013)111-126.

[39] J. C. Vuilleumier *et al., Search for neutrinoless double beta decay in Xe-136 with a time projection chamber*, Phys. Rev. D48 (1993), 1009-1020.

[40] R. Luscher *et al., Search for beta beta decay in Xe-136: New results from the Gotthard experiment*, Phys. Lett. B434 (1998) 407–414.

[41] http://encyclopedia.airliquide.com/encyclopedia.asp

[42] C. A. N. Conde and A. J. P. L. Policarpo, *A gas proportional scintillation counter*, Nucl. Instrum. Meth. 53 (1967), 7-12.

[43] G. Charpak, S. Majewski and F. Sauli, *The scintillating drift chamber: A new tool for high accuracy, very high rate particle localization*, Nucl. Instrum. Meth. 126 (1975) 381-389.

[44] T. Takahashi *et al., Emission spectra from Ar-Xe, Ar-Kr, Ar-*N_2*, Ar-*CH_4*, Ar-*CO_2 *and Xe-*N_2 *gas scintillation proportional counters,* Nucl. Instr. Meth. 205 (1983) 591-596.

[45] C.M.B. Monteiro *et al., Secondary scintillation yield in pure xenon*, 2007 JINST 2 P05001.

[46] L.M.P. Fernandes *et al., Primary and secondary scintillation measurements in a Xenon Gas Proportional Scintillation Counter*, 2010 JINST 5 P09006.

[47] D. Nygren, *Optimal detectors for WIMP and 0–ν ββ searches: Identical high-pressure xenon gas TPCs?,* Nucl. Instr. Meth. A 581 (2007) 632-642.

[48] F. Grañena *et al.* (NEXT Collaboration), NEXT Letter of Intent, http://arxiv.org/abs/0907.4054

[49] Hamamatsu Photonics Inc.; http://www.hamamatsu.com

[50] Y. Giomataris, P. Rebourgeard, J. P. Robert and G. Charpak, *MICROMEGAS: A high-granularity position-sensitive gaseous detector for high particle-flux environments*, Nucl. Instrum. Meth. A376 (1996) 29-35.

[51] I. Giomataris *et al., Micromegas in a bulk,* Nucl. Instrum. Meth. A560 (2006) 405-408.

[52] Y. Giomataris, *Development and prospects of the new gaseous detector "Micromegas"*, Nucl. Instrum. Meth. A419 (1998) 239-250.

2.

ELECTROLUMINESCENCE YIELD AT HIGH PRESSURE XENON GAS

We present results for xenon secondary scintillation yield, at room temperature, as a function of electric field in the gas scintillation gap for pressures ranging from 2 to 10 bar, using a Large Area Avalanche Photodiode (LAAPD) to collect the VUV secondary scintillation produced in the detector. The number of photons produced per drifting electron and per volt, the so-called scintillation amplification parameter, displays a small increase with pressure, ranging from 141±6 at 2 bar to 170±10 at 8 bar. In our study, this parameter does not increase above 8 bar. This is most probably due to non-negligible electron attachment. The results are in good agreement with those presented in the literature in the 1 to 3 bar range. The increase of the scintillation amplification parameter with pressure for high gas densities has been also observed in former work at cryogenic temperatures.

2.1. Introduction

The search for neutrinoless double beta decay (0νββ) is an important topic in contemporary physics with many active experiments. The search for 0νββ with various techniques is now increasingly intensive, and recent developments in detector technology make the observation of 0νββ feasible at the sensitivity scale required to address the question of normal or inverted hierarchy. A very recent detailed review of the 0νββ, including active and planned experiments, is presented in [1].

The search for 0νββ processes is being carried out with different techniques. Germanium calorimeters were proposed for this purpose for the first time by Fiorini [2] and used since then in experiments like Heidelberg-Moscow [3], IGEX [4], GEM [5], GENIUS [6] and GERDA [7]. Cryogenic TeO_2 bolometers are used in CUORE [8] and its smaller prototype, CUORICINO [9]. Others include tracking, such as the NEMO series [10], using a 3-D readout wire drift chamber.

Some projects are planning to use high-pressure xenon gas as both source and detection medium. The secondary scintillation process available in noble gases permits large amplification with negligible statistical fluctuations, offering the prospect of energy resolution approaching the Fano factor limit.

For half a century [11,12] it has been known that secondary scintillation, also called electroluminescence, provides signals with much larger amplitudes, minimal fluctuations in gain and negligible electronic noise, being the optimum amplification technique for this kind of experiments [13]. Therefore, especially in experiments with very low event rates and/or high background levels, as are the 0νββ experiments, it is of great importance to use the secondary scintillation signal rather than the signal from either unamplified primary ionization or secondary ionization [13]. This is the technique to be used in NEXT, with a nominal xenon pressure of 10 bar [14]. A similar project has been submitted to SNO Lab by the EXO Collaboration [15].

The electroluminescence yield is defined as the number of photons produced in the scintillation region per electron crossing the scintillation gap and per unit of path. The interaction of the X-rays in xenon has been extensively studied and the number of electrons resulting from the X-ray interaction is well known. As well as, the direct absorption of X-rays have also been used extensively as a reference to calibrate the number of charge carriers produced in avalanche photodiodes. In this work, X-rays directly absorbed in the LAAPD are used as a reference for determining the number of charge carriers produced by the scintillation pulse and hence the number of secondary scintillation photons impinging the LAAPD.

Absolute electroluminescence yields of xenon [16,17] and argon [18], around atmospheric pressure, have already been measure, with a simple method that makes use of just one experimental setup, without the need for calibration/comparison procedures that are sometimes difficult to carry out and often a source of additional errors. This method has been extensively used to measure the primary scintillation yield in inorganic crystals [19] and it was already used for the determination of the secondary scintillation yield in xenon [16]. The results obtained were in very good agreement, both with experimental results from other groups as well as with Monte Carlo simulation studies and Boltzmann calculations ([16] and references therein).

For higher pressures there were no studies reported in the literature. Favata *et al.* [20], concluded that the reduced electroluminescence yield (i.e. the yield divided by the gas pressure) is pressure-independent, in the region of 1 to 2 bar. Fonseca et al. [21], have shown that the scintillation yield increases only slightly for gas temperature in the range from 20 down to -88ºC and 2 bar pressure (corresponding to 3.2 bar PTN) but, on the other hand, for -90ºC and 2 bar, near the xenon saturation point, the scintillation amplification factor varies significantly.

In this work, we study the behaviour of the xenon electroluminescence yield as a function of electric field in the scintillation region, for xenon pressures from 2 to 10 bar, using the same method applied in [16-18].

2.2. Experimental Setup

The schematic of the gas proportional scintillation counter (GPSC) used in this work is depicted in figure 2.1, which is the same system used in [22]. The detector body has a cylindrical shape with 9 cm in diameter and 3.5 cm in height. Mesh G1 holder is a stainless steel cylinder of 4 cm diameter, and has multiple perforations on its side surface to increase gas circulation in the drift/absorption region.

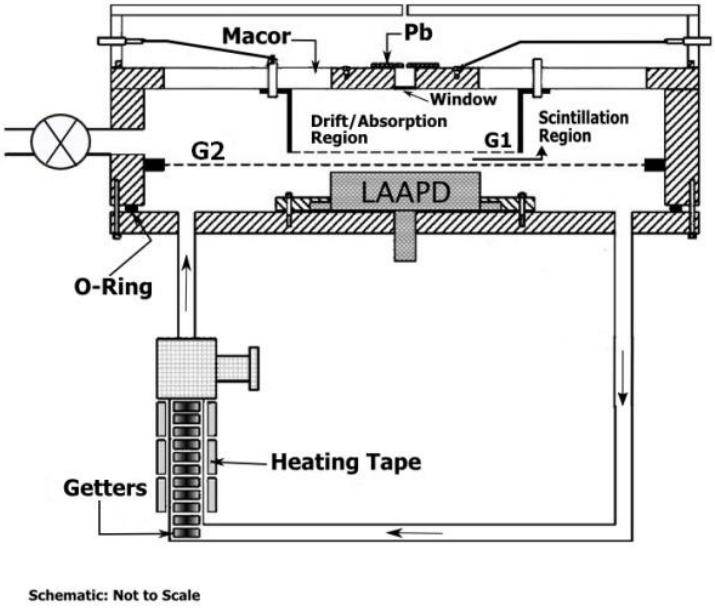

Figure 2.1. Schematic of the GPSC instrumented with a LAAPD.

The radiation window is made of 50-µm Kapton film, aluminised on the inner surface and epoxied to its holder electrode, which is kept at negative high-voltage -HV0, while mesh G1 (80-µm diameter stainless-steel wire with 900-µm spacing) and its holder are kept at -HV1; mesh G2 and detector body are grounded. Electrical insulation of the radiation window and the G1 holder is achieved using a machineable glass-ceramic, Macor®, glued to the detector body and to the window with a low vapour pressure epoxy. The voltage difference between the detector window and G1 defines the

reduced electric field in the absorption/drift region, which is kept below the xenon scintillation threshold, ~ 1 V cm^{-1} $torr^{-1}$ (~ 0.8 kV cm^{-1} bar^{-1}), throughout the work. The scintillation region is delimited by G1 and G2 and the electric field in this region is defined by HV1.

In this GPSC prototype, the absorption/drift region and the scintillation region were designed to be shallow (1-cm deep and 1.5-mm deep, respectively), to keep high reduced electric fields (electric field intensity divided by the gas pressure, E/p) with relatively low biasing-voltages.

Maximum HV0 and HV1 values vary from 3.3 and 1.9 kV to 11.0 and 3.4 kV, as the pressure rises from 2 to 10 bar, respectively. For each pressure, the maximum achieved E/p was limited by electrical insulation and maintained below the onset of electric breakdown, i.e. the appearance of microdischarges, noticeable in the oscilloscope and in the MCA during the pulse-height distribution acquisition.

The LAAPD is a custom made API Deep-UV model with a 16-mm diameter active area [23]. In order to have equal pressure on both sides of the silicon wafer, the LAAPD has several holes 3-mm in diameter throughout its body, connecting the outer surface to the inner chamber, which encloses the electrical contacts with the SHV socket. Throughout this work, the LAAPD biasing was set to a safe value of 1650V, corresponding to a photosensor gain of 25 [23]. Although this biasing voltage corresponds to a low photosensor gain, high performance is already achieved as a result of both high scintillation amplification in the GPSC and high conversion-efficiency of xenon scintillation into charge in the LAAPD [24]. This LAAPD is used to detect, simultaneously, the secondary scintillation of a GPSC and incident X-rays. The X-rays are used as a reference for determining the absolute number of VUV-photons impinging the LAAPD [19].

The detector was filled with xenon at pressures up to 10 bar and the pressure was kept constant during each set of measurements. Xenon circulates through convection, while continuously purified, by non-evaporable getters (SAES Getters, St 707/washer/833) that are kept at a stable temperature in the range 100-250 ºC. We used increasing

temperatures in the getters as the pressure was increased in order to keep the gas purification efficiency.

The charge signals of the LAAPD were fed through a CANBERRA 2006 charge-to-voltage preamplifier (sensitivity of 235 mV/10^6 ion pairs) and a TENNELEC TC243 linear amplifier (1-μs peaking time constant) to a 1024-multichannel analyser. For peak amplitude and energy-resolution measurements, pulse-height distributions were fitted to a Gaussian function superimposed on a linear background, from which the centroid and the FWHM were determined.

2.3. Electroluminescence yield method

Figure 2.2 illustrates the GPSC operation principle. The ionising radiation interacts primarily in the drift/absorption region, where the electric field is lower than the gas electron-impact excitation, i.e. the scintillation threshold (~0.8 kV cm^{-1} bar^{-1}). The resulting primary electron cloud drifts into the scintillation region where the electric field is larger than in the absorption region, but lower than the gas electron-impact ionization threshold (~4.5 kV cm^{-1} bar^{-1}). Upon crossing the scintillation region, electrons gain enough energy from the electric field to excite but not ionize the gas atoms, producing isotropically a large number of VUV photons, as a result of the gas de-excitation processes. A fraction of the produced scintillation photons will reach the LAAPD active-area, and the corresponding electric signal is amplified through the charge-avalanche process in the photodiode.

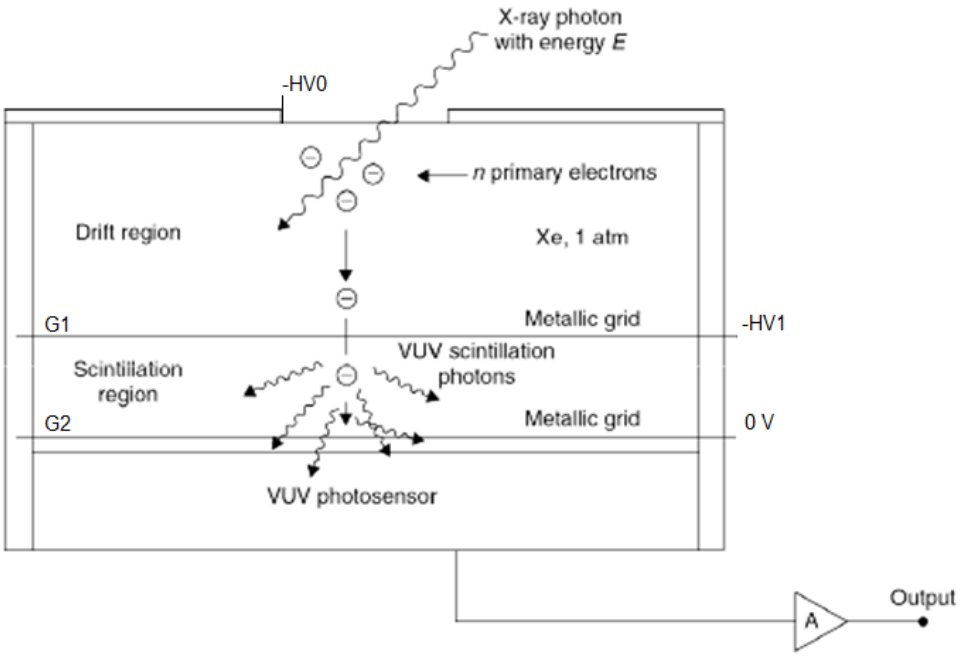

Figure 2.2. The GPSC operation principle.

Upon crossing the scintillation region, the primary electrons gain from the electric field enough energy to excite but not ionise the xenon atoms. As a result of subsequent excimer formation and de-excitation processes, a strong scintillation pulse is generated. The processes leading to emission in the second continuum occur through three-body collisions and can be schematized by

$$Xe^* + 2\,Xe \rightarrow Xe_2^* + Xe \tag{2.1}$$

$$Xe_2^* \rightarrow 2\,Xe + h\upsilon \tag{2.2}$$

One excited atom creates an excited excimer, Xe_2^*, which decays emitting one VUV photon, $h\upsilon$. For pressures above a few tenths of bar the electroluminescence spectrum of xenon consists of a narrow line peaking at 172 nm, with 5 nm FWHM [25].

The electroluminescence yield, *Y*, is defined as the number of secondary scintillation photons produced per drifting primary electron per unit path length.

$$Y = \frac{N_{UV}}{d \times T} \times \frac{4\pi}{\Omega_{Sc}} \times \left(\frac{E_x}{w_{E_x}} \right)^{-1} \tag{2.3}$$

where N_{UV} is the number of VUV-photons impinging the LAAPD per X-ray absorbed in the xenon drift gap, d is the scintillation region length, T is the optical transparency of the grid, Ω_{Sc} is the average solid angle subtended by the LAAPD, E_x is the energy of the incident X-ray and w_{Ex} the respective w-value for xenon. For these LAAPDs, the manufacturer provided a *QE* ~ 1.1 for the number of charge carriers produced in the LAAPD per incident 172-nm VUV photons [24,26]. According to the manufacturer, the LAAPD fabrication technology is well established, and quite good reproducibility is obtained. Therefore, the behaviour observed for individual LAAPDs is expected to be representative for any of these devices, with an uncertainty in *QE* of about ± 10% [27]. For low gains, around 25, the non-linear response of the LAAPD to the X-rays is negligible [28]. The average solid angle, Ω_{sc}, subtended by the active area of the LAAPD for the primary electron path has been computed by Monte Carlo simulation [29]. A value of 4.3 ± 1 sterad was obtained. The *w*-value for xenon, 21.7 eV for 22.1 and 59.6 keV X-rays, was obtained from [30]. Beside the uncertainty in *QE*, another dominating source of uncertainty in the calculated yield is the scintillation gap thickness, *d*, which is limited by the mechanical precision, estimated in, at most, 150 μm, i.e. ± 10% relative error for the scintillation gap thickness. A direct comparison between the amplitudes of the electroluminescence, A_{Sc}, and the X-rays directly absorbed in the LAAPD, A_X, provides a quantification for N_{UV},

$$N_{UV} = \frac{A_{Sc}}{A_X} \times \frac{N_{e,XR}}{QE} \quad \text{photons} \tag{2.4}$$

being $N_{e,XR}$ the number of charge carriers produced in the LAAPD by the direct X-ray interaction. A_{Sc} and A_X are obtained from the pulse height distributions biasing the whole GPSC or only the LAAPD, respectively. $N_{e,XR}$ is calculated from

$$N_{e,XR} = \frac{E_x}{w_{Si}} \text{ electrons} \tag{2.5}$$

where E_x is the energy of the incident X-ray and w_{Si} the respective w-value for silicon. A_{SC} and A_X are obtained with a precision better than ± 1% and ± 2%, respectively. Therefore, the uncertainty obtained for the yield is within ± 15%.

2.4. Experimental Results

The pulse-height distributions obtained with LAAPD readout for the electroluminescence pulses resulting from ^{109}Cd X-rays interacting in xenon and for the X-rays directly interacting in the LAAPD are depicted in figure 2.3. Figure 2.3(b) shows the pulse-height distributions resulting from X-rays directly interacting in the LAAPD. As shown, pulse-amplitudes resulting from electroluminescence depend on the electric field applied to the scintillation region, while pulse-amplitudes resulting from X-rays directly interacting in the LAAPD are independent from drift and scintillation region biasing, depending only on the LAAPD biasing.

Figure 2.4 shows the reduced electroluminescence yield, *Y/p*, i.e. the electroluminescence yield divided by the gas pressure as a function of reduced electric field, *E/p*, in the scintillation region, for pressures up to 10 bar, using 22.1 (figure 2.4(a)) and 59.6 keV (figure 2.4(b)) photons. These results show the characteristic approximately linear trend of electroluminescence dependence on the reduced electric field, having a scintillation threshold around 0.8 kV cm^{-1} bar^{-1}.

For example, for the 5 bar curve in figure 2.4(a),

$$Y/p \text{ (photons electron}^{-1}\text{ cm}^{-1}\text{ bar}^{-1}) = 151\ E/p - 131 \qquad (2.6)$$

where *E/p* is given in kV cm^{-1} bar^{-1}.

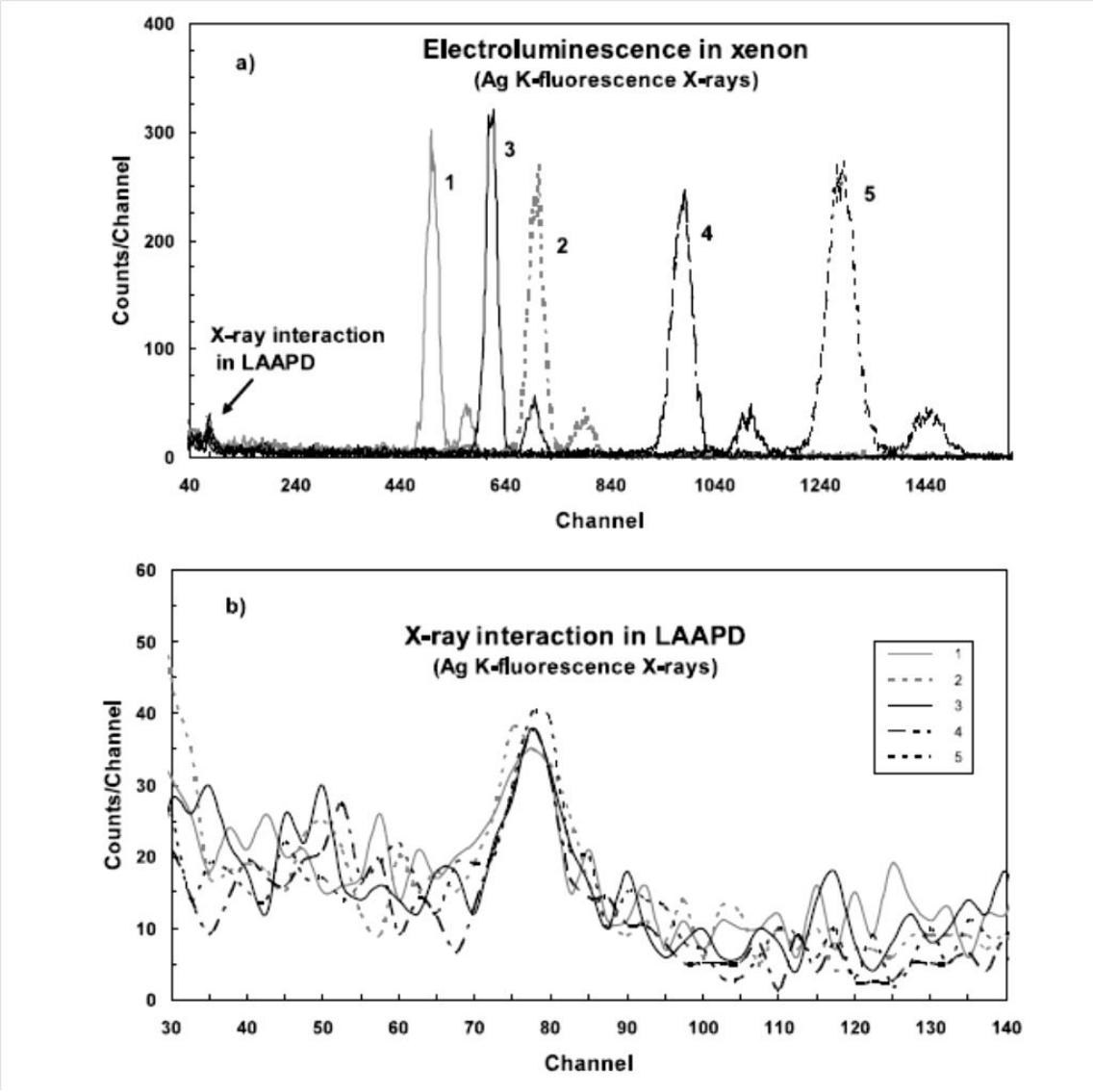

Figure 2.3. (a) Pulse-height distributions from LAAPD readout for electroluminescence resulting from 109Cd X-rays interacting in xenon and for X-rays directly interacting in the LAAPD. (b) details the pulse-height distributions from X-rays directly interacting in the LAAPD. Legend: 1: 2 bar, E/p = 4.8 kVcm^{-1} bar^{-1}; 2: 2 bar, E/p = 6.2 kVcm^{-1} bar^{-1}; 3: 4 bar, E/p = 3.0 kVcm^{-1}bar^{-1}; 4: 4 bar, E/p = 4.4 kVcm^{-1}bar^{-1}; 5: 4 bar, E/p = 5.3 kVcm^{-1}bar^{-1}.

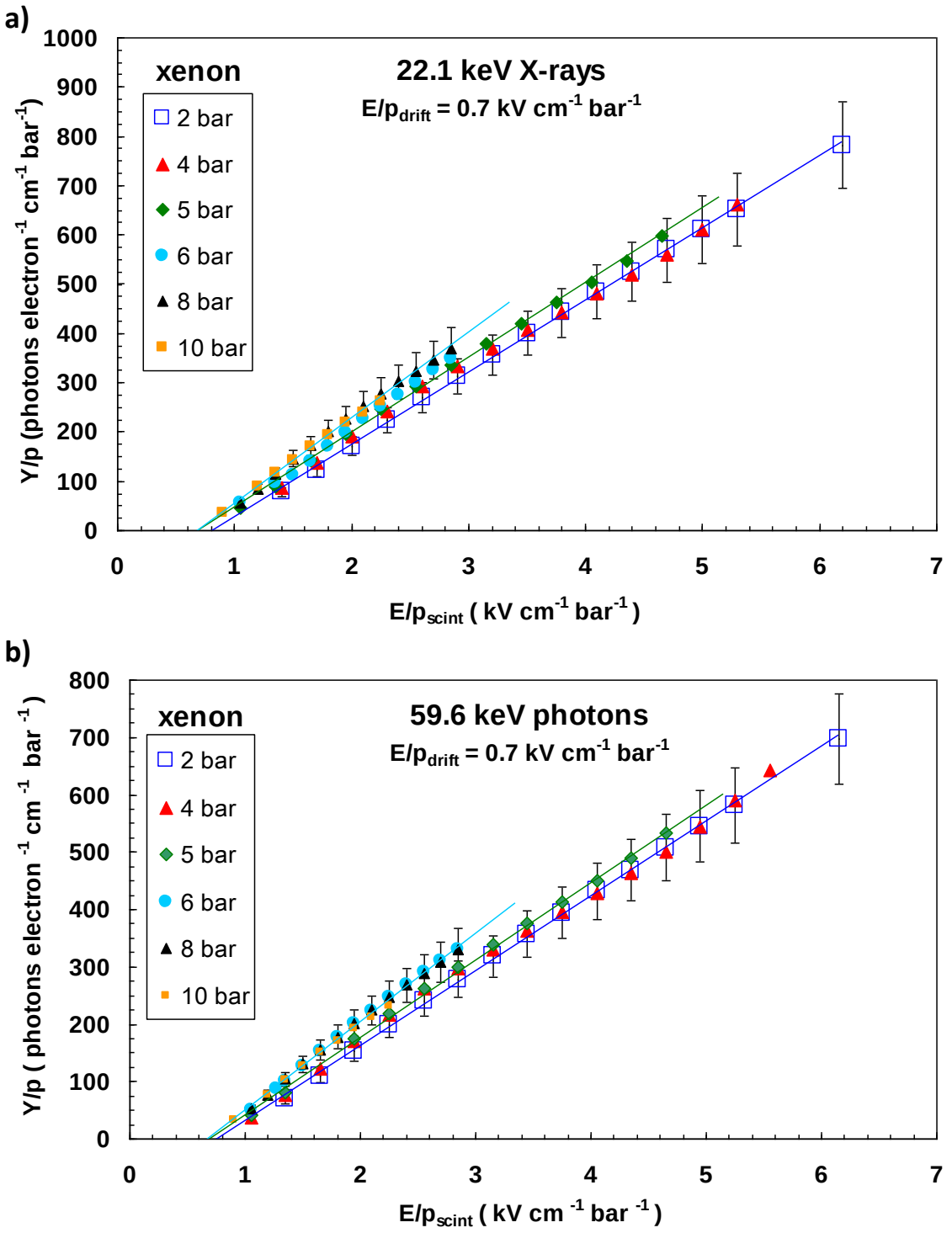

Figure 2.4. Xenon reduced electroluminescence yield as a function of reduced electric field, for different pressures, using 22.1 (a) and 59.6 keV (b) photons. Trend lines are included only to guide the eye.

In Table 1 we list the scintillation amplification parameter, i.e. the number of photons produced per drifting electron and per kilovolt, the slope of the linear trend, obtained for the different xenon pressures. The results agree with those obtained in [16] at 1 bar. The scintillation amplification parameter shows a small increase with pressure, of about 20%. This trend has been observed at cryogenic temperatures for high gas densities [21]. For pressures above 8 bar the increase is marginal; we attribute this effect to non-negligible electron attachment that may occur at higher densities [31]. This effect also explains the degradation in the energy resolution of our detector for higher pressures [22]. The results obtained with the setup of [32], in the range of 2 - 5 bar and using 5.9, 22.1 and 59.6 keV X-rays, have been analyzed using the above described method, rendering values that agree, within errors, with those obtained with the present setup.

The results of the calculation of the average amplification parameters and respective errors, are presented in Table 2.1.

Pressure (bar)	2	3	4	5	6	8	10
Scintillation Amplification Parameter (photons e^{-1} kV^{-1})	141 ± 6	141 ± 7	142 ± 5	151 ± 5	161 ± 9	170 ± 10	162 ± 10

Table 2.1. Xenon scintillation amplification parameter for pressures ranging from 2 to 10 bar.

For each run, e.g. the results presented for 2 bar in figure 2.4(a), a value for the amplification parameter and respective error is obtained from a linear fit to the data points, being the final amplification parameter and error, presented in Table 2.1, determined by weighing averages and respective errors of the different runs performed for each pressure. The differences in errors for the different pressures are mainly due to the number of runs performed for each pressure, e.g. only 2 runs for 6, 8

and 10 bar, while for 2, 4 and 5 bar, 5 runs were performed. We have fit the amplification parameter limiting the range of the reduced electric field in the scintillation region to a maximum of 3 $KVcm^{-1}bar^{-1}$ for all pressures, with similar results.

In our study, we consider the effect of the presence of primary scintillation in the LAAPD output, negligible. Although the primary scintillation is separated in time from the secondary scintillation by less than one microsecond, the electron drift time while crossing the drift region, the number of primary scintillation photons is more than three orders of magnitude lower than that of the secondary scintillation [33].

2.5. Conclusions

We have measured the xenon reduced electroluminescence yield, i.e. the number of secondary scintillation photons produced per drifting primary electron per unit path length, as a function of the reduced electric field, for different pressures between 2 and 10 bar. The measurements were performed using a gas proportional scintillation counter (GPSC) instrumented with a large area avalanche photodiode for the electroluminescence readout. Direct interactions of 22.1 keV X-rays in the LAAPD were used as a reference for the determination of the number of charge carriers produced by the scintillation pulse and, thus, the number of VUV photons impinging the photodiode, given its quantum efficiency.

The measurements have shown that the number of photons produced per drifting electron and per kilovolt, the so-called scintillation amplification parameter, presents a small increase with pressure, increasing from 141±6 at 2 bar to 170±10 at 8 bar. The increase with pressure is significant since most of the systematic errors are common to both points. Above 8 bar the amplification parameter does not increase; we attribute this effect to non-negligible electron attachment that occurs at higher densities. The results are in good agreement with former results presented in the literature in the 1

to 3 bar range. The increase of the scintillation amplification parameter with pressure for high gas densities was also observed in former work at cryogenic temperatures [21].

References

[1] J. J. Gómez-Cadenas *et al., Sense and sensitivity of double beta decay experiments,* JCAP 06 (2011) 007.

[2] E. Fiorini *et al., A search for lepton non-conservation in double beta decay with a germanium detector*, Phys. Lett. B25 (1967) 602-603.

[3] H.V. Klapdor-Kleingrothaus *et al.*, *Latest results from the Heidelberg-Moscow double beta decay experiment*, Eur. Phys. J. A 12 (2001) 147-154.

[4] C.E. Aalseth *et al., The IGEX experiment reexamined: A response to the critique of Klapdor-Kleingrothaus, Dietz, and Krivosheina*, Phys. Rev. D 70 (2004) 078302.

[5] Yu.G. Zdesenko *et al., High sensitivity GEM experiment on 2β decay of* ^{76}*Ge*, J. Phys. G 27 (2001) 2129-2146.

[6] H.V. Klapdor-Kleingrothaus, *GENIUS - A New Underground Observatory for Non-Accelerator Particle Physics*, Nucl. Phys. Proc. Suppl. 110 (2002) 364-368.

[7] S. Schönert *et al., Status of the Germanium Detector Array (GERDA) in the search of neutrinoless ββ decays of* ^{76}*Ge at LNGS*, Phys. Atom. Nucl. 69 (2006) 2101-2108.

[8] M. Pedretti *et al., CUORE Experiment: The search for neutrinoless double beta decay*, Int. J. Mod. Phys. A 23 (2008) 3395-3398.

[9] C. Arnaboldi *et al., Results from a search for the 0νββ-decay of* ^{130}*Te*, Phys. Rev. C 78 (2008) 035502.

[10] R. Arnold *et al.* (NEMO Collaboration), *Measurement of double beta decay of* ^{100}*Mo to excited states in the NEMO 3 experiment*, Nucl. Phys. A 781 (2007) 209-226.

[11] C. A. N. Conde and A. J. P. L. Policarpo, *A gas proportional scintillation counter*, Nucl. Instrum. Meth. 53 (1967), 7-12.

[12] A. S. Conceição *et al., GEM scintillation readout with avalanche photodiodes,* 2007 JINST 2 P09010.

[13] D. Nygren, *Optimal detectors for WIMP and 0–ν ββ searches: Identical high-pressure xenon gas TPCs?,* Nucl. Instr. Meth. A 581 (2007) 632-642.

[14] F. Grañena *et al.* (NEXT Collaboration), NEXT Letter of Intent, http://arxiv.org/abs/0907.4054

[15] D. Sinclair, "Progress on a Gaseous Xe detector for Double Beta Decay (EXO)", Workshop on Xenon-Based Detectors, Berkeley, USA, 16-18 November 2009. http://indico.cern.ch/conferenceOtherViews.py?view=standard&confId=66513.

[16] C.M.B. Monteiro *et al., Secondary scintillation yield in pure xenon*, 2007 JINST 2 P05001.

[17] C.M.B. Monteiro *et al., Secondary scintillation yield from gaseous micropattern electron multipliers in direct dark matter detection*, Phys. Lett. B 677 (2009) 133-138.

[18] C.M.B. Monteiro, J.A.M. Lopes, J.F. C.A. Veloso and J.M.F. dos Santos, *Secondary scintillation yield in pure argon*, Phys. Lett. B 668 (2008) 167-170.

[19] M. Moszynski, M. Szawlowski, M. Kapusta and M. Balcerzyk*, Large area avalanche photodiodes in scintillation and X-rays detection*, Nucl. Instrum. Meth. A 485 (2002) 504-521.

[20] F. Favata *et al., Light yield as a function of gas pressure and electric field in gas scintillation proportional counters*, Nucl. Instrum. Meth. A 294 (1990) 595-601.

[21] A.C. Fonseca, R. Meleiro, V. Chepel, A. Pereira, V. Solovov and M.I. Lopes, *Study of Secondary Scintillation in Xenon Vapour,* 2004 IEEE Nucl. Sci. Symp. Conference Record, vol.1, 572-576.

[22] L.C.C. Coelho, *et al., Xenon GPSC high-pressure operation with a large-area avalanche photodiode readout*, Nucl. Instrum. Meth. A 575 (2007) 444-448.

[23] Deep UV 500 Windowless Series LAAPD, Advanced Photonics Inc., 1240 Avenida Acaso, Camarillo, CA 93012, U.S.A.; http://www.advancedphotonix.com/

[24] J.A.M. Lopes *et al., A xenon gas proportional scintillation counter with a UV-sensitive large-area avalanche photodiode*, IEEE Trans. Nucl. Sci. 48 (2001) 312-319.

[25] T. Takahashi *et al., Emission spectra from Ar-Xe, Ar-Kr, Ar-N_2, Ar-CH_4, Ar-CO_2 and Xe-N_2 gas scintillation proportional counters,* Nucl. Instrum. Meth. 205 (1983) 591-596.

[26] B. Zhou and M. Szawlowski, *An explanation on the APD spectral quantum efficiency in the deep UV range*, Interoffice Memo, Advanced Photonix Inc., 1240 Avenida Acaso, Camarillo, CA 93012, U.S.A., 1999.

[27] M. Szawlowski, Advanced Photonix Inc., private communication (2002).

[28] M. Moszynski *et al., Large Area Avalanche Photodiodes in X-rays and scintillation detection*, Nucl. Instrum. Meth A 442 (2000) 230-237.

[29] J.M.F. dos Santos, A.C.S.M. Bento and C.A.N. Conde, *The dependence of the energy resolution of gas proportional scintillation counters on the scintillation region to photomultiplier distance*, IEEE Trans. Nucl. Sci. 39 (1992) 541-545.

[30] T.H.V.T. Dias *et al., Full-energy absorption of X-ray energies near the Xe L-and K-photoionization thresholds in xenon gas detectors: Simulation and experimental results*, J. Appl. Phys. 82 (1997) 2742-2753.

[31] A. Bolozdynya *et al., A high pressure xenon self-triggered scintillation drift chamber with 3D sensitivity in the range of 20–140 keV deposited energy*, Nucl. Intrum. Meth. A 385 (1997) 225-238.

[32] D.S. Covita *et al., High-pressure xenon GPSC/LAAPD for x-ray spectrometry,* IEEE Trans. Nucl. Sci. 51 (2004) 1492-1496.

[33] L.M.P. Fernandes *et al., Primary and secondary scintillation measurements in a Xenon Gas Proportional Scintillation Counter*, 2010 JINST 5 P09006.

3.

STUDY OF THE CHARACTERISTICS OF HAMAMATSU S8664 APD FOR XENON ELECTROLUMINESCENCE DETECTION

We investigated the operation of the S8664-SPL Avalanche Photodiode (APD) from Hamamatsu to xenon scintillation light and to direct X-rays of 22.1 keV and 5.9 keV. A large non-linear response was observed for the direct X-ray detection. For a APD bias voltage of 415 V, the non-linearity response factor was about 0.3 for 22.1 keV and about 0.45 for 5.9 keV X-rays. The quantum efficiency of this type of APD and for 172nm photons it was measured to be 69 ±15 %.

3.1. Introduction

Avalanche Photodiodes (APDs) are compact and low power consumption devices made of silicon p-n junctions. They are able to detect light from the infrared region to the Vacuum UltraViolet (VUV), and X-rays with energy up to about 25 keV, depending on the internal structure. Although their performance in the response to direct X-rays can be similar or even better than that of proportional counters, low-energy X-ray

detection techniques with APDs were mainly developed to measure the number of charge carriers released by X-rays in scintillation counters. In this chapter, we investigated the performance of the S8664-55 SPL APD from Hamamatsu as a VUV photosensor for the xenon VUV scintillation, using a Gas Proportional Scintillation Counter (GPSC).

Avalanche photodiodes (APDs) have proven to be a good alternative to photomultiplier tubes (PMTs) in visible and VUV photon detection [1,2]. They are compact, consume small amounts of power and are simple to operate. APDs also present high quantum efficiency, acceptable gain, insensitivity to intense magnetic fields, resistance to high-pressure environments and low degassing properties. In particular, their low radioactivity contamination is attractive for low background experiments based on xenon, such as direct dark matter searches (XENON [3], ZEPLIN [4]) and neutrinoless double beta decay searches (EXO [5], NEXT [6]), where the radiopurity of the photosensors is of critical importance. High pressure TPCs based on xenon [6–8] are being considered for the detection of the neutrinoless double beta decay. Gas detectors present several advantages over the liquid option. Gaseous xenon detectors have better intrinsic energy resolution [9] than the liquid and the low density media allows to track the electrons emitted from the double beta decay, reducing the background contamination through topological constraints. Previous studies show that the operation of the detector in the so-called electroluminescence regime allows to obtain resolutions close to the ones of the primary electron fluctuations. Electroluminescence is achieved by accelerating the primary electrons in the xenon to an energy that produces scintillation light without entering into the charge amplification regime. This technique is well established for xenon with photomultipliers [10] and APD [11] readouts.

In this chapter we evaluate the performance of the Hamamatsu S8664-SPL Avalanche Photodiode sensor for the Xe electroluminescence readout. This APD is a special version of the standard product, made sensitive to xenon (172 nm) and argon (128 nm) scintillating light. The APD is available in two different sizes (5x5mm^2 and 10x10mm^2).

The small size of the sensor allows to explore the possibility of using this technology for energy measurement and tracking when laying them as an array of sensors with independent readouts [12]. We will obtain an independent measurement of the quantum efficiency for 172 nm photons for these devices and a measurement of their response to direct X-rays of 22.1 keV and 5.9 keV. The X-ray detection with APDs has been used to measure the charge carriers produced in light measurements, using the number of charge carriers produced by the X-ray interaction in the APDs as a reference, resulting in a straight forward process to evaluate the number of charge carriers produced in the APD by the light pulse. This method has been extensively used to measure the scintillation yield in inorganic crystals [14] and in noble gases [15], as well as to determine the quantum efficiency of APDs [16–18]. However, non-linearities in the APD response to X-rays have to be taken into account. This effect has been studied for the standard S8664 type APDs [19–21], but not yet for the present type. Therefore, the non-linear response to X-rays has to be investigated for a full characterization of the present type of photodiodes.

3.2. Experimental setup

Figure 3.1 depicts the schematic of the GPSC used, as well a photograph of the detector with the APD used in this work. The detector body has a cylindrical shape with 14 cm in diameter and 5 cm in height, with a 2 mm aluminized Kapton detector radiation window. Mesh G1 holder is a stainless steel cylinder of 6 cm diameter, and has multiple perforations on its side surface to increase gas circulation in the drift/absorption region. The radiation window is kept at negative high-voltage −HV0, while mesh G1 and its holder are kept at −HV1; mesh G2 and detector body are grounded. Electrical insulation of the radiation window and the G1 holder is achieved using a machineable glass ceramic, Macor®, glued to the detector body and to the X-ray window with a low vapour pressure epoxy. The voltage difference between the

detector window and G1 defines the electric field in the absorption/drift region, which is kept below the xenon scintillation threshold, ~ 1 V $cm^{-1}torr^{-1}$. The scintillation region is delimited by G1 and G2. The electric field in this region is defined by −HV1. In this GPSC prototype, the absorption/drift region and the scintillation region were designed to be 2 cm and 1.4 cm deep, respectively, and the detector is operated at a pressure of 800 torr of xenon that was continuously purified through St707 SAES getters at ~120ºC. The active area of the photodiode was positioned 4.7 mm below grid G2. G1 and G2 are highly transparent stainless steel meshes, 80 µm diameter wire with a 900 µm spacing.

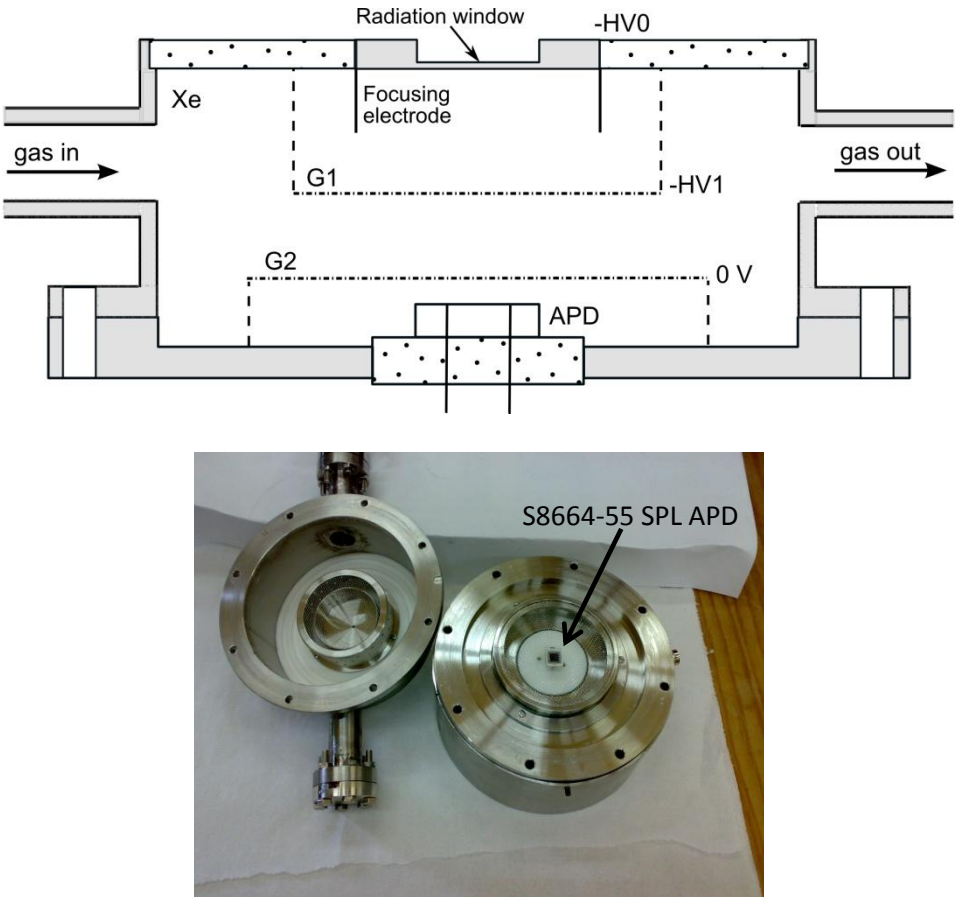

Figure 3.1. Schematics and picture of the GPSC used in this work, with the S8664-SPL APD used as VUV scintillation photosensor.

The VUV photodiode signals were fed through a low-noise charge pre-amplifier (CANBERRA 2004) and an amplifier with a shaping time of 4 μs, to a 1024-channel MCA. For pulse amplitude and energy-resolution measurements, the x-ray pulse-height distributions were fitted to a gaussian function superimposed on a linear background, from which the centroid and the full-width-at-half-maximum were determined.

X-rays interacting in the drift region produce a primary electron cloud that drifts toward the scintillation region. Upon crossing the scintillation region, each primary electron produces, in average, a known number of scintillation photons [22]. X-ray interactions in the scintillation region will lead to scintillation pulses with lower amplitudes. These pulses result in a distortion of the Gaussian-shape pulse height distribution with a tail toward the low amplitude region. However, the peak of the pulse height distribution is not altered by this tail. A fraction of the X-rays interact in the APD, producing a pulse height distribution that is independent of the electric fields of the GPSC, depending only on the APD biasing.

3.3. Experimental results

We investigated the response of the Hamamatsu S8664-55 SPL APD to the electroluminescence produced within the xenon GPSC. The amplitude and energy resolution of the scintillation pulses produced in the xenon by the interaction of 22.1 keV X-rays from a ^{109}Cd radioactive source were determined for different electric fields in the drift and scintillation regions of the GPSC, for gas pressures of 800 torr.

Typical pulse-height distributions obtained for ^{109}Cd X-rays are depicted in figure 3.2. The pulse-height distributions were obtained at 800 torr for different reduced electric fields in the GPSC scintillation region, while keeping a reduced electric field of 0.2 V cm^{-1} torr^{-1} in the drift region, and for a APD bias voltage of 415 V. The best energy resolution of 18% (FWHM) for the 22.1 keV X-ray peak was obtained for a reduced electric field of 5.0 V cm^{-1} torr^{-1} in the scintillation region, figure 3.2(b).

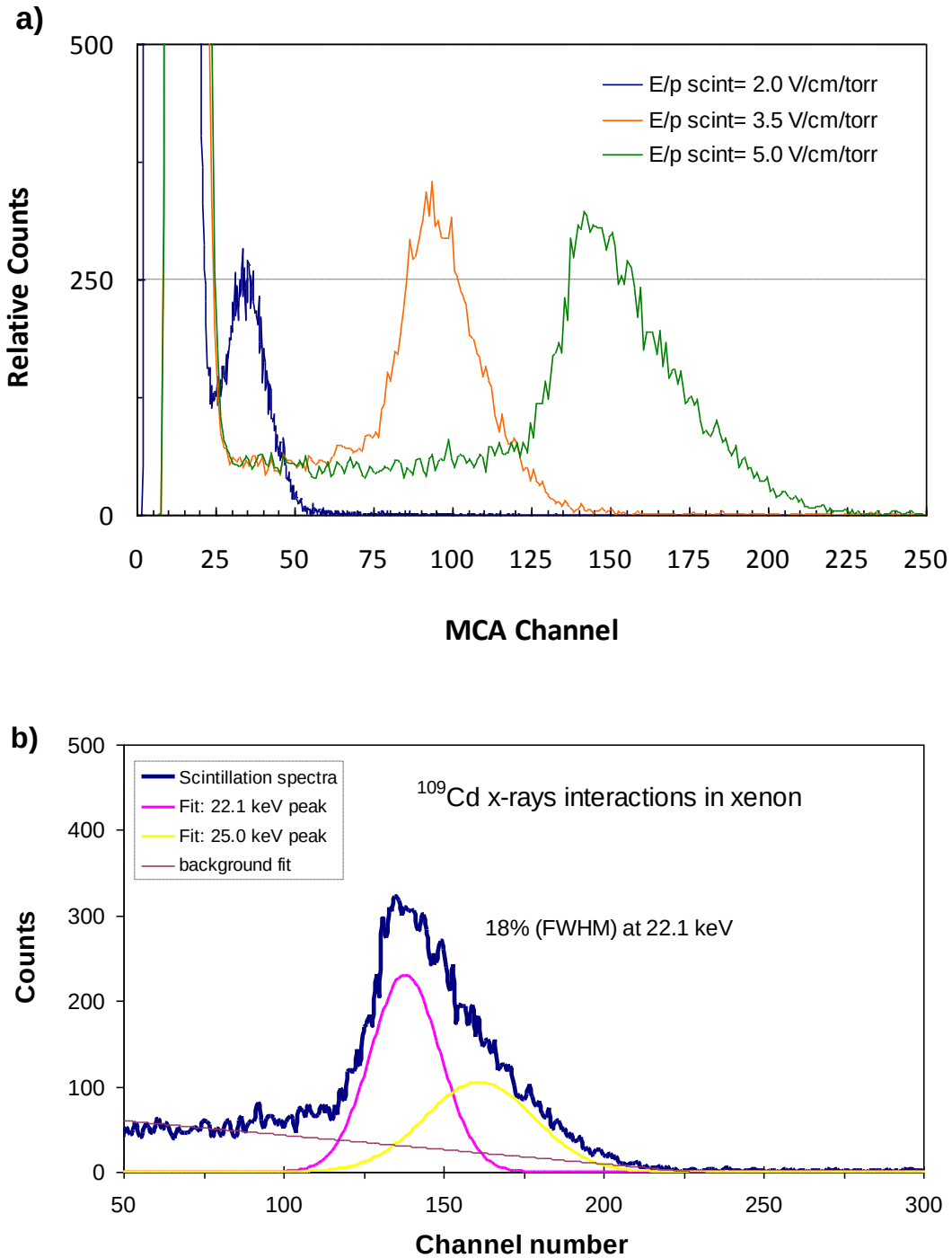

Figure 3.2. Typical pulse-height distributions of ^{109}Cd X-ray interactions in xenon: (a) for different reduced electric fields in the scintillation region, while keeping the drift reduced electric field at 0.2 Vcm^{-1}torr^{-1} and (b) gaussian fits to the ^{109}Ag K-lines for the pulse height distribution obtained for a scintillation field of 5.0 Vcm^{-1}torr^{-1}.

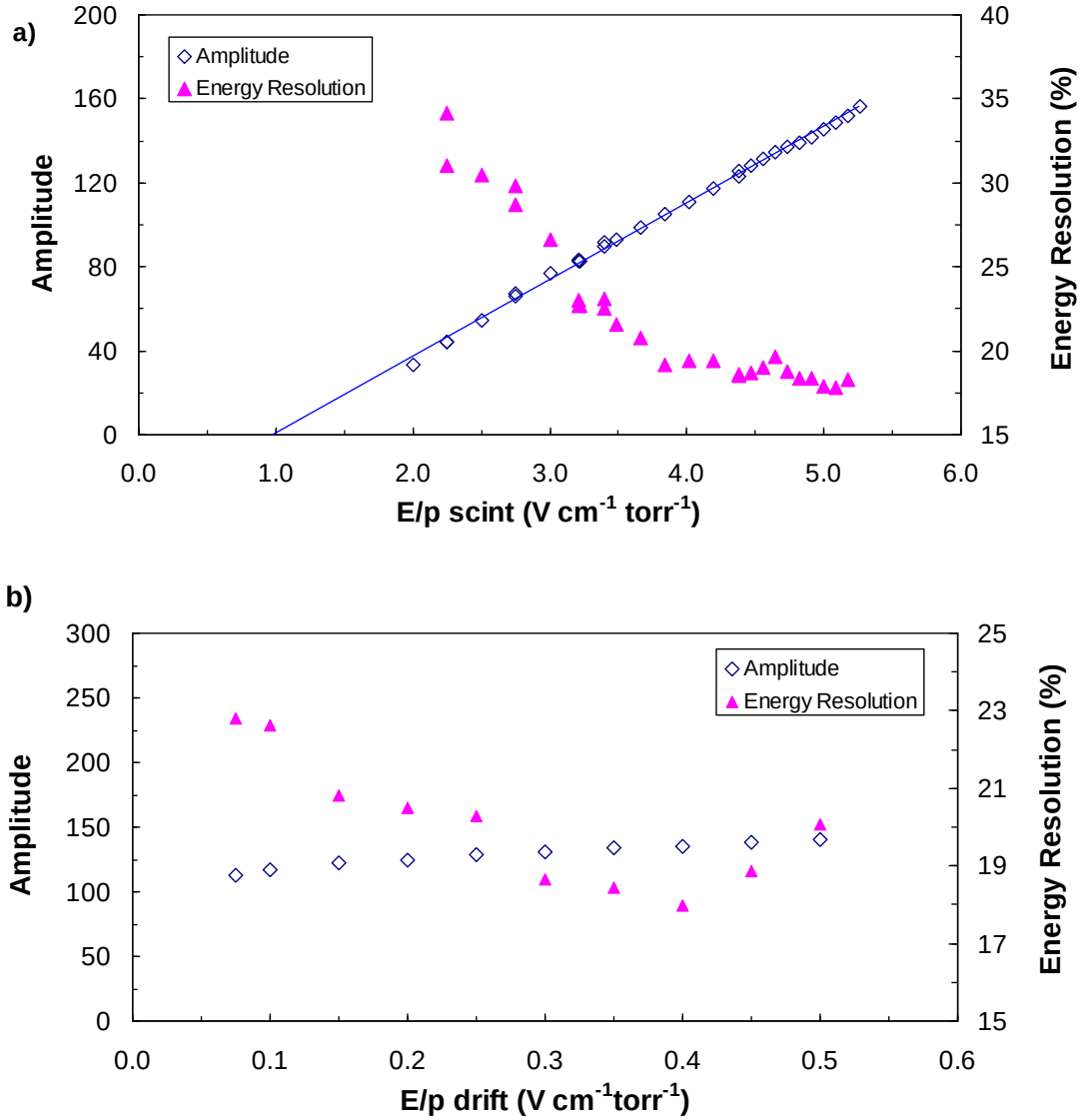

Figure 3.3. Relative amplitude and energy resolution for 22.1 keV X-rays absorbed in the GPSC as a function of: (a) E/p-scint, the reduced electric field in the scintillation region; (b) E/p-drift, the reduced electric field in the drift region. In (a), a fixed electric field of 0.2 V cm^{-1} $torr^{-1}$ was used in the drift region. In (b), a scintillation electric field of 4.4 V cm^{-1} $torr^{-1}$ was used. In both, the APD was biased to 415 V.

The dependence of the amplitude and energy resolution on the reduced electric field applied to the scintillation region is shown in figure 3.3(a), while the dependence on the drift electric field is shown in figure 3.3(b). Figure 3.3 shows that E/p-scint has to be larger than 4 V cm^{-1} $torr^{-1}$ in order to get the best energy resolution, while E/p-drift

has to be larger than 0.2 cm^{-1} $torr^{-1}$. The scintillation output shows the typical linear dependence on the electric field with a threshold at 1.0 Vcm^{-1} $torr^{-1}$, figure 3.3(a).

3.4. Quantum efficiency determination

The quantum efficiency (QE) of the APD was determined, using the method established in [22], by a direct comparison between the pulse amplitudes of the electroluminescence, A_{Sc}, with those resulting from direct interactions of the X-rays in the photodiode, A_X. The total number of VUV photons produced in the scintillation region, N_{UV}^{total}, is calculated from

$$N_{UV}^{total} = N_{elec} G = \frac{E_x}{w_x} G \tag{3.1}$$

where G is the electroluminescence phase gain, and N_{elec} is the number of primary electrons. This number can be obtained by dividing the energy of the incident X-rays, E_x, by the average energy needed to produce an electron–ion pair in xenon, w_x,(for 22 kev X-ray interactions in xenon the w-value is 21.7 eV [23]). From Ref. [22], the electroluminescence yield per cm per bar, Y/p, is given by

$$\frac{Y}{p} = 140 \frac{E}{p} - 116 \tag{3.2}$$

where, E/p is the reduced electric field in the scintillation region, in kV cm^{-1} bar^{-1}.

Therefore, the gain G can be defined as

$$G = \frac{Y}{p}\, p\, d \tag{3.3}$$

where d, is the scintillation region depth in cm, and p is the operation pressure in bar. For ^{109}Cd, d=1.4 cm, p=1.07 bar (800 torr) and for a scintillation reduced electric field

of E/p=3.75 kVcm^{-1}bar^{-1} (5.0 V cm^{-1} torr^{-1}), the total number of VUV photons produced is about 622 000. The number of photons arriving to the APD, N_{UV}, is derived from the total number of photons emitted in 4π and the average solid angle, Ω_{sc}, subtended by the active area of the APD.

$$N_{UV} = N_{UV}^{total} \frac{\Omega_{sc}}{4\pi} T \tag{3.4}$$

The average solid angle Ω_{sc} and the optical transparency of the grid G2 *T,* were estimated from a Monte Carlo simulation implemented by our collaborators in IFAE, Barcelona. The quantum efficiency QE, defined as the number of free electrons produced in the APD, $N_{e,sci}$, per VUV photon, can be calculated from

$$QE = \frac{N_{e,sci}}{N_{UV}} \tag{3.5}$$

$$QE = \frac{A_{sc}}{A_X} \frac{N_{e,XR}}{N_{UV}} \tag{3.6}$$

where, A_{sc} and A_X are respectively, the peak position of the electroluminescence response and the direct X-ray peak in the pulse-height spectrum. $N_{e,XR}$ is the number of charge carriers produced in the APD by the direct absorption of a X-ray. $N_{e,XR}$ can be calculated from the incident X-ray energy, E_X (22.1 keV for ^{109}Cd), from the energy needed to produce an electron–ion pair in silicon, w_{Si} (w-value for Si 3.62 eV [24]), NL are the non-linearities and NLR_f a non-linearity response factor

$$N_{e,XR} = \frac{E_X}{w_{Si}}(1 - NL) \tag{3.7}$$

$$N_{e,XR} = \frac{E_X}{w_{Si}} NLR_f \tag{3.8}$$

Where, the non-linearity response depends on the type of APD, the applied bias voltage and the X-ray energy.

Pulse-amplitudes resulting from electroluminescence depend on the electric field applied to the scintillation region. On the other hand, the pulse-amplitudes resulting from X-rays directly interacting in the APD are independent from drift and scintillation region electric fields, depending only on the APD biasing. Therefore, we have determined A_x in the same setup as in section 3.3 for the same biasing voltages of the LAAPD, 415 V. Figure 3.4 shows the pulse-height distributions resulting from X-rays directly interacting in the APD, with no electric fields applied on the GPSC and for 415 V applied to the photodiode. The mean of this distribution was used for the determination of A_x.

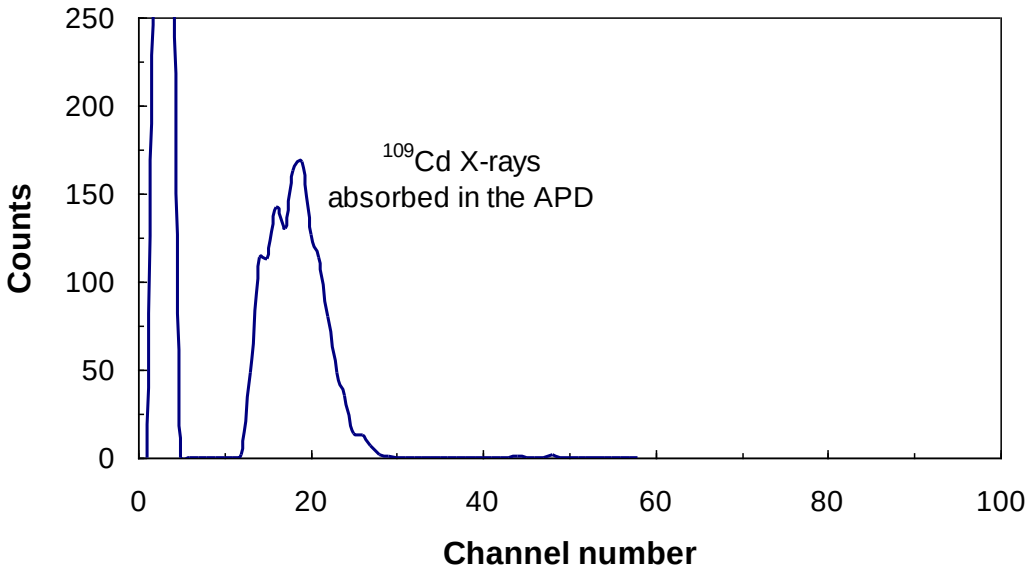

Figure 3.4. Pulse-height distribution for X-rays interacting directly in the APD. The APD was biased at 415 V.

3.5. The non-linearity response to X-rays

In light detection we are dealing with pulses resulting for the overall interaction of a great number of photons: The fact that the absorption length is larger for a given wavelength means that the number of photons interacting deeper in the APD is larger and their contribution to the overall avalanche amplification becomes lower for the

interactions taking place inside the multiplication region; longer wavelength result in lower overall gains [20,25,26].

On the other hand for x-rays, no matter the absorption length for a specific X-ray energy a photon interacting in the region before the multiplication region results in a full amplitude event, while those interacting inside the multiplication region results in lesser amplitude events, contributing to the distortion of the "full-gain" peak in the form of a low energy tail that extends to zero energy. The longer the absorption length for a given X-ray energy, the higher is the fraction of the tail area compared to the peak area. The gain for photons interacting behind the multiplication region results from hole multiplication and it is too low to "disturb" the peak distribution, for the Hamamatsu reversed type models it is below or around 2, i.e. almost two orders of magnitude lower [21]. The fact that the multiplication region is only 5 microns away from the window (the p-n junction is at 7 microns) affects the counting efficiency for the peak (full gain) events but, judging from the internal structure of the S8864 APDs (see e.g. in Refs. [25] and [27]), the multiplication region thickness is even smaller. Taking into account the exponential behaviour of X-ray absorption and the fact that the area of the tail extends from the peak centroid to almost zero energy, the "full gain" peak is not such distorted and the peak centroid is easy to determine, as can be seen in figure 3.5 and figure 3.6.

On the other hand, the point-like nature of the primary electron cloud produced by the X-ray interaction in the APD leads to non-linearities in the APD response to X-rays that have to be taken into account. The effective gain of the APD for the X-ray pulses decrease with increasing APD biasing voltage, i.e. the A_{sc}/A_X ratio increases with increasing APD voltage. These non-linearities are due to space charge effects in the avalanche volume, resulting in a reduction of the local electric field intensity, and in local heating, due to the high charge concentration in that volume [26,28,29]. Therefore, the non-linear response to X-rays has to be investigated for a full characterization of the present photodiodes and correct determination of the APD QE.

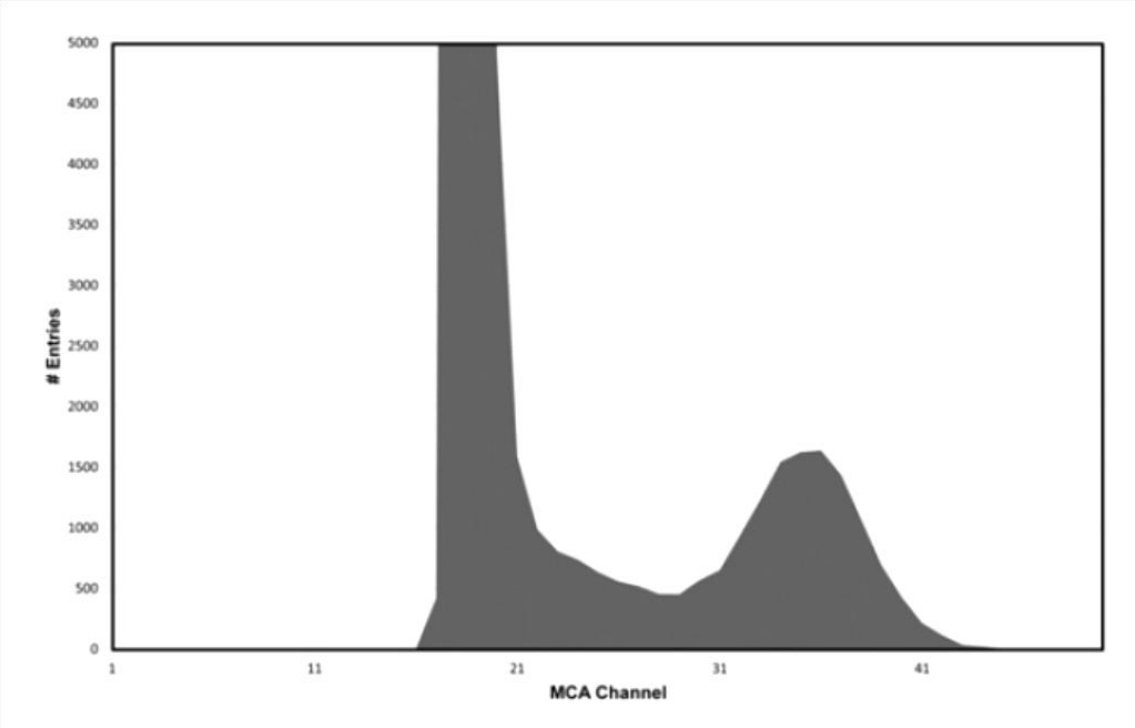

Figure 3.5. Pulse-height distribution for ^{55}Fe X-rays interacting directly in the APD, with the APD biased at 360 V (data taken by our colleagues at IFAE).

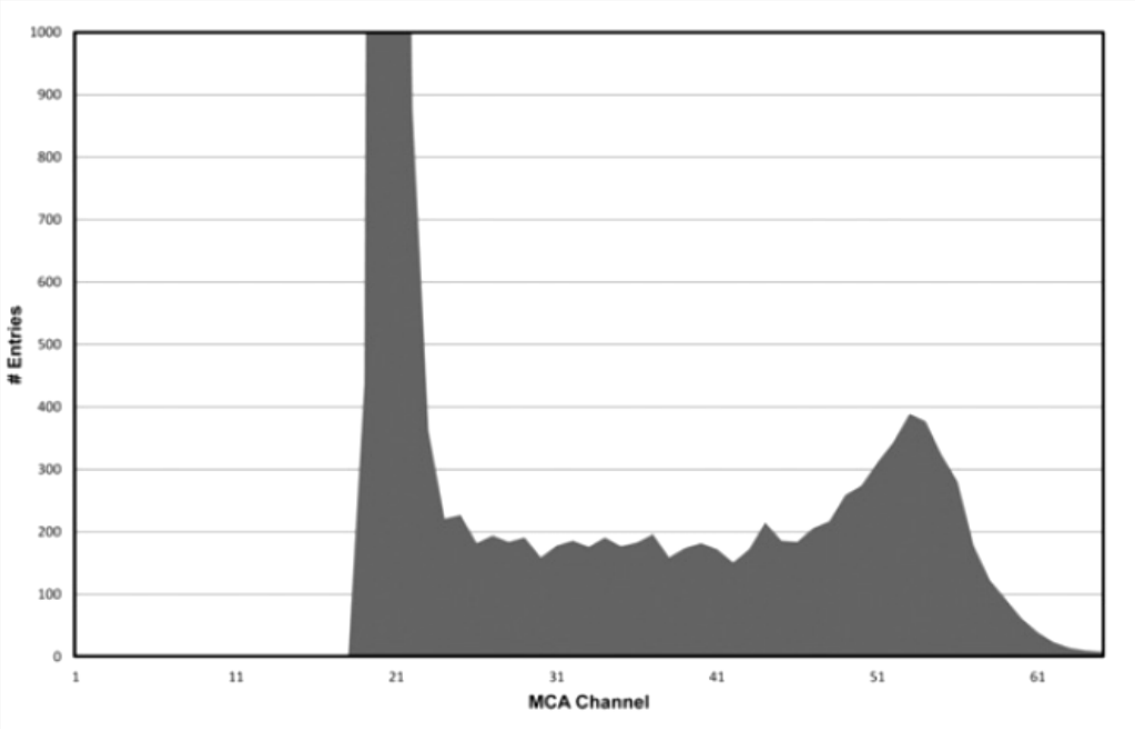

Figure 3.6. Pulse-height distribution for ^{109}Cd X-rays interacting directly in the APD, with the APD biased at 325 V (data taken by our colleagues at IFAE).

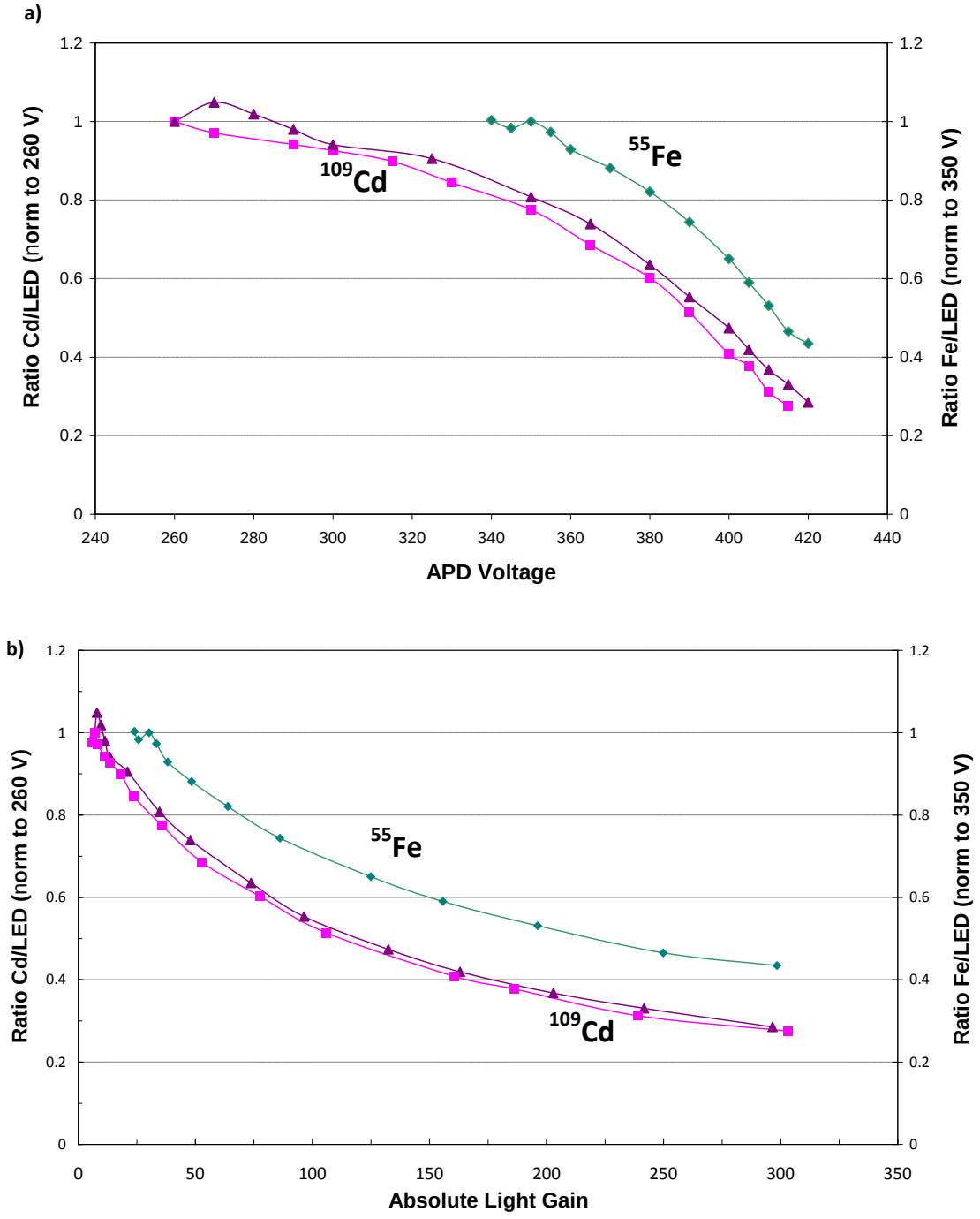

Figure 3.7. Ratio of direct X-ray interaction peak position and LED peak position as a function of the APD bias voltage (a) and as a function of the absolute light gain (b).The interactions resulting from the 22.1 keV X-rays of the ^{109}Cd source are shown for two APDs, normalized to the value at 260 V; the interactions of the 5.9 keV from the ^{55}Fe source (green line) were normalized to the value at 350 V.

The non-linear response to X-rays was measured for this type of VUV-sensitive APDs, following the method described in [14]. These experimental results were obtained by our Colleagues at IFAE, Barcelona, within the NEXT Collaboration, and are described in the Appendix A.

In figure 3.7, the APD non-linearities for ^{55}Fe and ^{109}Cd X-rays are shown as a function of the APD bias voltage (figure 3.7(a)) and as a function the APD absolute gain for light pulses (figure 3.7(b)).

Below APD biasing voltages of 260 V, for 22.1 keV and of 340 V for 5.9 keV X-rays, the APD response for the X-rays direct interactions were superimposed in the noise background. The non-linearity response factor of this APD for a bias voltage of 415 V, is 0.29±0.04 for 22.1 keV and 0.46±0.07 for 5.9 keV X-rays. These values are significantly lower than the ones obtained with APDs from Advanced Photonics Inc. (API), 0.87 and 0.93, respectively, for the highest biasing voltages of the LAAPD [11,30]. The lower numbers indicate that these devices are less suitable for direct X-ray detection, as also referred to in Refs. [19–21]. This type of APD design has been developed to improve the APD characteristics for light detection. While for the 22.1 keV X-rays there are no other results available, the obtained results for the non-linearity on the APD response to 5.9 keV X-rays are similar to those obtained in the literature [19–21] for the standard APD. This was expected since the internal structure and electric field profile of the S8664 APD, figure 3.8, are maintained on the VUV-sensitive type of APD (S8864 SPL), only the window has been removed to make it sensitive to VUV.

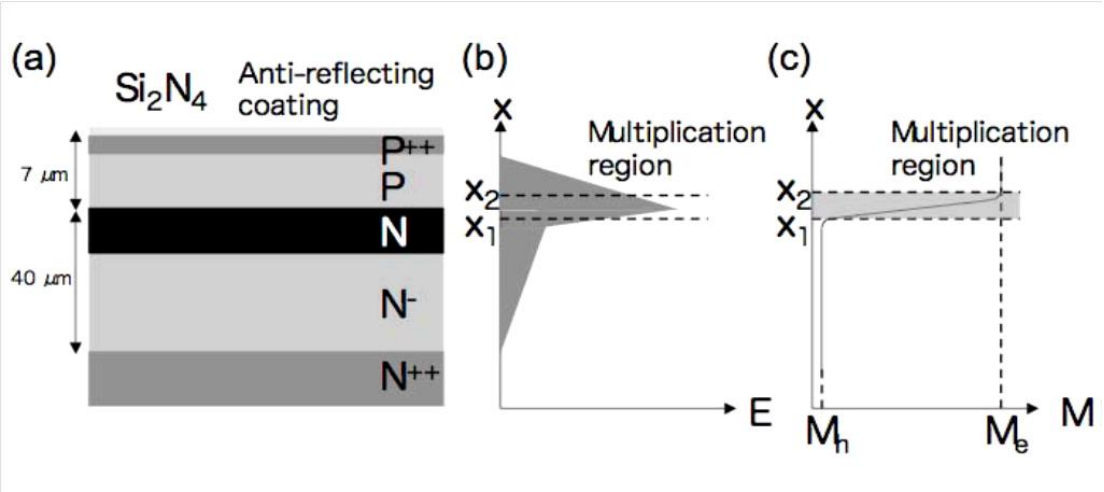

Figure 3.8. Hamamatsu S8664-55: (a) cross-sectioned view; (b) an electric field profile and (c) an avalanche gain profile [27].

3.6. QE Results and Discussion

A Monte Carlo simulation program for the determination of the APD QE, was developed at IFAE, Barcelona, to describe our experimental setup. The code integrated some important features that are required to take into account: X-ray absorption in the gas, primary electron ionization, electron transport following the transverse diffusion in the gas [31], electroluminescence production, photon propagation, optical transparency of the grids, solid angle effects, etc.

From the Monte Carlo simulation, we determine the number of photons arriving to the APD, N_{UV}, and with the result of the non-linear response factor, for 22.1 keV X-rays at a biasing voltage of 415 V, the final value of the Hamamatsu VUV-sensitive S8664-SPL quantum efficiency was obtained.

The result for the quantum efficiency of the APD is 69±15% for 172 nm photons using a ^{109}Cd source, it is well in agreement with the measurements from Hamamatsu which claims about 80% for 175 nm. This QE result makes these devices very attractive for

the readout of GPSCs filled with xenon. On the other hand, large non-linearities for direct X-ray detection were observed as function of the APD bias voltage and also depending on the energy of the x-ray source which makes these devices unsuitable for direct X-ray detection.

References

[1] J.A.M. Lopes *et al., A xenon gas proportional scintillation counter with a UV-sensitive large-area avalanche photodiode*, IEEE Trans. Nucl. Sci. 48 (2001) 312-319.

[2] L.C.C. Coelho, *et al., Xenon GPSC high-pressure operation with a large-area avalanche photodiode readout*, Nucl. Instrum. Meth. A 575 (2007) 444-448.

[3] T. Shutt, E. Aprile *et al.* (XENON Collaboration), *The XENON dark matter experiment*, Nucl. Phys. B—Proceedings Supplements 138 (2005) 156-159.

[4] V.N. Lebedenko *et al., Results from the first science run of the ZEPLIN-III dark matter search experiment,* Phys. Rev. D 80 (2009) 052010.

[5] R. Neilson *et al.* (for the EXO Collaboration), *EXO-200*, J. Phys. Conference Series 136 (2008) 042052.

[6] V. Alvarez *et al.* (NEXT Collaboration)*, NEXT-100 Technical Design Report (TDR)*, 2012 JINST 7 T06001.

[7] D. Sinclair (for the EXO Collaboration), *New concepts for a gaseous Xenon detector for double beta decay*, J. Phys. Conference Series 203 (2010) 012062.

[8] D. Nygren, *High-pressure xenon gas electroluminescent TPC for 0-ν ββ-decay search*, Nucl. Instrum. Meth. A 603 (2009) 337-348.

[9] A. Bolotnikov and B. Ramsey, *The spectroscopic properties of high-pressure xenon*, Nucl. Instrum. Meth. A 396 (1997) 360-370.

[10] L.M.P. Fernandes *et al., Primary and secondary scintillation measurements in a Xenon Gas Proportional Scintillation Counter*, 2010 JINST 5 P09006.

[11] L.M.P. Fernandes *et al., Characterization of large area avalanche photodiodes in X-ray and VUV-light detection*, 2007 JINST 2 P08005.

[12] T. Lux *et al., A Multi-APD readout for EL detectors*, J. Phys. Conference Series 309 (2011) 012008.

[13] L. Ludhova *et al.*, *Planar LAAPDs: temperature dependence, performance, and application in low-energy X-ray spectroscopy*, Nucl. Instrum. Meth. A 540 (2005) 169-179.

[14] M. Moszynski, M. Szawlowski, M. Kapusta and M. Balcerzyk*, Large area avalanche photodiodes in scintillation and X-rays detection*, Nucl. Instrum. Meth. A 485 (2002) 504-521.

[15] C.M.B. Monteiro, J.A.M. Lopes, J.F. C.A. Veloso and J.M.F. dos Santos, *Secondary scintillation yield in pure argon*, Phys. Lett. B 668 (2008) 167-170.

[16] P. Shagin *et al.*, *Avalanche Photodiode for liquid xenon scintillation: quantum efficiency and gain*, 2009 JINST 4 P01005.

[17] R. Chandrasekharan, M. Messina and A. Rubbia, *Detection of VUV light at high quantum efficiency with large area avalanche photodiodes (LAAPDs),* Nucl. Instrum. Meth. A 567 (2006) 45-47.

[18] R. Chandrasekharan, M. Messina and A. Rubbia, *Detection of noble gas scintillation light with large area avalanche photodiodes (LAAPDs)*, Nucl. Instrum. Meth. A 546 (2005) 426-437.

[19] T. Ikagawa *et al.*, *Performance of large-area avalanche photodiode for low-energy X-rays and γ-rays scintillation detection*, Nucl. Instrum. Meth. A 515 (2003) 671-679.

[20] T. Ikagawa *et al.*, *Study of large area Hamamatsu avalanche photodiode in a γ-ray scintillation detector*, Nucl. Instrum. Meth. A 538 (2005) 640-650.

[21] M. Sato *et al., Hole multiplication in a reverse-type avalanche photodiode*, Nucl. Sci. Symposium Conf. Rec., 2007. NSS '07. IEEE, vol. 2, 1486–1490.

[22] C.M.B. Monteiro *et al., Secondary scintillation yield in pure xenon*, 2007 JINST 2 P05001.

[23] T.H.V.T. Dias *et al., Full-energy absorption of X-ray energies near the Xe L-and K-photoionization thresholds in xenon gas detectors: Simulation and experimental results*, J. Appl. Phys. 82 (1997) 2742-2753.

[24] G. Knoll, *Radiation Detection and Measurements*, third ed., Wiley, 2001.

[25] M. Sato et al., *Reverse-type avalanche photodiode for scintillation detection and intrinsic energy resolution of BGO and GSO:Ce*, Nucl. Sci. Symposium Conf. Rec., 2007. NSS '07. IEEE, vol. 3, 2023–2032.

[26] M. Moszynski *et al.*, *Comparative study of avalanche photodiodes with different structures in scintillation detection*, IEEE Trans. Nucl. Sci. 48 (2001) 1205-1210.

[27] M. Sato *et al., Temperature effects in reverse-type avalanche photodiodes*, Nucl. Sci. Symposium Conf. Rec., 2007. NSS '07. IEEE, vol. 2, 1491–1493.

[28] J. Pansart, *Avalanche photodiodes for particle detection*, Nucl. Instrum. Meth. A 387 (1997) 186 -193.

[29] C. P. Allier *et al.*, *Comparative study of silicon detectors*, IEEE Trans. Nucl. Sci. 45 (1998) 576-580.

[30] M. Moszynski *et al.*, *Large Area Avalanche Photodiodes in X-rays and scintillation detection*, Nucl. Instrum. Meth. A 442 (2000) 230-237.

[31] S.F. Biagi, *Monte Carlo simulation of electron drift and diffusion in counting gases under the influence of electric and magnetic fields*, Nucl. Instrum. Meth. A 421 (1999) 234-240.

4.

ROOM TEMPERATURE OPERATION OF HAMAMATSU R8520-06SEL PMT FOR PRIMARY AND SECONDARY SCINTILLATION MEASUREMENTS

NEXT is a new experiment to search for neutrinoless double beta decay using a radiopure high-pressure gaseous xenon TPC. The detector requires excellent energy resolution, which can be achieved in a Xe TPC with electroluminescence readout. Hamamatsu R8520-06SEL photomultipliers are good candidates for the scintillation readout. The performance of this photomultiplier, used as VUV photosensor in a gas proportional scintillation counter, was investigated. Initial results for the detection of primary and secondary scintillation produced as a result of the interaction of 5.9 keV X-rays in gaseous xenon, at room temperature and at pressures up to 3 bar, are presented. An energy resolution of 8.0% was obtained for secondary scintillation produced by 5.9 keV X-rays. No significant variation of the primary scintillation was observed for different pressures (1, 2 and 3 bar) and for electric fields up to 0.8 V cm^{-1} $torr^{-1}$ in the drift region, demonstrating negligible recombination luminescence. A primary scintillation yield of 81 ± 7 photons was obtained for 6 keV X-rays, corresponding to a mean energy of 72 ± 6 eV to produce a primary scintillation photon in xenon.

4.1. Introduction

The proposed detector design for NEXT called SOFT (Separated Optimized Function TPC) approach, is based on a specific readout for both tracking and energy measurement [1]. Electroluminescence photons emitted towards the hemisphere of the anode can be used to recognize the specific track pattern of the two electrons emitted in the double beta decay. The technology does not require excellent energy resolution capabilities but does require robust pattern recognition and the capability to separate nearby hits. The photons emitted in the opposite direction can be detected with a series of PMTs mounted behind the cathode. Here, energy resolution and the identification of the start-of-event signal (t0) are the major needs, the latter being determined by the primary scintillation. Due to a uniform light distribution at the cathode, the whole area does not have to be covered. However the coverage has to guarantee a good identification of the t0 signal to ensure a full three-dimensional event reconstruction. Therefore the precise knowledge of the expected primary and secondary light densities is crucial to optimize the technology for these two tasks.

One of the PMTs considered for energy readout was from Hamamatsu, R8520-06SEL series [2] A similar type of PMT, R8520-06-AL, was developed for the double phase detector of the XENON collaboration and optimized for cryogenic operation [3,4]. This type of PMT, square shaped with a bialkali (Rb-Cs-Sb) photocathode and a quartz window, presents a quantum efficiency of about 30% at 175 nm. The PMTs are compact (1 in^2 area, 3.5 cm long), have 10 multiplication stages (dynodes) and reach a maximum gain of a few 10^6. The PMT investigated has a gain of 1.7×10^6 for a PMT bias of 800V, according to the manufacturer datasheet. The PMT, operating at room temperature, is able to detect a small number of UV photons.

The study of the performance of such PMT for the detection of primary and secondary scintillation produced in xenon, at room temperature, was an important part of the NEXT program. For this purpose, we built a xenon Gas Proportional Scintillation

Counter (GPSC) [5] equipped with a R8520-06SEL PMT as VUV photosensor. In such a detector, primary electrons released by ionization of the gas medium drift under an external electric field, below the Xe scintillation threshold, towards a region between two parallel meshes separated by a few mm. In this region, the so-called scintillation region, the electric field is such that the electron energy is kept below the Xe ionization threshold but high enough to excite Xe atoms. The de-excitation of Xe results in the isotropic emission of secondary scintillation photons of about 175 nm, which are detected by a photosensor. This multiplication process presents a linear dependence on the applied electric field [6,7] and smaller statistical fluctuations, resulting in improved energy resolutions when compared to charge avalanche processes [5].

In this chapter, we report the results obtained with such GPSC for 5.9 keV X-rays absorbed in the xenon. The results for both primary and secondary scintillation detection are presented and compared with other high performance GPSCs equipped with standard PMTs.

4.2. Experimental setup

The GPSC investigated is schematically depicted in figure 4.1. The R8520-06SEL PMT, used as VUV photosensor, was glued with low vapour pressure epoxy (TRA-CON 2116) to the pressure vessel on the anode plane. The GPSC has an aluminized Kapton window, a 3 cm thick drift region between the window and mesh G1, and a scintillation gap of 0.5 cm between mesh G1 and the anode plane (mesh G2). A radioactive source is positioned outside the chamber, on top of the detector window. The radiation window and mesh G1 are biased to negative high voltage, $-HV_0$ and $-HV_1$, while mesh G2, which covers the PMT window, and the detector body are connected to ground. A Macor piece is used to hold and provide electric insulation to the radiation window and mesh G1. Vacuum sealing of these parts was achieved by means of low vapour

pressure epoxy, while the lower and upper parts of the detector body are vacuum sealed by compression of an indium gasket.

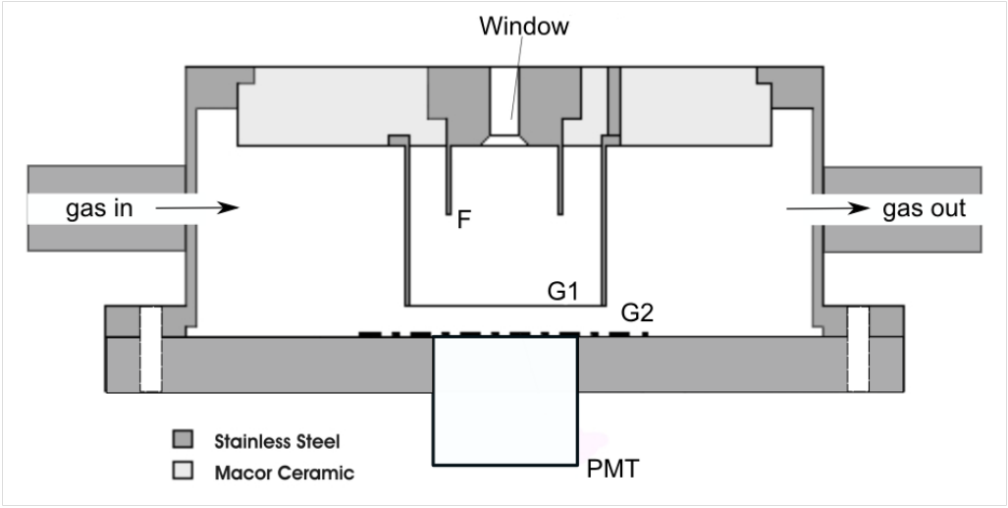

Figure 4.1. Schematic of the xenon GPSC with a R8520-06SEL PMT used as VUV photosensor.

The GPSC was pumped to vacuum pressures of about 10^{-6} mbar prior to xenon (99.999% pure) filling. The GPSC was operated at room temperature with the gas circulating by convection through ST707 SAES getters operated at 180ºC.

The study includes gain and energy resolution measurements for secondary scintillation as a function of the reduced electric fields (E/p) in the drift and scintillation regions, and also primary scintillation amplitude measurements as a function of the drift field. The measurements were made with both a digital oscilloscope and a multichannel analyser (MCA) and were performed at gas pressures of 1, 2 and 3 bar. PMT signals were fed through a low-noise charge sensitive preamplifier (Canberra Model 2005, with a charge conversion gain of 4.5 mV/pC) to a spectroscopy amplifier (Tennelec TC243, with coarse gain selectable between 5 and 2000 and shaping time constants between 0.5 and 12 μs) and were pulse-height analysed by a 1024-channel MCA (Nucleus PCA II).

4.3.Electroluminescence measurements

The response of the R8520-06SEL PMT to the electroluminescence produced within the xenon GPSC was investigated. The amplitude and energy resolution of the scintillation pulses produced in the xenon by the interaction of 5.9 keV X-rays from a ^{55}Fe radioactive source were determined for different electric fields in the drift and scintillation regions of the GPSC and for gas pressures up to 3 bar.

A thin film of chromium was placed between the radioactive source and the window to efficiently reduce the interaction of 6.4 keV X-rays (Mn K_β line) in the gas volume. A typical pulse-height distribution obtained for 5.9 keV X-rays (Mn K_α line) is shown in figure 4.2. The pulse-height distribution was obtained at atmospheric pressure for reduced electric fields in the GPSC drift and scintillation regions of 0.6 and 5.0 V cm^{-1} $torr^{-1}$, respectively, and for a PMT bias voltage of 660 V, which corresponds to a gain of about 3×10^5 according to the manufacturer datasheet. An energy resolution of 8.0% (FWHM) was obtained for the 5.9 keV X-ray peak, demonstrating a high performance, similar to that obtained with GPSCs instrumented with larger PMTs [8,9].

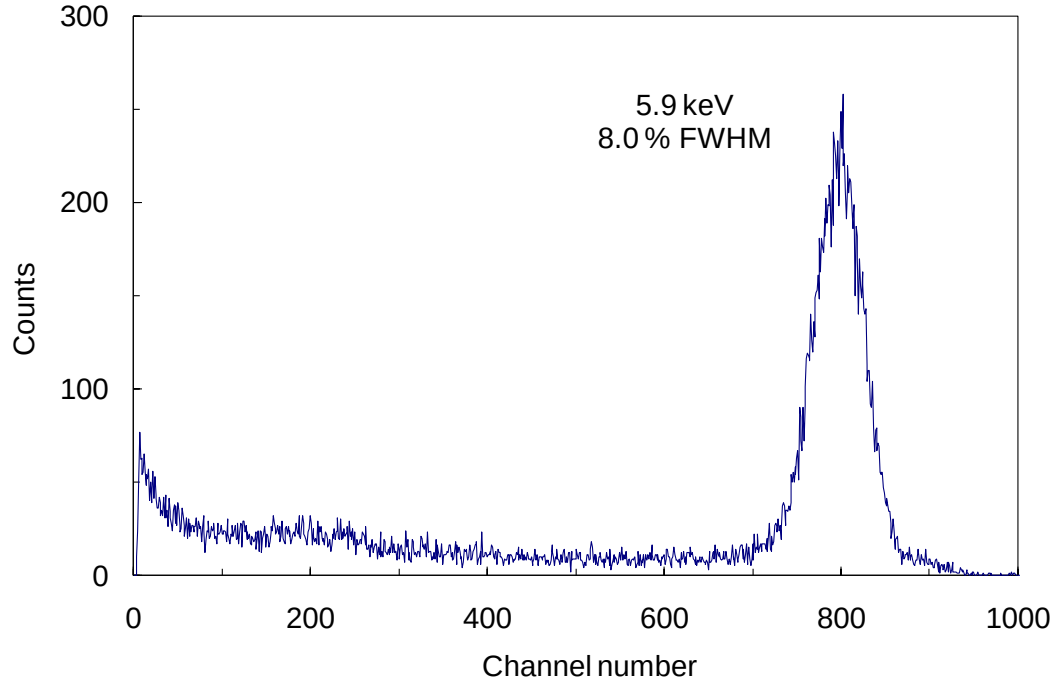

Figure 4.2. Energy spectrum of a ^{55}Fe radioactive source, showing the 5.9 keV X-ray peak. The PMT was biased to 660V. Optimal values of the electric field were applied to the drift and scintillation regions (0.6 and 5.0 V cm^{-1} torr^{-1}, respectively).

Since the statistical fluctuations associated to the production of VUV scintillation can be neglected, the energy resolution of a conventional GPSC is determined by the statistical fluctuations occurring in the primary ionization processes and in the photosensor. For a PMT photosensor, the energy resolution R (FWHM) is approximately [5]:

$$R = 2.355\sqrt{\frac{F}{N} + \frac{2}{N_e}} \tag{4.1}$$

where N is the average number of primary electrons produced per incident X-ray photon, F, the Fano factor, is the relative variance of N, and N_e is the average number of photoelectrons produced in the photosensor per X-ray photon absorbed in the drift region. Taking into account that $N = \frac{E_x}{w}$, where E_x is the X-ray photon energy and w the mean energy to produce a primary electron and defining the number of

photoelectrons produced per primary electron, $L = \frac{N_e}{N}$, the energy resolution can be given by:

$$R = 2.355\sqrt{\frac{w}{E_x}\left(F + \frac{2}{L}\right)} \quad (4.2)$$

L is a parameter that describes the photosensor performance. For the present PMT, *L= 19* assuming *F= 0.2* [5].

To obtain this excellent energy resolution, the reduced electric fields in the scintillation region (E/p-scint) and in the drift region (E/p-drift) had to be optimized. The dependence of the amplitude and energy resolution on the reduced electric field applied to the scintillation region is shown in figure 4.3(a), while the dependence on the drift electric field is shown in figure 4.3(b). Figure 4.3 clearly shows that E/p-scint has to be larger than 4 V cm^{-1} $torr^{-1}$ in order to get the best energy resolution, while E/p-drift has to be larger than 0.2 cm^{-1} $torr^{-1}$. In both cases, there are no significant variations of the energy resolution with the pressure. The signal amplitude increases with pressure. However, for the same E/p value, the amplitude is approximately proportional to the pressure due to the increase of the electric field. The ratio amplitude/pressure is then not significantly dependent on pressure, in accordance with former studies [7].

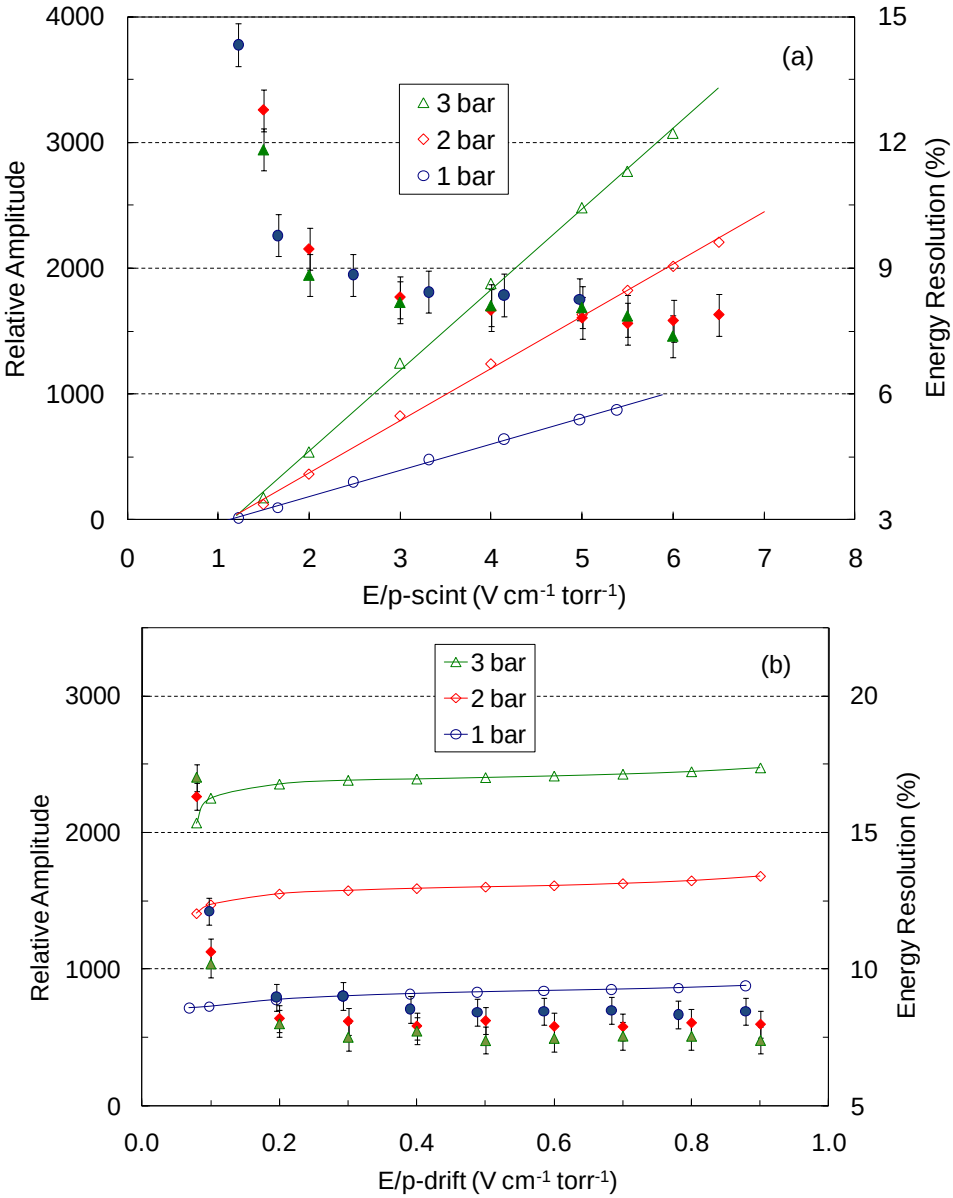

Figure 4.3. Relative amplitude (open symbols) and energy resolution (full symbols) for 5.9 keV X-rays absorbed in the GPSC as a function of: (a) E/p-scint, the electric field in the scintillation region; (b) E/p-drift, the electric field in the drift region. In (a), a fixed electric field of 0.5 V cm^{-1} $torr^{-1}$ was used in the drift region and the PMT was biased to 690 V. In (b), a scintillation electric field of 4 V cm^{-1} $torr^{-1}$ was used and the PMT was biased to 710 V. Measurements for different gas pressures (1, 2 and 3 bar) are shown.

4.4. Primary scintillation measurements

Primary scintillation is produced in the xenon during the formation of the primary electron cloud following the absorption of radiation and the subsequent

thermalisation of the photoelectron and other Auger electrons. The amplitude of primary scintillation pulses is very low, difficult to distinguish from noise. However, averaging out the noise to a very low level, using a digital oscilloscope, the primary scintillation pulse amplitude can be determined. The oscilloscope is triggered with the secondary scintillation pulse, which takes place few microseconds later, the transit time of the primary electrons through the drift region. The amplitude is measured from the average of 128 pulses. Figure 4.4 shows typical primary and secondary scintillation pulses, obtained in a Tektronix TDS 2022B oscilloscope. Electric fields of 0.2 and 2.0 V cm^{-1} $torr^{-1}$ were applied to the drift and scintillation regions, respectively. Where, the primary scintillation pulse is very well distinguished from the noise as a result of the averaging process.

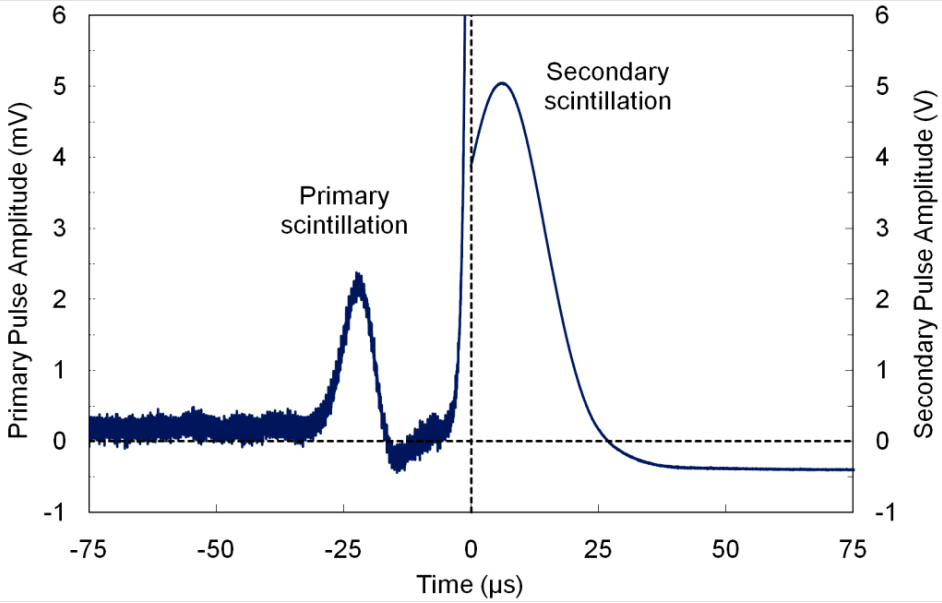

Figure 4.4. Typical primary and secondary scintillation pulses observed in the oscilloscope, after averaging 128 pulses, for 5.9 keV X-rays interacting in gaseous xenon. The oscilloscope was triggered by the secondary scintillation pulse.

The primary scintillation pulse amplitude was measured as a function of the drift electric field for pressures of 1, 2 and 3 bar, using a reduced electric field of 2.0 V cm^{-1} $torr^{-1}$ in the scintillation region (figure 4.5). Figure 4.5 shows that within the

experimental errors, the amplitude variation is not significant for electric fields between 0.2 and 0.8 V cm^{-1} $torr^{-1}$ and no significant variation with the pressure is observed. Below reduced electric fields of 0.2 V cm^{-1} $torr^{-1}$, both primary and secondary scintillation pulse amplitude drop significantly, an effect that has been also observed in Ref. [10]. The drop in the primary scintillation amplitude is not real, rather being an electronic artefact due to the trigger level as the secondary scintillation drops significantly with decreasing drift electric field. This behaviour is due to the loss of primary electrons through diffusion for the weaker drift fields. In fact, the amount of the primary scintillation, for low drift fields, could even increase with decreasing electric fields due to the presence of additional scintillation resulting from electron-ion recombination. For alpha particles interacting in xenon, the amount of recombination luminescence can reach a fraction above 50% of the total primary scintillation at zero drift electric field [11].

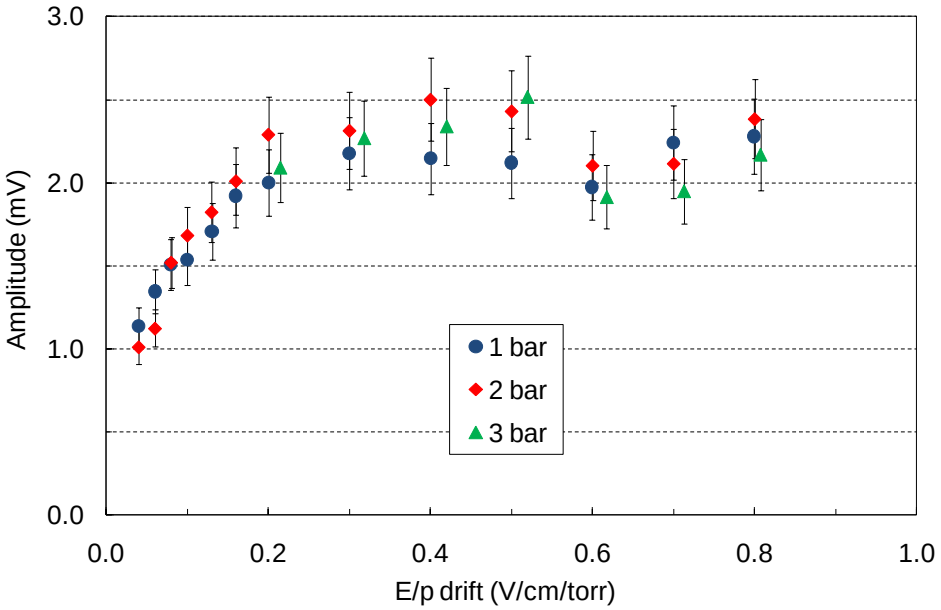

Figure 4.5. Primary scintillation signal amplitude, resulting from 5.9 keV X-ray interactions in xenon, as a function of the drift electric field, as measured directly in the oscilloscope.

To overcome the oscilloscope limitation and to look for experimental evidence of recombination luminescence, the electronic settings were optimized in order to detect primary scintillation pulses in the MCA. From the ratio between amplitudes of secondary and primary scintillation pulses, we can estimate the region where the pulse-height distribution of primary scintillation should be. In order to be more sensitive to the detection of the primary scintillation, the amplifier gain and the PMT voltage were increased to higher values.

In order to obtain the pulse-height distribution for the primary scintillation resulting from 5.9 keV X-rays absorbed in xenon, energy spectra with and without X-ray irradiation were recorded, with no electric fields in the GPSC drift and scintillation regions. This way, the pulse-height distribution for background due to residual visible light entering the chamber could be identified and subtracted (figure 4.6). The background rate decreases by improving the light shielding of the detector and by taking data during the night.

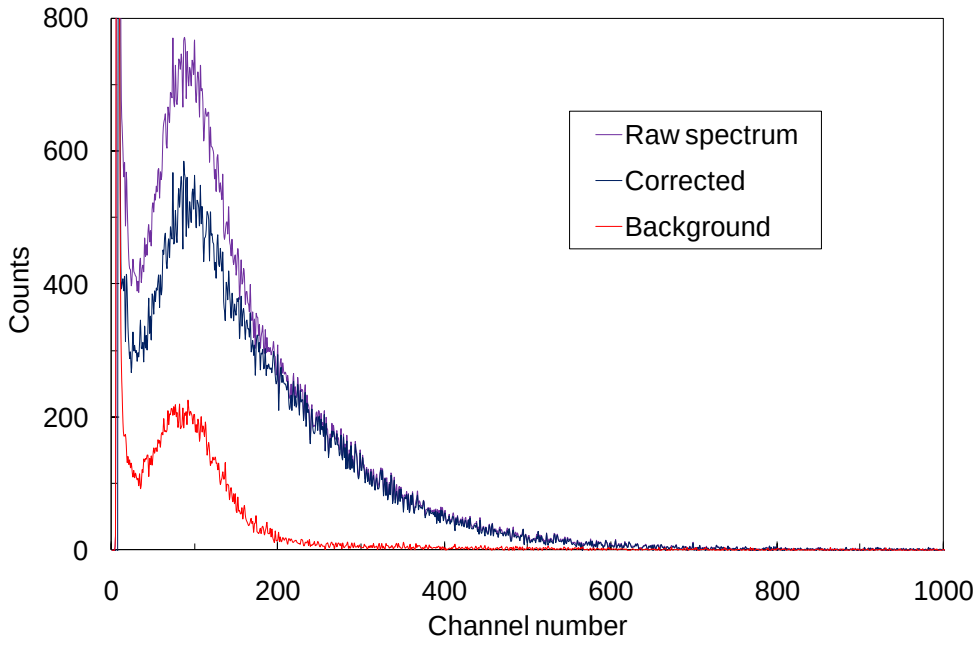

Figure 4.6. Pulse-height distribution obtained for 5.9 keV X-rays absorbed in the detector, with no electric fields applied to the drift and scintillation regions and for a PMT bias voltage of 730 V.

The pulse-height distribution obtained after background subtraction has other contributions than the one resulting from primary scintillation due to 5.9 keV X-rays absorbed in xenon. In fact, irradiating the detector with 22.1 and 25.0 keV X-rays from a ^{109}Cd radioactive source, a similar distribution is obtained in the low-energy region, while the pulse-height distribution due to primary scintillation resulting from X-ray absorption in xenon extends towards the higher energy region (figure 4.7). We believe that the peak obtained in the low energy region results from interactions in the presence of X-rays, such as luminescence and/or fluorescence of the detector materials as a result of X-ray and/or VUV photon interactions.

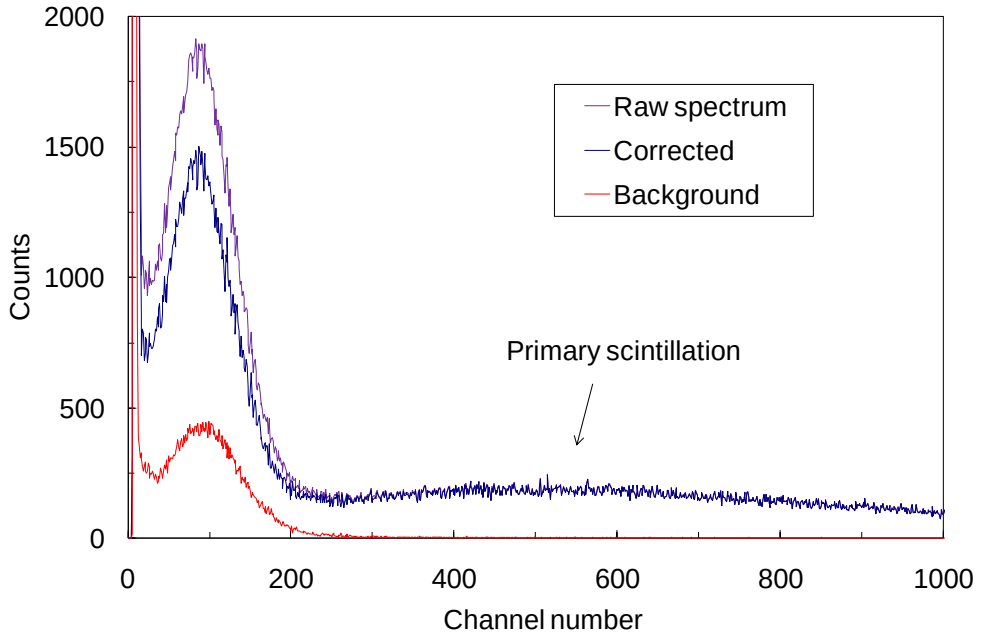

Figure 4.7. Pulse-height distribution obtained for the ^{109}Cd radioactive source, with no electric fields applied to the drift and scintillation regions of the detector and for a PMT bias voltage of 730 V.

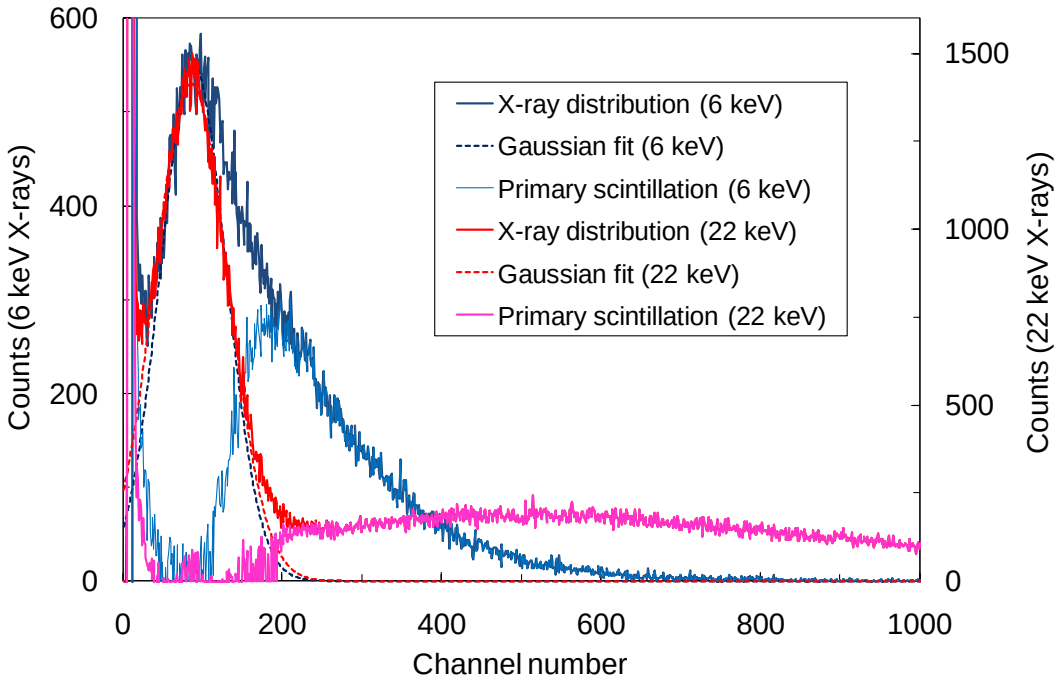

Figure 4.8. Estimated pulse height distributions of primary scintillation produced by 5.9 keV and 22.1 keV X-rays absorbed in the xenon, obtained by subtraction of a Gaussian curve fitted to the low-energy region of the X-ray distribution.

In order to extract the pulse-height distribution resulting from the primary scintillation produced by X-ray absorptions in xenon, the low-energy peak was subtracted from the pulse-height distributions, assuming a Gaussian shape (figure 4.8). Note that the fitted curves are very similar for 6 keV and 22 keV. The primary scintillation pulses produced by 5.9 keV X-rays are superimposed to the noise distribution, as was already shown by the oscilloscope measurements. The Landau shape of the primary scintillation distributions comes from solid angle effects. The amount of scintillation photons reaching the PMT depends on the depth where the primary scintillation is produced.

The variation of the primary scintillation distributions obtained for 5.9 keV X-rays with the drift electric field and with the xenon pressure was investigated (figure 4.9). For these measurements, no electric field was applied to the scintillation region. As seen, no dependence was found with the drift electric field and with pressure.

These results demonstrate promising operation characteristics of large volume xenon TPCs. No evidence of significant recombination at low drift electric fields and high pressures was found.

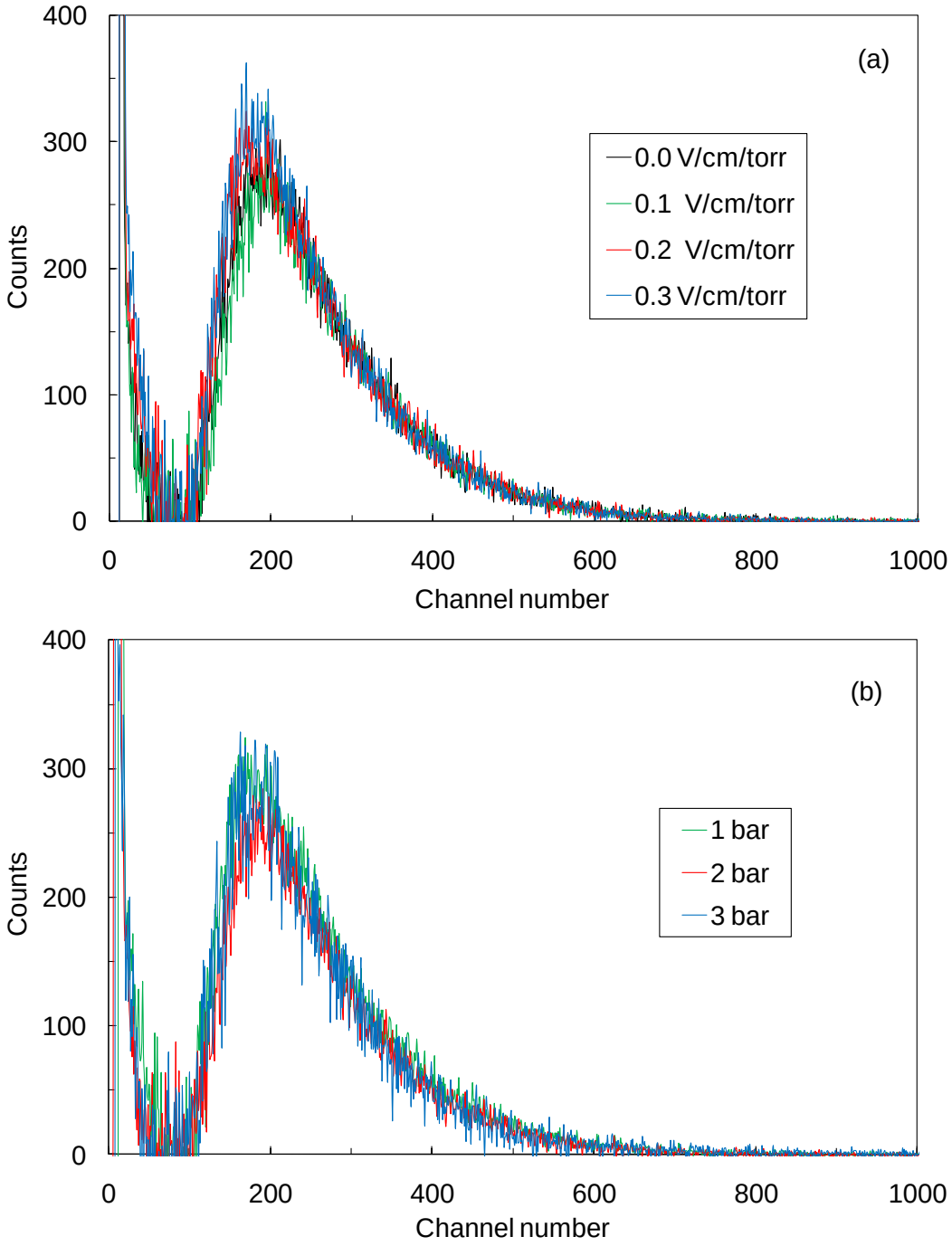

Figure 4.9. Estimated primary scintillation distributions for 5.9 keV X-rays absorbed in the xenon: (a) for different drift electric fields; (b) for different gas pressures.

4.5. Primary scintillation yield

The ratio between primary and secondary scintillation pulse amplitudes can be used to determine the absolute number of primary scintillation photons produced upon X-ray absorption, enabling the calculation of the average energy required to produce a primary scintillation photon (W_s). The pulse amplitudes for primary and secondary scintillation are proportional to the average numbers of primary and secondary scintillation photons reaching the PMT.

The number of secondary scintillation photons detected by the PMT is given by:

$$N_s = N_e\, T\, Y \frac{1}{4\pi} \int_D^{D+d} \Omega(x)\, dx \tag{4.3}$$

where N_e is the average number of primary electrons produced per X-ray absorbed, T is the grid optical transmission, Y is the secondary scintillation yield per primary electron per cm, $\Omega(x)$ is the solid angle subtended by the PMT window at each scintillation point x measured from the detector window, D and d are the thicknesses of the drift and scintillation regions, respectively.

Assuming a PMT photocathode with a circular shape, the solid angle $\Omega(x)$ along the drift and scintillation regions is given by [10]:

$$\Omega(x) = 2\pi \frac{1 - (D + d - x)}{\sqrt{(D + d - x)^2 + R^2}} \tag{4.4}$$

where R is the radius of the PMT photocathode.

As the primary scintillation has to cross two grids, the number of primary scintillation photons reaching the PMT is given by:

$$N_p = N_0\, T^2 \frac{\overline{\Omega}}{4\pi} \tag{4.5}$$

N_0 is the total number of primary scintillation photons produced per X-ray absorption, here called primary scintillation yield, and $\overline{\Omega}$ is the average solid angle for primary scintillation. This average solid angle has to be weighted by the X-ray absorption rate $g(x)$, taken along the drift region [10]. Function $g(x)$ is related to the X-ray absorption length, λ, through:

$$g(x) = (\frac{1}{\lambda}) e^{-\frac{x}{\lambda}} \tag{4.6}$$

The average solid angle for primary scintillation is then given by:

$$\overline{\Omega} = \frac{\int_0^D g(x)\ \Omega(x) dx}{\int_0^D g(x) dx} \tag{4.7}$$

From Eq. (4.3) and (4.5), we obtain:

$$\frac{N_s}{N_p} = \frac{N_e\ Y \int_D^{D+d} \Omega(x)\ dx}{N_0\ T\ \overline{\Omega}} \tag{4.8}$$

This ratio is then equal to ratio between the pulse amplitudes for secondary and primary scintillation. N_0 can be determined from Eq. (4.8) as all other parameters in the second term can be calculated.

The average energy required to produce a primary scintillation photon can be then estimated as $W_s = E_x/N_0$, E_x is the energy of the incident X-ray. For 5.9 keV X-rays, the number of primary electrons is $N_e = E_x/w = 263$ assuming a w-value of 22.4 eV for xenon [12]. The secondary scintillation yield Y is related to the electric field E in the scintillation region and can be obtained from the equation from Ref. [6]:

$$\frac{Y}{p} = 140\frac{E}{p} - 116 \tag{4.9}$$

where Y/p is expressed in photons per electron per cm per bar and E/p in kV per cm per bar.

For E/p = 1.5 kV cm^{-1} bar^{-1} (or 2.0 V cm^{-1} torr^{-1}), Y/p = 94 photons electron^{-1} cm^{-1} bar^{-1}.

The other parameters of Eq. (4.8) are T = 0.84, D = 3 cm, d = 0.5 cm. The solid angle was calculated numerically assuming that the PMT has a circular photocathode with the same area (R = 1.24 cm). For 5.9 keV X-rays in 1 bar of xenon, the absorption length is 0.26 cm [13]. The solid angle parameters obtained for 1 bar are:

$$\int_{D}^{D+d} \Omega(x)\, dx = 2.533\ sr\ cm \tag{4.10}$$

$$\overline{\Omega} = 0.424\ sr \tag{4.11}$$

The ratio between secondary and primary scintillation pulse amplitudes is shown in Figure 4.10. These results were obtained from oscilloscope measurements of the primary and secondary scintillation pulse amplitudes, like in figure 4.5. In order to observe secondary scintillation pulses, an electric field of 2.0 V cm^{-1} torr^{-1} was used in the scintillation region. Within the experimental errors, the ratio is approximately constant for drift electric fields between 0.2 and 0.8 V cm^{-1} torr^{-1}. An average value in this interval was used for calculations.

Table I shows several parameters used in Eq. (4.8) to determine N_0 and W_s for different gas pressures. As expected, there is no significant variation with the pressure. The three values obtained are very compatible taking into account the respective errors. Averaging the results for the three different series, for gas pressures of 1, 2 and 3 bar, a final value N_0 = 81 ± 7 photons is obtained. And the mean energy required to produce a primary scintillation photon is W_s = 72 ± 6 eV. This value is lower than previous measurement, 111 ± 16 eV [10] but it is, however, similar to the one measured in [14], 76 ± 12 eV, obtained for 60 keV γ-rays at 20 bar.

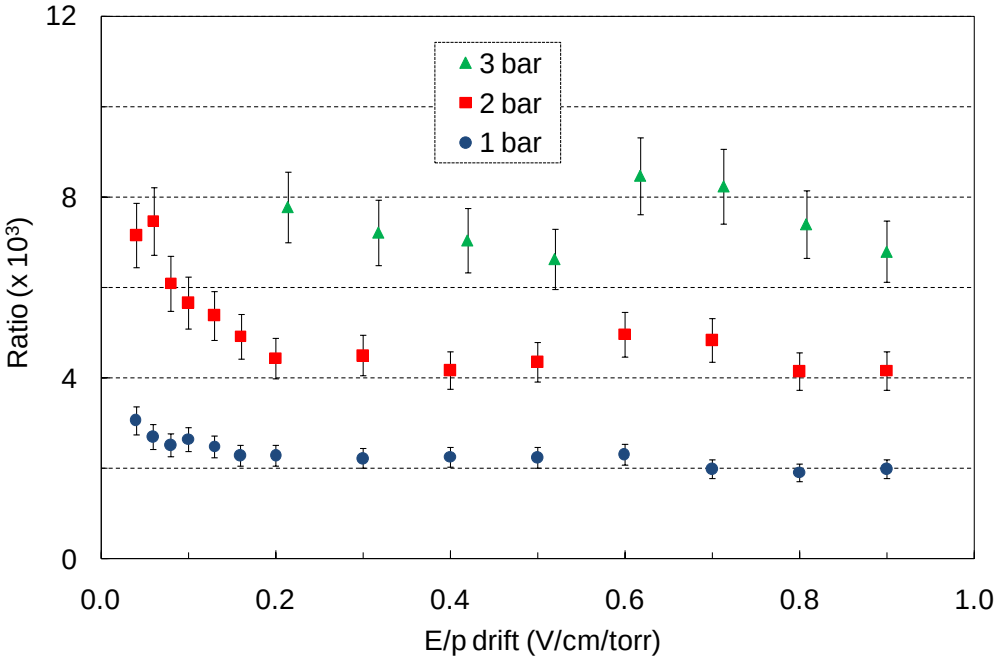

Figure 4.10. Ratio between secondary and primary scintillation pulse amplitude as a function of the drift electric field, obtained from oscilloscope amplitude measurements, for 5.9 keV X-rays absorbed in xenon.

In the present conditions, about 2 primary scintillation photons were detected by the PMT per X-ray of 5.9 keV absorbed in the xenon. For NEXT, double beta decay events have 2458 keV energy. The total number of primary scintillation photons produced in xenon will be ~ $2458\times10^3/72 = 3.4\times10^4$. As the PMT dimensions are much smaller than the distance to the interaction point, the solid angle subtended by the PMT is approximately given by $\Omega = (A/d)^2$, where A is the PMT active area and d is the distance to the interaction point. Assuming d = 50 cm, the fractional solid angle is then $\Omega/4\pi = (2.2/50)^2/4\pi = 1.54\times10^{-4}$. This means that about 5 photons should reach the PMT. However, a large amount of PMTs will be used and the sum of all PMT signals will make the signal large enough to be detected above the noise level as the sum of the noise will reduce the final noise level. In addition, the visible light and X-ray background observed in this work will not be present in the NEXT detector.

The number of photoelectrons produced in the PMT per primary electron crossing the scintillation region (L) can be estimated from Eq.(4.3) as L=Ns*QE/Ne, being QE the quantum efficiency of the PMT (30% [2]). A value of L= 20 is obtained for E/p = 5 V $cm^{-1}torr^{-1}$ in the scintillation region, which is in good agreement with that obtained from the energy resolution values, Eq.(4.2).

Pressure (bar)	N_s/N_p (×10^3) Fig. 4.10	Y (photons/e^-/cm) Ref. [6]	λ (cm)	$\overline{\Omega}$	N_0 (photons)	W_s (eV)
1	2.2 ± 0.2	94 (±10%)	0.261	0.424	80 ± 11	74 ± 10
2	4.5 ± 0.4	188 (±10%)	0.131	0.389	85 ± 11	69 ± 9
3	7.5 ± 0.9	282 (±10%)	0.087	0.379	79± 12	75± 12

Table 4.1. Parameters of eq. (4.8) used to determine the primary scintillation yield in xenon for different gas pressures

4.6. Conclusions

The performance of a Hamamatsu R8520-06SEL photomultiplier, used as VUV photosensor in a xenon GPSC, has been investigated, demonstrating that this PMT is a good candidate for the scintillation readout in the TPC to be used in the NEXT experiment.

The PMT high performance for secondary scintillation detection was demonstrated. An energy resolution of 8.0% (FWHM) was obtained for 5.9 keV X-rays absorbed in the xenon, similar to GPSCs instrumented with larger PMTs, demonstrating the very low statistical variance of electroluminescent gain.

Primary scintillation measurements have been carried out. The pulse-height distribution obtained in the MCA, for different electric field values in the drift region and for different xenon pressures, didn't show significant variations with the drift electric field and with pressure, demonstrating negligible recombination luminescence. Amplitude measurements of the primary scintillation produced by 5.9 keV X-rays were

possible using an averaging process in the oscilloscope and triggering at the corresponding secondary scintillation pulse. These oscilloscope measurements allowed a determination of the primary scintillation yield in xenon gas. An average of 81 ± 7 primary scintillation photons produced by 6 keV X-rays absorbed in the xenon was obtained. The average energy required to produce a primary scintillation photon in xenon was deduced, resulting W_s = 72 ± 6 eV. This value is lower than the previous measurement of W_s, 111 ± 16 eV [10], but is however similar to the one measured for 60 keV γ-rays at 20 bar, 76 ± 12 eV [14]. Since the production of primary scintillation results from collisional processes of the photoelectrons and other Auger and shake-of electrons with the gas atoms, it is expected that Ws does not vary significantly with the gas pressure.

References

[1] D. Nygren, *Optimal detectors for WIMP and 0–v ββ searches: Identical high-pressure xenon gas TPCs?,* Nucl. Instr. Meth. A 581 (2007) 632-642.

[2] Hamamatsu Photonics Inc.; http://www.hamamatsu.com

[3] J. Angle *et al.* (XENON collaboration), *First results from the XENON10 dark matter experiment at the Gran Sasso National Laboratory*, Phys. Rev. Lett. 100 (2008) 021303.

[4] J. Angle *et al.* (XENON collaboration), *Constraints on inelastic dark matter from XENON10*, Phys. Rev. D 80 (2009) 115005.

[5] J.M.F. dos Santos *et al., Development of portable gas proportional scintillation counters for X-ray spectrometry*, X-Ray Spectrom. 30 (2001) 373-381.

[6] C.M.B. Monteiro *et al., Secondary Scintillation Yield in Pure Xenon*, 2007 JINST 2 P05001.

[7] E.D.C. Freitas *et al., Secondary scintillation yield in high-pressure xenon gas for neutrinoless double beta decay (0νββ) search*, Phys. Lett. B 684 (2010) 205-210.

[8] J.M.F. dos Santos, A.C.S.S. Bento and C.A.N. Conde, *A simple, inexpensive gas proportional scintillation counter for X-ray fluorescence analysis*, X-Ray Spectrom. 22 (1993) 328-331.

[9] A. Peacock *et al., Performance characteristics of a gas scintillation spectrometer for X-ray astronomy*, Nucl. Instrum. Meth. 169 (1980) 613-625.

[10] S.J.C. do Carmo, F.I.G.M. Borges, F.P. Santos, T.H.V.T. Dias and C.A.N. Conde, *Absolute primary scintillation yield of gaseous xenon under low drift electric fields for 5.9 keV X-rays*, 2008 JINST 3 P07004.

[11] M. Mimura *et al., Intensity and time profile of recombination luminescence produced by an α-particle in dense Xenon gas*, Nucl. Instrum. Meth. A 613 (2010) 106-111.

[12] T.H.V.T. Dias *et al., Full-energy absorption of X-ray energies near the Xe L-and K-photoionization thresholds in xenon gas detectors: Simulation and experimental results*, J. Appl. Phys. 82 (1997) 2742-2753.

[13] http://physics.nist.gov/PhysRefData/XrayMassCoef/ElemTab/z54.html

[14] A. Parsons *et al., High pressure gas scintillation drift chambers with wave shifter fiber readout,* IEEE Trans. Nucl. Sci. 36 (1989) 931-935.

5.

MICROMEGA OPERATION AT HIGH PRESSURE XENON FOR CHARGE AND ELECTROLUMINESCENCE AMPLIFICATION

In this chapter we investigated the characteristics of a Micromegas operating in pure xenon at the pressure range of 1 to 10 bar. The maximum charge gain achieved in each pressure is for xenon pressures up to 5 bar, approximately constant, around 4 x 10^2, and decreasing slowly above this pressure down to values somewhat above 10^2 at 10 bar. The lowest energy resolution obtained for x-rays of 22.1 keV exhibits a steady increase with pressure, from 12% at 1bar to about 32% at 10 bar. The effective scintillation yield, defined as the number of photons exiting through the MM mesh holes per primary electron produced in the conversion region was calculated. This yield is about 2x10^2 photons per primary electron at 1 bar, increasing to about 6x10^2 at 5 bar and, then, decreasing again to 2x10^2 at 10 bar. Comparing to the charge readout, the readout of this scintillation by a suitable photosensor will result in higher gains but with increased statistical fluctuations.

5.1. Introduction

The detector proposed design for NEXT, called SOFT approach, is based on a specific readout for both tracking and energy measurement [1]. Primary ionization signals are amplified by means of electroluminescence amplification in a confined region of the TPC, the scintillation region. Electroluminescence photons emitted towards the hemisphere of the anode can be used for tracking, while photons emitted in the opposite direction can be detected with a series of PMTs mounted behind the cathode, for energy measurement and t_0 determination (by means of primary scintillation readout).

While for the energy and t_0 readout plane PMTs are the best choice, for the tracking plane different options can be considered. MPPCs (multi-pixel photo-counters) [2], APDs (avalanche photodiodes) [3] and THGEM [4] are options under study for the electroluminescence readout. In addition, the use of Micromegas [5] for the tracking plane is also under consideration [6]. In this case, the primary electrons will be guided to the Micromegas (MM) after crossing the scintillation region, undergoing charge avalanche in the MM gap for signal amplification. On the other hand, if the energy resolution obtained by the Micromegas operating in xenon can be as good as that obtained in other gas mixtures [6,7], i.e. close to the intrinsic energy resolution, then the MM can also present an alternative to the energy readout plane, merging in a single plane the tracking and energy readout and resulting in a significant reduction in detector complexity and cost.

However, the performance of micropatterned electron multipliers operating at high pressures is limited. For GEMs, THGEMs and MHSPs operating in heavy noble gases, Xe and Kr, the maximum achievable gain decreases with pressure, together with an increase of the statistical fluctuations [8-11]. This is due to the fact that the maximum applied voltage does not increase as fast as the pressure and, consequently, the maximum achievable reduced electric field decreases with pressure. Such studies in xenon have not yet been carried out for MM. In addition, the scintillation produced in

the electron avalanches in the MM gap will be superimposed with that produced in the scintillation region, due to the large dimensions of the primary electron cloud. This may jeopardize the detector energy resolution if its relative amount is significant.

We investigated the performance of Micromegas (MM) operating in pure xenon at high pressures. The charge gain, the scintillation yield (i.e. the number of photons leaving the MM per primary electron produced in the conversion gap) and the associate statistical fluctuations are studied as a function of the MM biasing voltage for different pressures, in the range of 1 to 10 bar. The scintillation produced in the MM is readout by means of a large area avalanche photodiode (LAAPD), placed in front of it.

5.2. Experimental setup

The MM and the LAAPD were accommodated in a stainless steel chamber. The schematic layout of the MM and the LAAPD is shown in figure 5.1. The chamber has a cylindrical shape with 100 mm in diameter and 49.5 mm in height. The MM has an active area of ~ 40 mm in diameter, a gap of 50 μm and its mesh has 25 μm diameter holes. The LAAPD is an API Deep UV model [12], with an active area 16 mm and its encapsulation is perforated with holes in order to have the same pressure in both sides of the Si wafer. The MM backplane was fixed to the chamber scintillation window. A stainless steel mesh (80 μm diameter wires with 900 μm spacing) was placed in between the MM and the LAAPD in order to establish an uniform electric field in the conversion/drift region. The stainless steel mesh and the MM mesh were kept at negative voltages while the MM induction plane was kept at zero volts. The LAAPD enclosure and the chamber body were grounded. The conversion/drift region gap was 7.0 mm thick and the region between the LAAPD enclosure and the stainless steel

mesh was chosen to be thick, 7.8 mm thick, in order to keep the reduced electric field in this region below the xenon scintillation threshold (~ 0.8 kV $cm^{-1}bar^{-1}$ [13]).

The Micromegas [5] is a double stage parallel plate avalanche counter with a narrow multiplication gap (25–150 μm, 50–70 kV/cm), located between a thin metal grid (micromesh) and the readout electrode (strips/pads of conductor printed on an insulator board). The distance homogeneity between the anode and the grid mesh is preserved by using spacers from insulating material. The small amplification gap is a key element in Micromegas operation, giving rise to excellent spatial and time resolution: 12 μm spatial (limited by the pitch of micromesh) and 300 ps time resolution are achieved with single electron signal.

For our studies we have used a Micromegas (figure 5.1(b)) fabricated by a novel technique, called “Microbulk”, based on kapton thin-foil etching technology [14]. A thin photoresistive film is laminated on top of the kapton foil and it is insolated by UV light to produce the required mask. The copper is then removed by a standard lithographic process, the non-insulated places producing a pattern of a thin mesh. The polyimide is then etched and partially removed in order to create tiny pillars in the shadow part of the mesh below the copper mesh. The result is an “all-in-one” detector with improved characteristics such as uniformity, stability and material radiopurity. Thus, the achieved maximum gain and energy resolution are further improved compared to the traditional Micromegas, while it is possible to construct detectors with multiplication gaps of 25 or even 12.5 μm which are better performing in high gas pressures.

A 2-mm collimated x-ray beam originating from a ^{109}Cd source (22.1 and 25.0 keV Ag K_α and K_β fluorescence x-rays, respectively), irradiate the conversion/drift region through the chamber radiation window and through the MM. The primary electron clouds induced by the X-rays in the conversion gap were focused under a drift field E_{drift} into the MM holes and multiplied in the gap, being the charge signal collected in the MM induction electrode. A great number of VUV photons (~ 172nm) are produced along the charge avalanche as a result of the gas de-excitation processes. Part of these

photons leaves the MM trough the mesh holes and reaches the LAAPD active area and the corresponding electric signal is amplified in the photodiode. Therefore, we have two independent readout channels: one for the MM induction plane, which we call Charge channel, and the other for the LAAPD anode, which we call scintillation channel.

a)

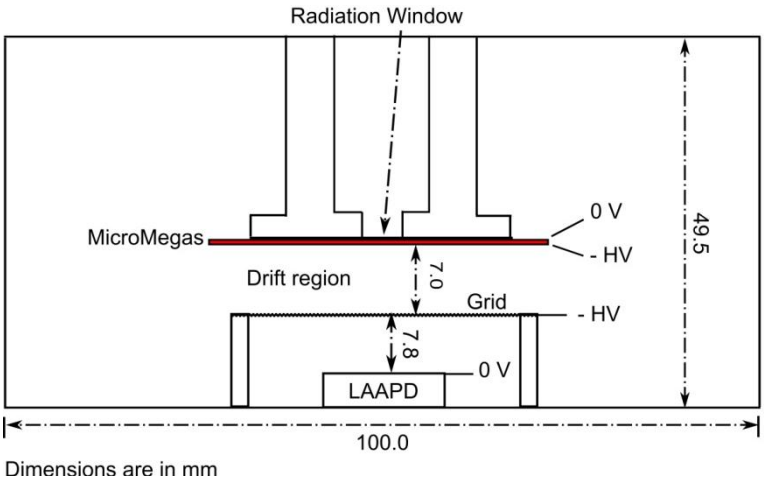

b)

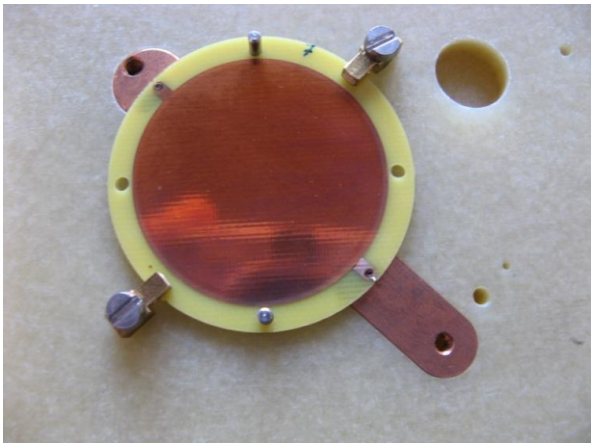

Figure 5.1. Schematic layout of the MicroMegas detector used in this work (a) and Micromega with 3.5 cm diameter (b).

Through this experimental work, the LAAPD biasing was set to a safe value of 1650 V, corresponding to a charge amplification gain of about 30 [15,16]. High performance is reached, even for such small photosensor gains, as a result of both high scintillation amplification and high conversion-efficiency of xenon scintillation into charge in the LAAPD [17]. The LAAPD was used to detect simultaneously the secondary scintillation

produced in the MM and the incident X-rays, which are used as a reference for determining the absolute number of charge carriers produced by the scintillation detected in the LAAPD and, hence, the number of VUV-photons hitting the LAAPD, given its quantum efficiency.

The chamber was pumped down to ~10^{-5} mbar by a turbo-molecular pump and filled with Xenon at pressures from 1 to 10 bar. The pressure was kept constant during each set of measurements. The xenon is continuously purified, circulating by convection through non-evaporable getters (SAES St 707), which are kept to a stable temperature, ~130ºC.

The charge signals of both MM induction plane and LAAPD were fed to charge-sensitive preamplifiers, being further amplified and shaped with linear amplifiers and pulse-height analyzed with multi-channel analyzers. For peak amplitude and energy resolution measurements, pulse-height distributions were fitted to a Gaussian function superimposed on a linear background, being the centroid and the full width half maximum (FWHM) determined. Both electronic chains were calibrated by means of a precision pulse generator and a known capacitance coupled to the preamplifier input.

5.3. Experimental results

5.3.1. Preliminary study at 1 bar

The reduced electric field in the drift region defines the primary electron cloud diffusion and the ratio of drift-to-gap fields defines the electron transfer efficiency through the mesh. Therefore, we started to study the pulse amplitude and energy resolution dependence on the drift voltage and on the MM biasing voltage, for the charge and the scintillation pulses for xenon at 1 bar. In figure 5.2 we depict the amplitude and energy resolution as a function of the voltage applied to the drift region, for the MM and LAAPD pulses and for a constant MM bias voltage of 340V. Figure 5.2 shows that both relative amplitudes remain constant up to a certain drift

voltage, decreasing with the increase of ΔV drift above this value. The MM should be operated in this so called plateau in order to achieve the best performance conditions.

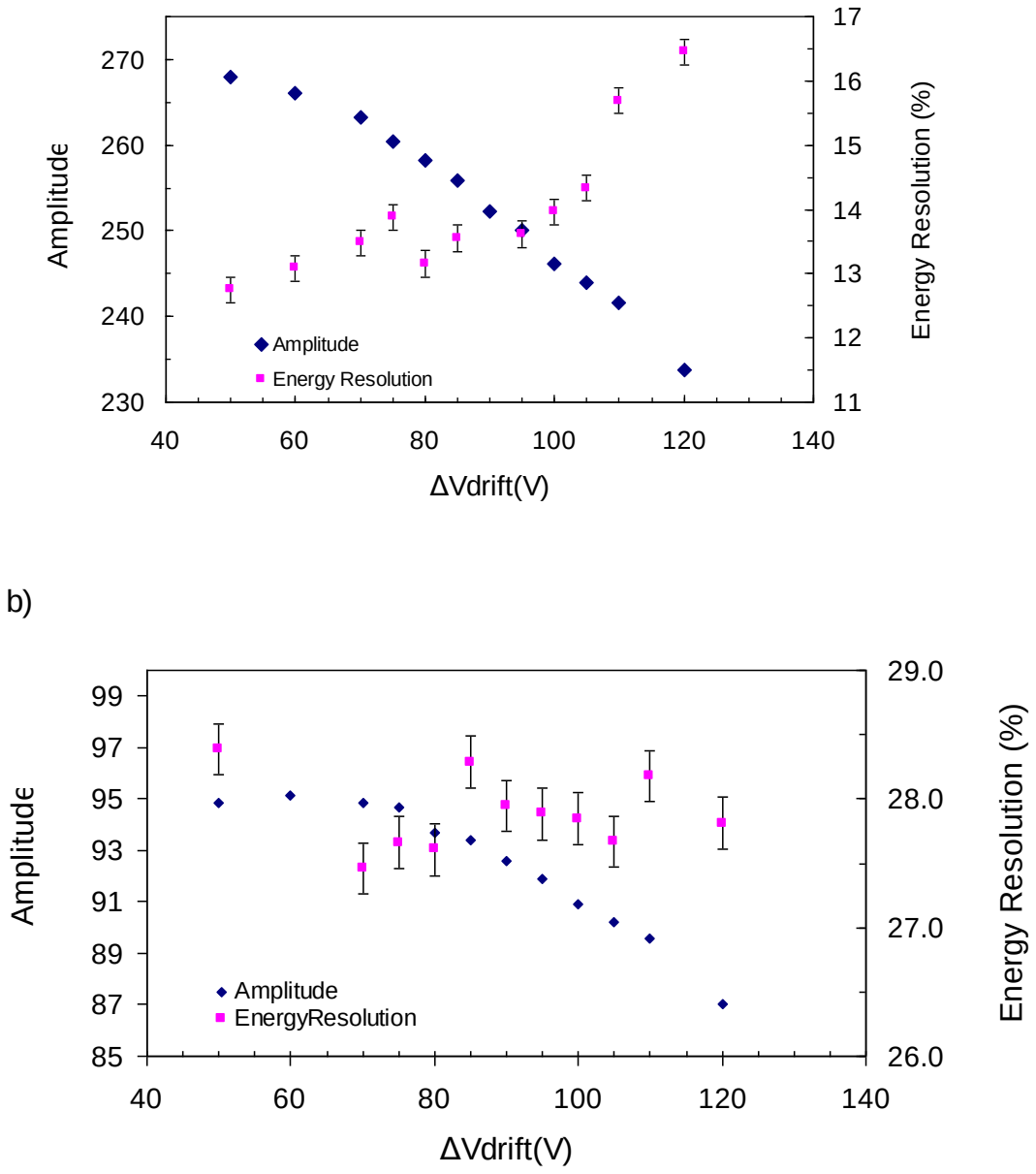

Figure 5.2. Relative amplitude and energy resolution for 22.1 keV X-rays absorbed in the GPSC as a function of the voltage applied in the drift region, for a constant V_{MM} of 340V with the LAAPD biased to 1650 V: (a) MM charge readout (b) LAAPD scintillation readout.

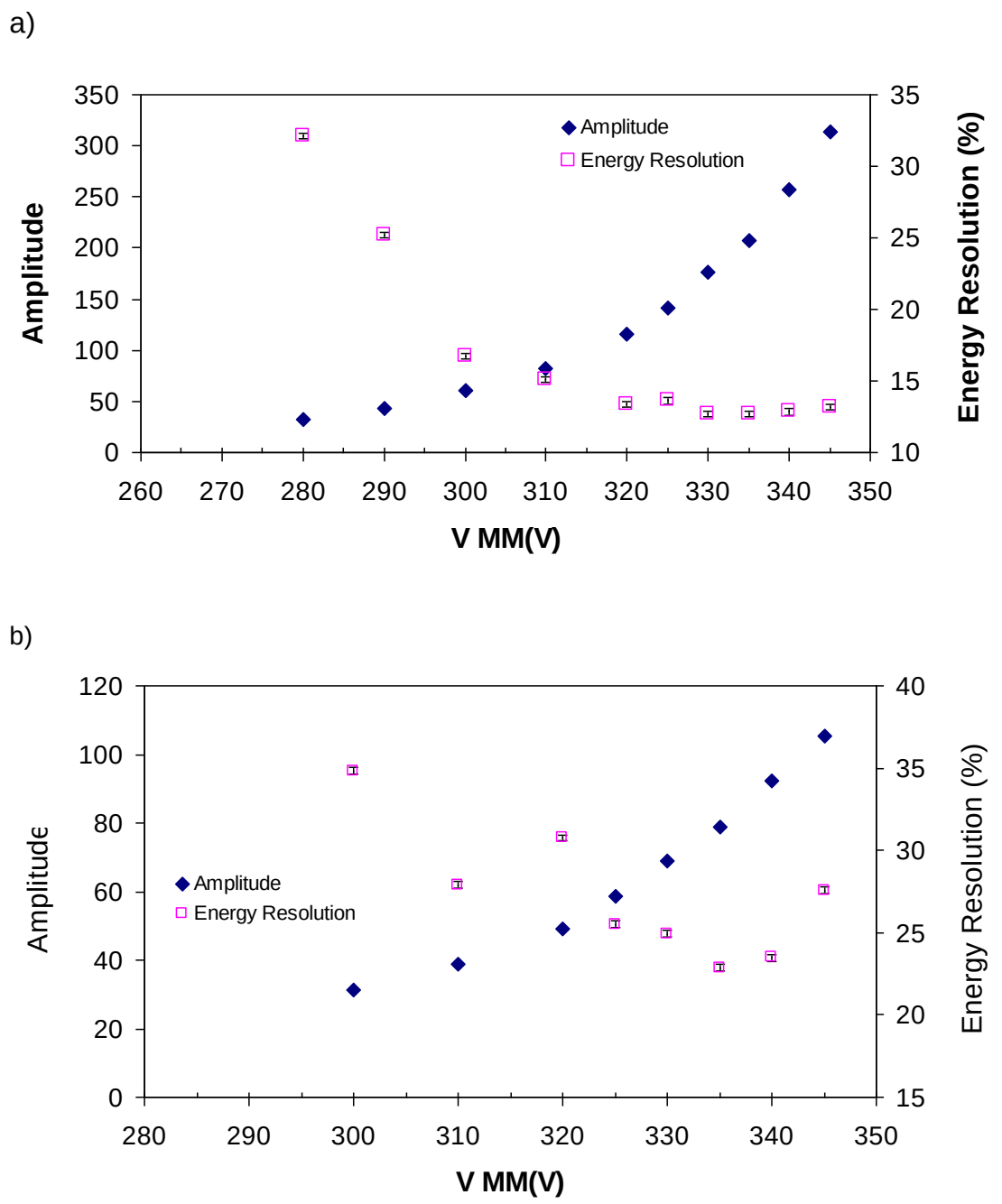

Figure 5.3. Relative amplitude and energy resolution for 22.1 keV X-rays absorbed in the GPSC as a function of the voltage applied in the Micromega, for a constant drift voltage applied of 80V with the LAAPD biased to 1650 V: (a) MM charge readout (b) LAAPD scintillation readout.

Figure 5.3 depicts the dependence of the amplitude and energy resolution readouts for the MM (a) and LAAPD (b), on the applied MM voltage bias while keeping ΔV drift,

the voltage applied in the drift region, as well as the the LAAPD biasing voltage constant. Figure 5.3 shows that both relative amplitudes increases with the increase of the biasing MM voltage, but in order to get the best energy resolution in the LAAPD the MM biasing voltage should not be higher than 340V.

5.3.2. Studies for the pressure range 2-10 bar

Typical pulse-height distributions obtained for the ^{109}Cd x-rays are presented in figure 5.4, for filling pressures of 2, 6 and 10 bar and for the charge and the scintillation readout channels.

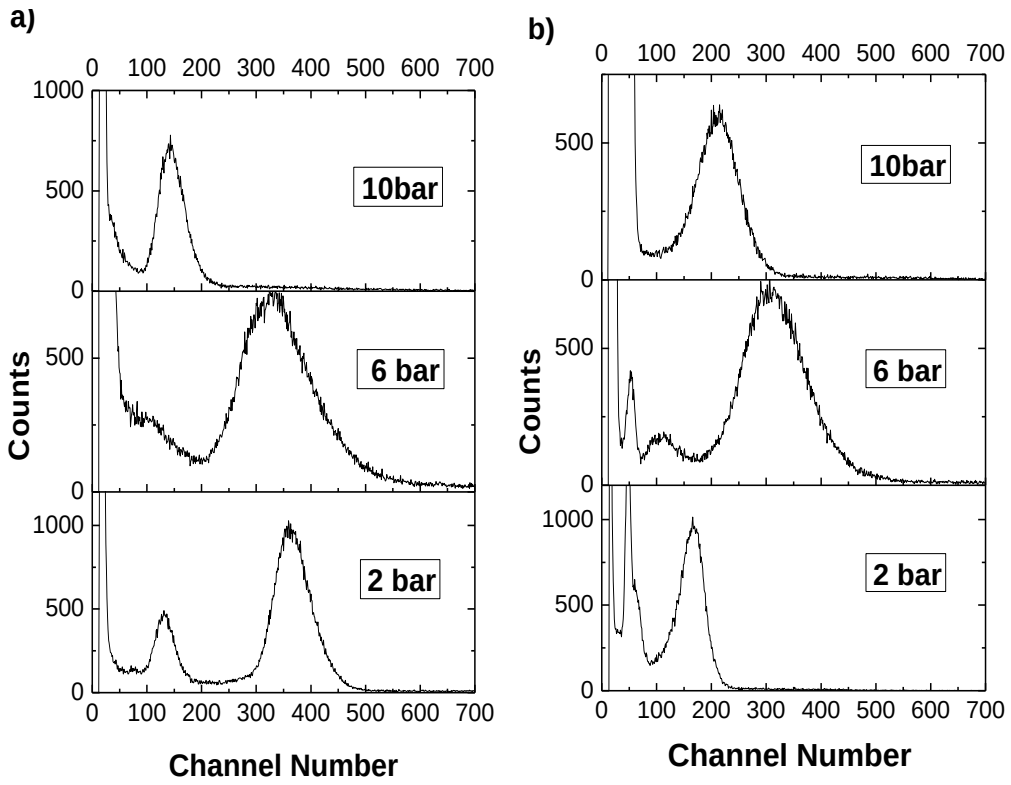

Figure 5.4. Typical pulse-height distributions obtained for the ^{109}Cd x-ray source; a) for the charge readout channel and b) for the scintillation readout channel.

The pulse-height distributions exhibit the peak resulting from the Ag K-fluorescence emitted by the ^{109}Cd x-ray radioactive source, the peak resulting from the Cu K-fluorescence resulting from the interactions of the x-rays in the MM copper electrodes, and the electronic noise tail in the low energy range. The energy resolution is not enough to separate the Ag K_α and K_β lines. A good separation has been observed [18] in a different set-up using an Argon mixture at atmospheric pressure. We do not know whether this degradation is due to the different gas or pressure or the quality of the readout element.

For the scintillation readout channel an additional peak resulting from the Ag K-fluorescence direct interactions in the LAAPD is present in the pulse-height distributions up to 7 bar. Above that pressure this peak is inside the electronic noise tail. On the other hand, the position of the peak depends only on the LAAPD biasing voltage and the peak is present even for null voltage difference across the MM gap.

We have evaluated the effect of the electric field intensity of the drift region on the charge gain in order to establish good operational conditions, determining the MM operational plateau. In figure 5.5, we depict the MM relative amplitude as a function of reduced electric field in the drift region. We observed that the charge gain and energy resolution are fairly constant over a wide range of electric field values, down to very low values. Even for null or reversed electric fields in the drift region, the MM charge gain is significant. This is due to the penetration of the very intense electric field present in the MM gap into the shallow drift region of this detector. For high values of drift electric field, the MM charge gain may decrease as a consequence of the decrease of the primary electron transmission through the MM mesh, which depends on the ratio between the electric fields in the drift region and in the MM gap. For very low drift fields the drift velocity of the primary electron cloud becomes very low, increasing diffusion and the probability of electron attachment, leading to the loss of primary electrons.

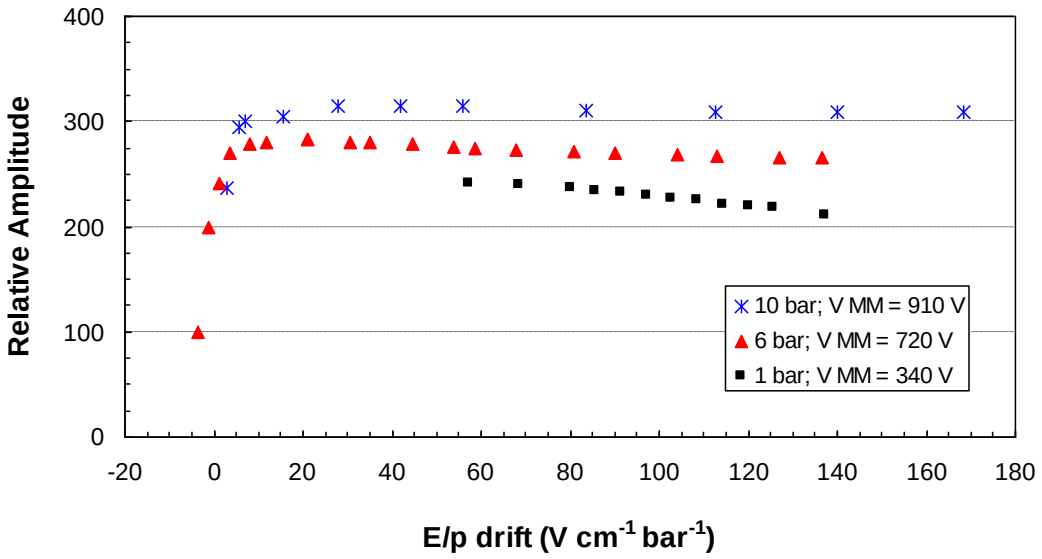

Figure 5.5. MM relative amplitude as a function of reduced electric field in the drift region.

5.3.2.1. Gain

Figure 5.6 shows typical gain curves obtained with the present MM as a function of MM biasing voltage, for both charge and scintillation readout channels, figures 5.6 (a) and 5.6 (b), respectively, and for different filling pressures. The MM biasing voltage was increased until a first discharge occurred and the run was ended. For the scintillation readout channel, the photosensor charge amplification gain was 30. From this value and from the quantum efficiency of the LAAPD it is possible to determine the number of photons hitting the LAAPD, as it will be discussed ahead.

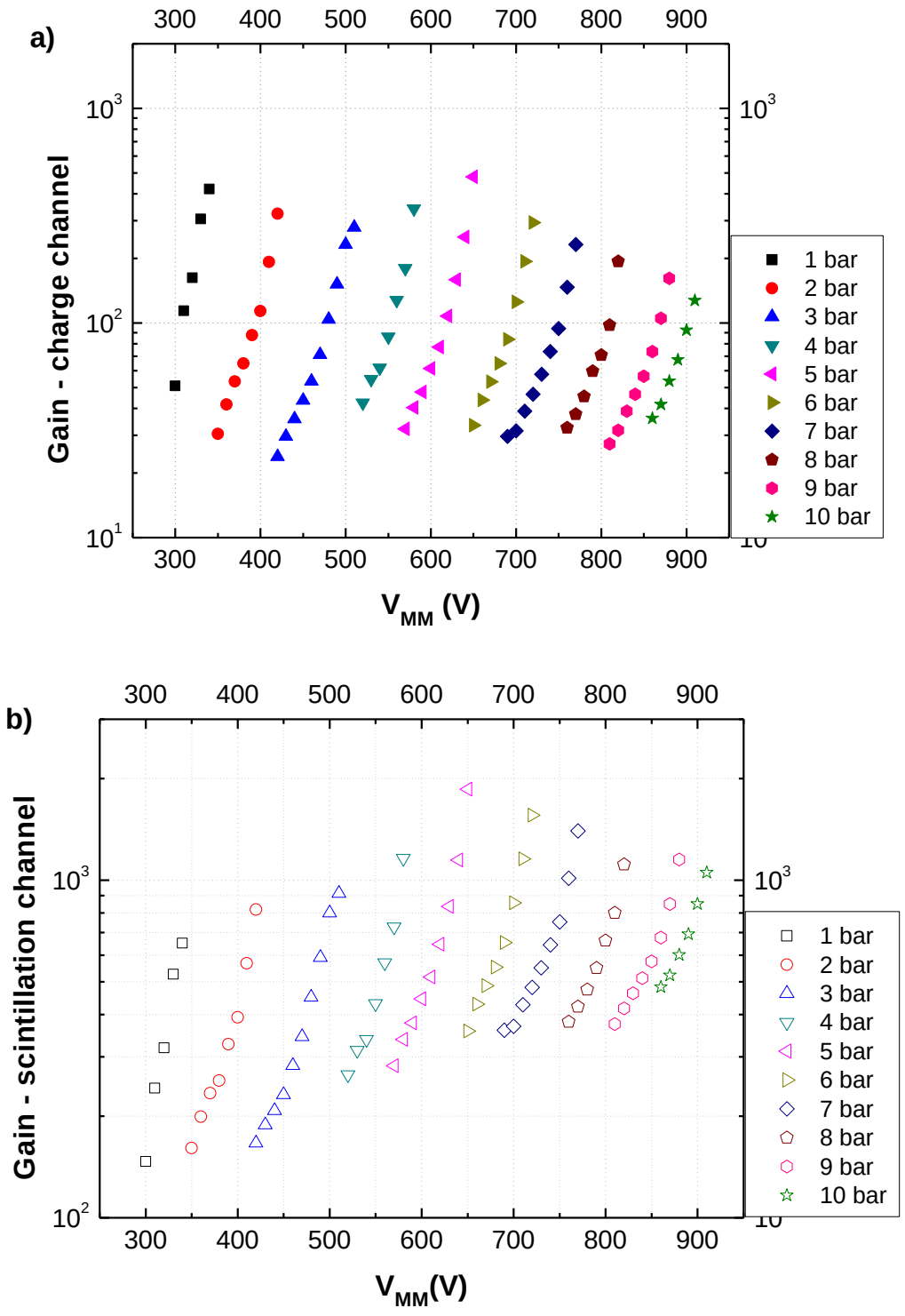

Figure 5.6. MM charge gain (a) and total charge amplification gain of the scintillation channel readout (b), as a function of MM biasing voltage.

Figure 5.6 (a) shows that the maximum absolute gain of the charge readout channel presents only a small dependence with pressure, increasing within a factor of two up to 5 bar and decreasing slowly above this pressure. The maximum gain achieved at 10 bar is still above 100 and it is only four times less than the highest gain. This behavior is in opposition to other micropattern gas electron multipliers, where the charge gain of electron avalanches presents a fast decrease with pressure, with a reduction of few orders of magnitude. These results evidence a notable characteristic of MM and its potential to be used for high pressure operation. This is clearly shown in figure 5.7 where the maximum achieved gain in MM is depicted as a function of pressure, together with the maximum gains obtained for triple-GEM [8], MHSP [9], GEM [10] and THGEM [11]. Although at 1 bar The MM is the microstructure presenting the lowest gains, in xenon, as the pressure increases the MM gain becomes higher than that obtained with the other microstructures, figure 5.7.

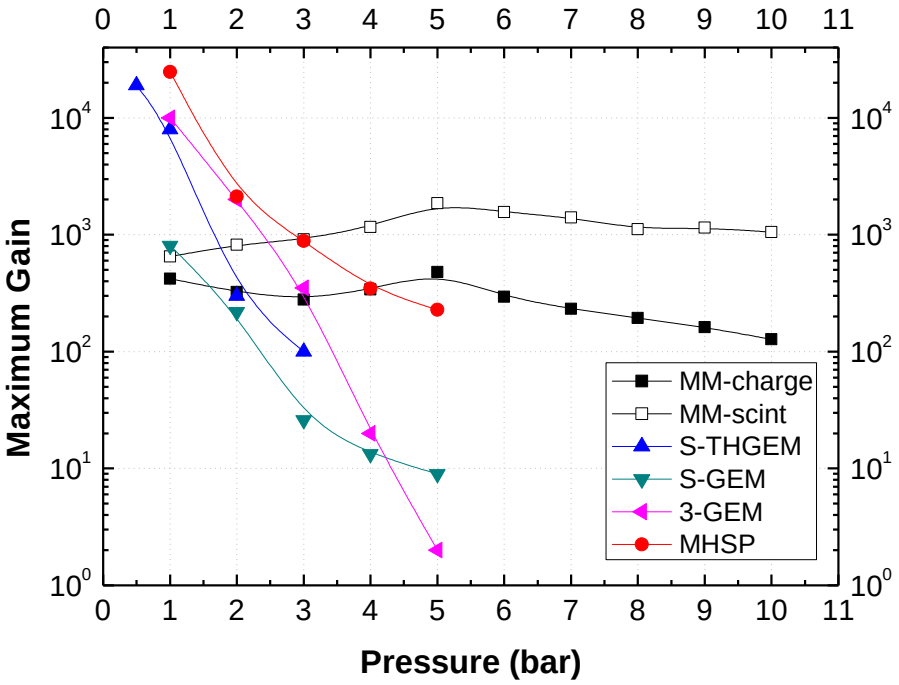

Figure 5.7. Maximum gains obtained with the MM for both charge and scintillation readout channels as a function of pressure in the 1 to 10 bar range. For comparison the maximum gains obtained with other micropattern gas electron multipliers are also depicted as a function of pressure: triple-GEM [8], MHSP [9], GEM [10] and THGEM [11].

The maximum gain achieved in the scintillation readout channel presents an even smaller dependence with pressure, increasing by a factor of 3 up to 5 bar and, then, decreasing within a factor of two up to 10 bar, as shown in figure 5.6(b) and figure 5.7. The scintillation produced by the electron avalanches from GEMs operating in xenon have been also readout by a LAAPD of the same type, presenting a much faster gain reduction with increasing pressure, a factor of 5 in decrease when the pressure increases from 1 to 2.5 bar [19].

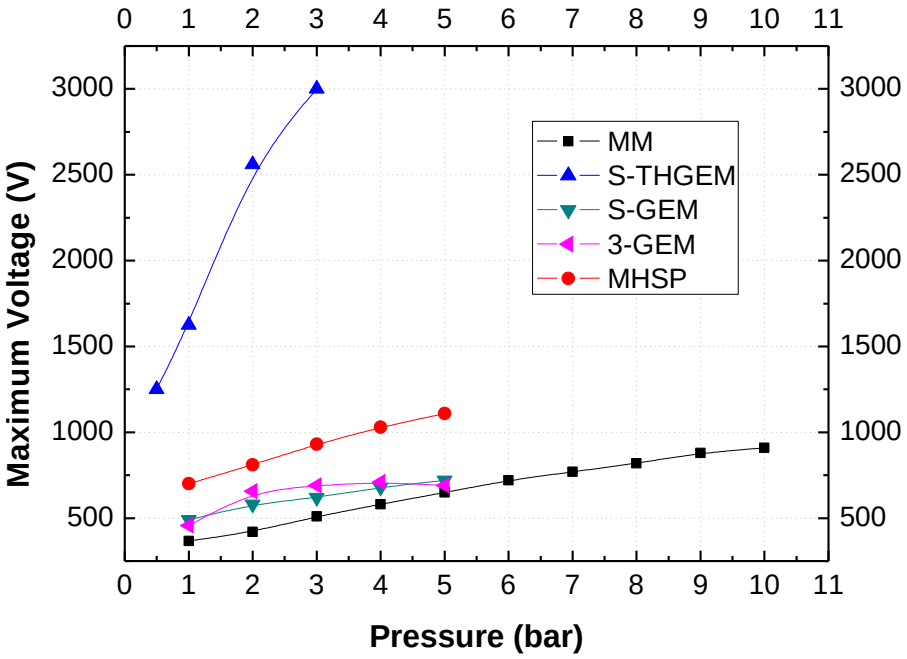

Figure 5.8. Maximum operation voltage as a function of the pressure for the different microstructures.

Figure 5.8 presents the maximum operation voltage that can be applied to the different microstructures as a function of pressure. In single-element multipliers, the maximum applicable voltage steadily increases with pressure, being the MM the microstructure withstanding the lowest voltages, but delivering higher charge gains for pressures above 3-4 bar. Studies on the electron avalanche mechanisms have been performed [20,21]. For Xe, the electron avalanche ionisations and excitations are determined by the electron-impact mechanism, which explains the maximum gain drop for high pressures, as the maximum applied voltages do not increase as fast as

pressure, figure 5.8. The present MM withstands maximum voltages that increase a factor of about 2.7 when the xenon pressure presents a 10-fold increase.

Figure 5.9 depicts the charge-to-scintillation gain ratio as a function of the MM biasing voltage for the different xenon pressures. The data is consistent with the trend of the reduced electric field in the MM gap. Higher reduced electric fields favor the gas ionization when compared to gas excitation. Therefore, the charge-to-scintillation ratio increases with the MM bias voltage, for each gas pressure, and decreases with pressure, as the maximum applied voltages do not increase as fast as pressure and, consequently, the reduced electric field decreases with pressure. The gain of the scintillation readout channel is, in any case, less than a factor of 10 when compared to the gain of the charge readout channel, in opposition to GEMs and THGEMs, for the same photosensor conditions [20]. This may be due to the small MM mesh hole diameter, which is half of the gap thickness, limiting the amount of scintillation that can exit the MM.

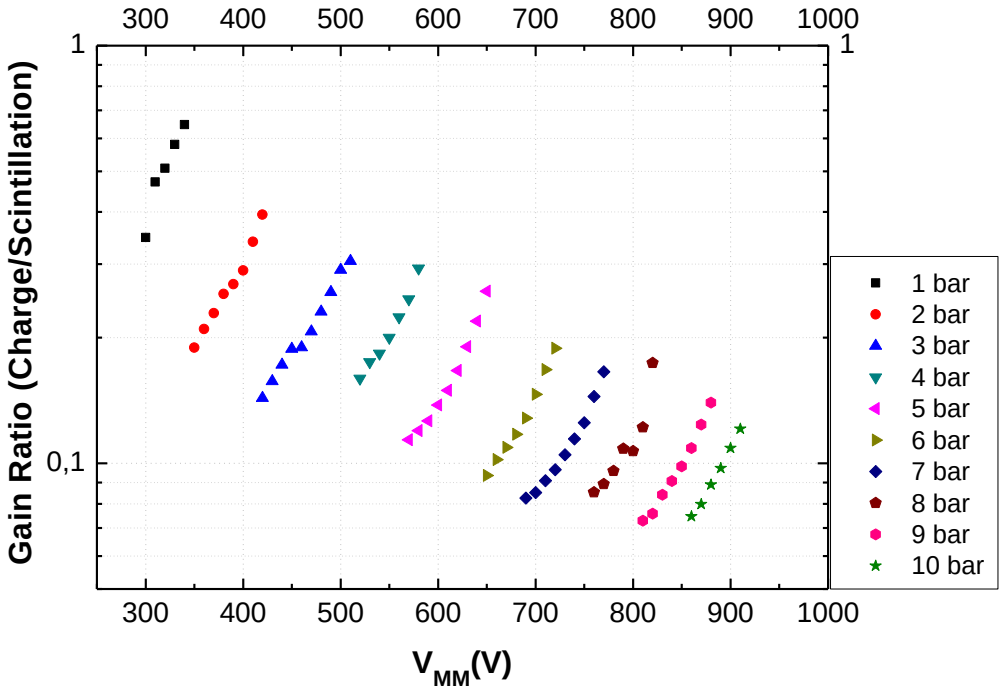

Figure 5.9. Charge-to-scintillation gain ratio as a function of the MM biasing voltage for the different xenon pressures.

5.3.2.2. Energy Resolution

We have studied the energy resolution as a function of the drift electric for different xenon pressures. We found that, similarly to the gain, the energy resolution is fairly constant over a wide range of drift reduced electric field values, down to very low values, figure 5.10. The penetration of the very intense electric field present in the MM gap into the shallow drift region of this detector is responsible to the efficient focusing of primary electrons into the mesh aperture even at very low drift fields.

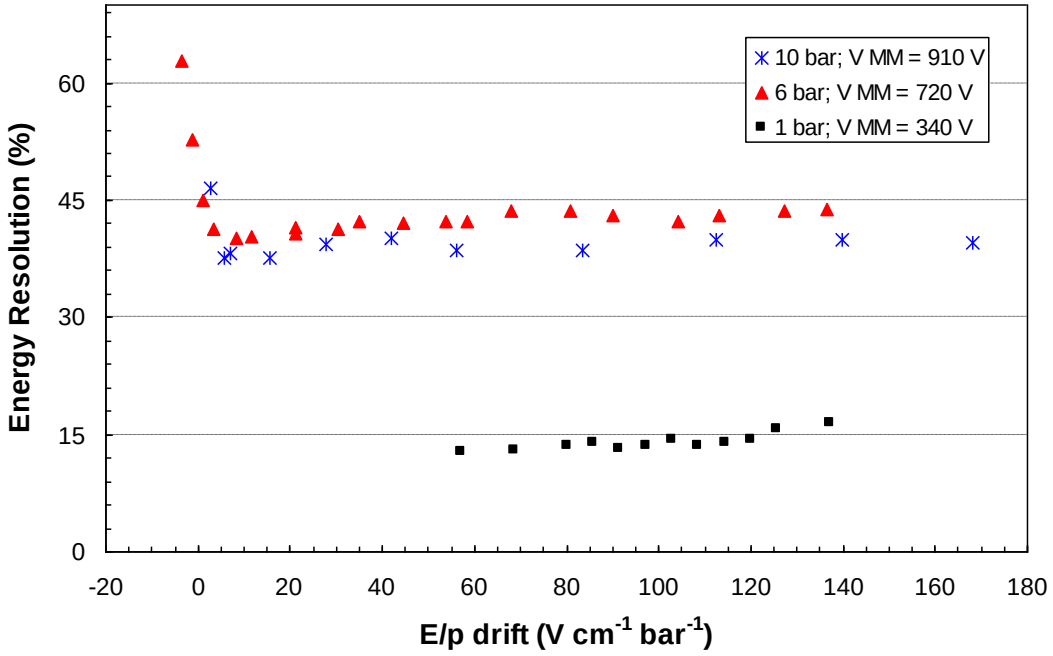

Figure 5.10. Energy resolution of the charge readout channel as a function of reduced electric field in the drift region for xenon pressures of 1, 6 and 10 bar.

Figure 5.11 shows the energy resolution obtained for the 22.1 keV x-rays as a function of the MM biasing for the different xenon pressures and for both charge readout and scintillation readout channels, figure 5.11 (a) and (b), respectively.

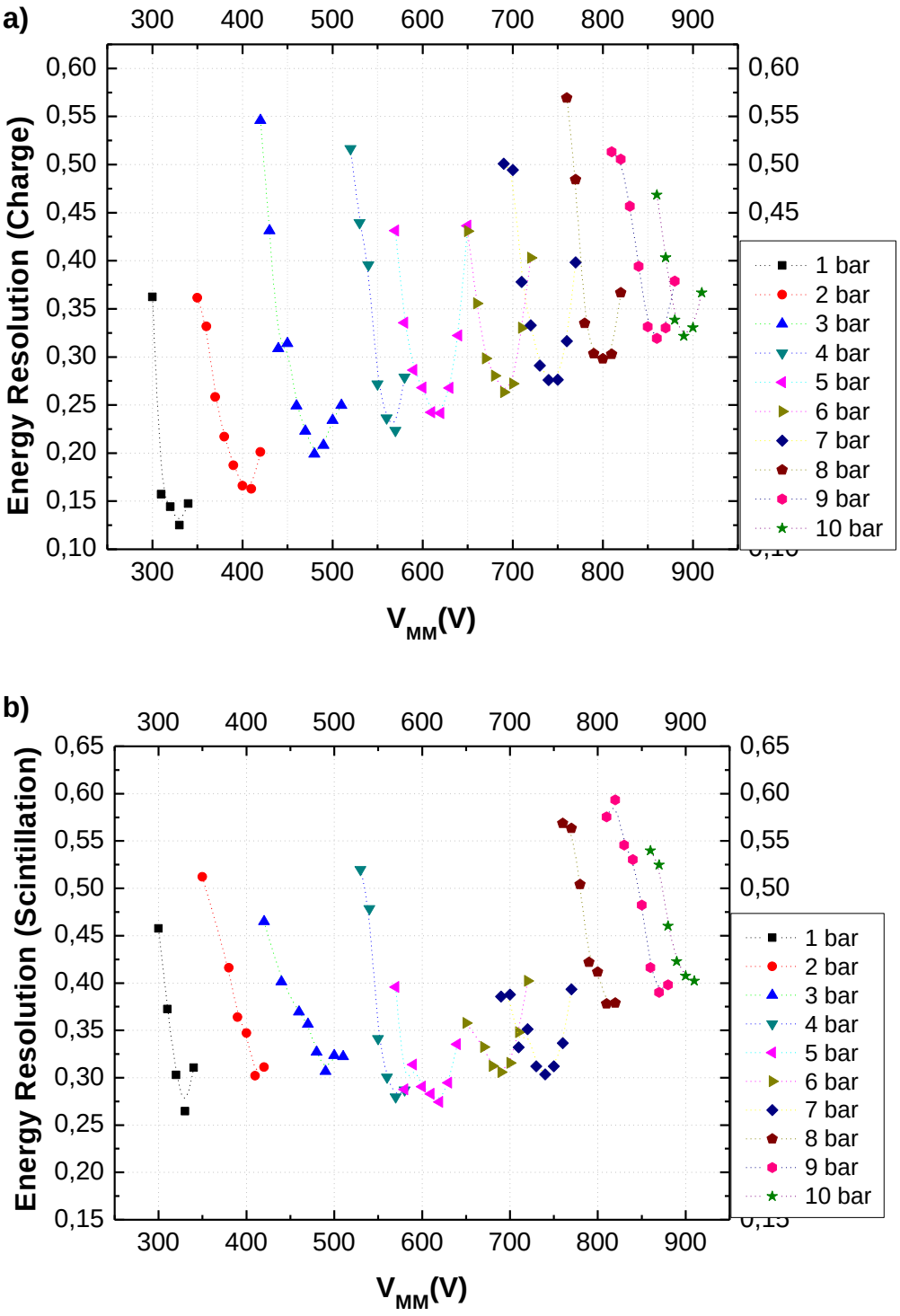

Figure 5.11. Detector energy resolution for the 22.1 keV as function of MM biasing voltage and for the different xenon pressures: a) charge readout channel, b) scintillation readout channel.

For each pressure, the energy resolution presents a fast decrease as the MM biasing voltage increases, reaching a minimum and then increasing again for the highest voltages. This degradation is due to the onset of ion and/or photon feedback effects in the mesh electrode for the highest avalanche gains. This effect is also seen in the gain curves, which present a supra-exponential increase for the higher voltages. On the other hand, the fast increase in the energy resolution for low biasing voltages is due to the poor signal-to-noise ratio.

Figure 5.11 (a) shows that the minimum energy resolution achieved in the charge readout, at each pressure, increases steadily with pressure from 12% at 1 bar to 32% at 10 bar. These energy resolutions are better than those obtained with GEMs and THGEMs. Figure 5.11 (b) show that the energy resolution obtained for the scintillation readout channel is higher than that obtained for the charge readout and presents a different behavior with pressure; the best energy resolution is approximately constant, about 30%, up to 7 bar, degrading to about 40% for the highest pressures.

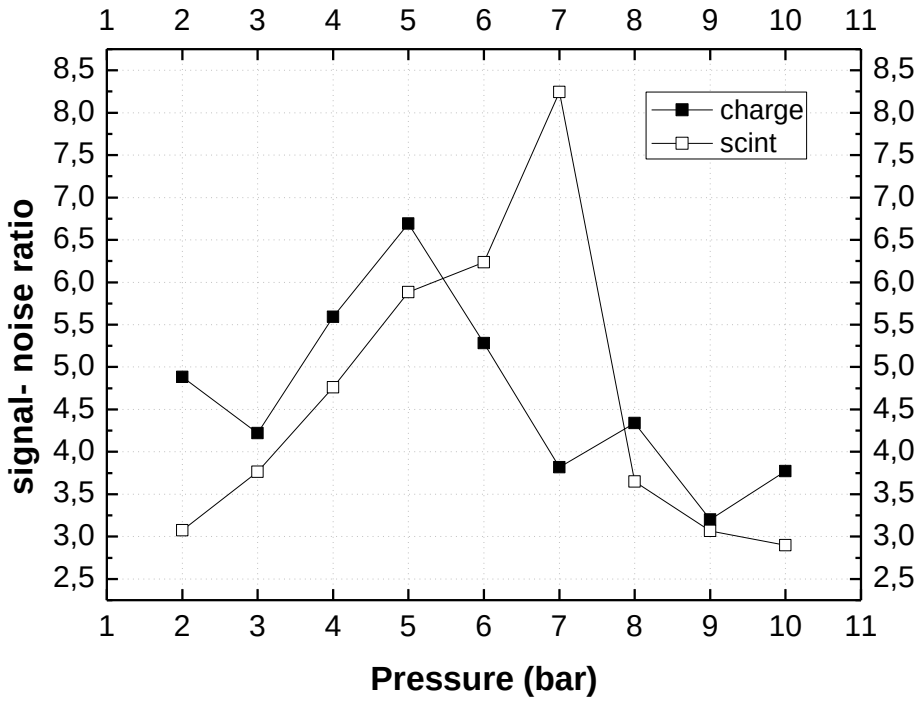

Figure 5.12. Signal/Noise Ratio as a function of pressure for maximum applied voltage in the MM gap.

Figure 5.12 depicts the signal-to-noise ratio, SNR, as a function of pressure, for the highest gains. As shown, given the low gains achieved in the MM, the SNR is low, below 10, being around 3-4 for pressures above 8 bar. However, we have not made much elaborated efforts to optimise the noise.

5.3.3. Scintillation yield

We define the effective scintillation yield of MM, Y_{eff}, as the number of photons that exit from the MM holes per electron produced in the drift region. A certain amount of these photons hit the LAAPD active surface, producing a number of free charge carriers, which are amplified and the resulting charge signal is collected in the LAAPD anode.

The number of photons impinging the LAAPD per x-ray interaction, N_{uv}, is related to the yield through

$$Y_{eff} = N_{UV} \times \frac{2\pi}{\Omega_{Sc}} \times \left(\frac{E_x}{w_{E_x}} \right)^{-1} \quad (5.1)$$

where Ω_{sc} is the solid angle subtended by the LAAPD, E_x is the energy of the incident x-ray and w_{Ex} the respective w-value for xenon. In our conditions, the *w*-value for xenon is 21.77 eV for 22.1 keV x-rays [22] and the relative solid angle subtended by the LAAPD is $\Omega_{sc}/2\pi = 0.12$. N_{uv} can be determined through the pulse-height distributions obtained with the scintillation readout channel, by comparing the centroid of the peak resulting from the full absorption of the 22.1 keV x-rays in the drift region, i.e. resulting from the xenon electroluminescence, A_{Sc}, with the centroid of the peak resulting from the direct absorption of the x-rays in the LAAPD, A_X,

$$N_{UV} = \frac{A_{Sc}}{A_X} \times \frac{N_{e,XR}}{QE} \tag{5.2}$$

where *QE* is the quantum efficiency of the LAAPD, defined as the number of charge carriers produced per incident VUV photon, being 1.1 for 172-nm photons [3,23], and, $N_{e,XR}$ is the number of electron-hole pairs produced by direct absorption of the x-ray in the LAAPD. The latter is determined from the energy of the x-ray and the *w*-value in silicon (*w* = 3.62 eV [25]) and is approximately 6.1×10^3 electron-hole pairs for E_x = 22.1 keV. The dominating source of uncertainty in the calculated yield is QE, which is estimated in ± 10% [16]. This method has been used to determine the xenon and argon electroluminescence yield for uniform electric fields, below and just above the ionization threshold and the electroluminescence yield produced in the GEM avalanches [19,25,26], presenting results that agree with those available in the literature.

The MM effective scintillation yield is shown in figure 5.13 as a function of MM biasing voltage for the different xenon pressures. The total number of photons released by the MM operating in xenon is about 200 photons per primary electron produced in the drift region, at low pressures in the 1- 3 bar range. This is more than one order of magnitude lower than the total number of photons produced in the GEM avalanches [20]. We believe that this difference is due to the fact the present MM has a mesh with holes having small diameter, 25 μm, being most of the scintillation produced in the last part of the electron path in the gap, i.e. almost 50 micron away from the holes. Therefore, the small average solid angle subtended by the mesh holes reduces significantly the amount of scintillation produced in the MM gap that exit through the holes. For xenon pressures of 10 bar the MM effective scintillation yield is just above 200 photons per primary electron.

The calibration of the electronic chain of the scintillation readout channel allows an independent determination of the MM effective scintillation yield. This calibration allows the calculation of the number of electrons collected in the LAAPD anode per primary electron produced in the scintillation region, G_{tot}, i.e. the data presented in

figure 5.6.(b). Assuming the LAAPD gain for the 1650 V bias to be about G_{APD} = 30 [15,16], the number of charge carriers produced by the scintillation pulse can be determined by the ratio of these two gains. Therefore, the number of photons impinging the LAAPD per primary electron, $N_{uv,e}$, can be given by

$$N_{UV,e} = QE^{-1} \times \frac{G_{tot}}{G_{APD}} \tag{5.3}$$

and the MM effective scintillation yield is obtained from

$$Y_{eff} = N_{UV} \times \frac{2\pi}{\Omega_{Sc}} \tag{5.4}$$

The values obtained from Eq. 5.4 are also depicted in figure 5.13 and are similar to those obtained with the former method. However, the uncertainty in the yield obtained by this method is higher, because of the uncertainty in G_{APD} and in G_{tot}, which are larger, than that of *QE*.

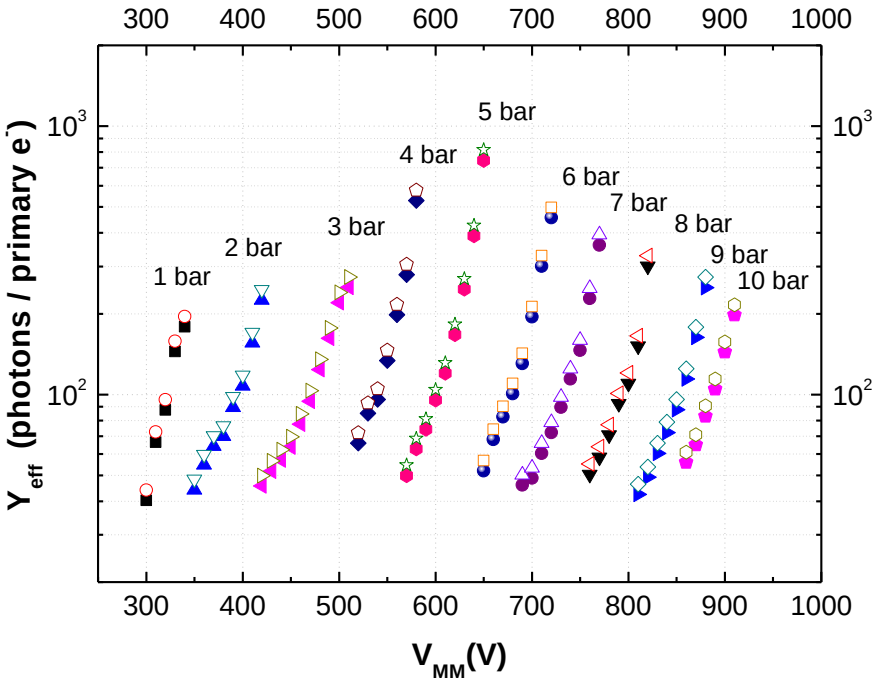

Figure 5.13. Effective scintillation Yield, i.e. number of photons emitted from the MM per primary electron produced in the drift region, as a function of MM biasing voltage. Solid symbols: using direct x-ray interactions in the LAAPD as a reference; open symbols: using the gain calibration of the electronic chain and an LAAPD gain of about 30.

5.4. Conclusions

We investigated the characteristics of the Micromegas electron multiplier operated in Xe, at pressures ranging from 1 to 10 bar. The results exhibit the notable behaviour of MM for high pressure operation. The charge gains are around 4 x 10^2 for xenon pressures up to 5 bar, decreasing slowly above this pressure down to values above 10^2 at 10 bar. Although the gain achieved with the MM at low pressures are much less than those obtained with THGEMs, MHSPs and GEMs, the MM presents the highest gains for xenon pressures above 4 bar. On the other hand, the energy resolution obtained for x-rays of 22.1 keV exhibits a steady increase from 12% at 1bar to about 32% at 10 bar, presenting at 1 bar similar values to those of GEM and substantially better than those of THGEMs. For high pressures the energy resolutions obtained with the MM are better than those obtained with the GEM.

The scintillation produced in the electron avalanches in the MM gap was assessed and the effective scintillation yield, defined as the number of photons exiting through the MM mesh holes per primary electron produced in the conversion region was calculated. This yield is about 2x10^2 photons per primary electron at 1 bar, increasing to about 6x10^2 at 5 bar and, then, decreasing again to 2x10^2 at 10 bar. At 1 bar, the amount of scintillation emitted by the MM is more than one order of magnitude lower than that emitted from GEMs, THGEMs and MHSPs. The readout of this scintillation by a suitable photosensor will result in higher gains but with increased statistical fluctuations.

Concerning the potential application of MM to the NEXT experiment, it is clear that the MM is the only micropatterned structure that can potentially be operated in 10 bar xenon and, therefore, that can be used for the tracking plane of the NEXT TPC. The obtained signal-to-noise ratio shows that the minimum detectable energy can be easily set at few keV, enough for the tracking performance. However, the effective scintillation yield exiting through the holes of the present MM is of the same order of magnitude as the yield produced in the scintillation gap and these two components

will be superimposed, due to the large diffusion in the TPC of the primary electron cloud. This will be a drawback in the use of this MM for the tracking plane for it will degrade the energy resolution of the TPC, which should be optimized to the best possibly achievable. The results also show the unfeasibility of using the present MM as the energy plane of the NEXT TPC, because the energy resolution obtained for the charge readout in the MM is much worse than that obtained for the readout of the scintillation produced in an uniform field gap, without the presence of charge multiplication, either using a PMT or a LAAPD, which may present resolutions below 6% at 10 bar, for 22.1 keV x-rays [27]. The alternative of using the primary electron counting as a technique to readout the event energy, having only the intrinsic statistical fluctuations associated to the primary electron cloud formation, is also unfeasible with the present MM because the gain that could be achieved at 10 bar is too low to be possible the detection of single electrons.

Nevertheless, other MM types aiming to reach much higher gains and much lower energy resolutions in high pressure xenon operation are under implementation [7,28] and will be through similar studies to evaluate its potential applicability to the NEXT TPC.

References

[1] D. Nygren, *Optimal detectors for WIMP and 0-nu beta beta searches: identical high-pressure xenon gas TPCs?*, Nucl. Instrum. Meth. A 581 (2007) 632-642.

[2] K. Yamamoto *et al., Development of Multi-Pixel Photon Counter (MPPC)*, IEEE Nucl. Sci. Symp. Conf. Rec. (2007) 1511-1515.

[3] J.A.M. Lopes *et al., A xenon gas proportional scintillation counter with a UV-sensitive large-area avalanche photodiode*, IEEE Trans. Nucl. Sci. 48 (2001) 312-319.

[4] P.K. Lightfoot, G.J. Barker, K. Mavrokoridis, Y.A. Ramachers and N.J.C. Spooner, *Optical readout tracking detector concept using secondary scintillation from liquid argon generated by a thick gas electron multiplier*, 2009 JINST 4 P04002.

[5] Y. Giomataris, *Development and prospects of the new gaseous detector "Micromegas",* Nucl. Instrum. Meth. A 419 (1998) 239-250.

[6] A. Tomas *et al.*, *Development of Micromegas for neutrinoless double beta decay searches*, 2009 JINST 4 P11016.

[7] S. Cebrian *et al.*, *Micromegas readouts for double beta decay searches*, JCAP 10 (2010) 010.

[8] V. Aulchenko *et al.*, *Further studies of GEM performance in dense noble gases*, Nucl. Instrum. Meth. A 513 (2003) 256-259 and references therein.

[9] F.D. Amaro, J.F.C.A. Veloso, A. Breskin, R. Chechik and J.M.F. dos Santos, *Operation of MHSP multipliers in high pressure pure noble- gas*, 2006 JINST 1 P04003.

[10] A.S. Conceicao *et al., GEM scintillation readout with avalanche photodiodes*, 2007 JINST 2 P09010.

[11] R. Alon *et al., Operation of a thick gas electron multiplier (THGEM) in Ar, Xe and Ar-Xe*, 2008 JINST 3 P01005.

[12] Windowless Large Area APDs, Application notes 1999, Advanced Photonix, Inc., 1240 Avenida Acaso, Camarillo, CA 93012, U.S.A., http://www.advancedphotonix.com/

[13] J.M.F. dos Santos *et al., Development of portable gas proportional scintillation counters for X-ray spectrometry*, X-Ray Spectrom. 30 (2001) 373-381.

[14] S. Andriamonje *et al., Development and performance of Microbulk Micromegas detectors*, 2010 JINST 5 P02001.

[15] L.M.P. Fernandes *et al., LAAPD low temperature performance in X-Ray and visible light detection*, IEEE Trans. Nucl. Sci. 51 (2004) 1575-1580.

[16] R. Neilson *et al., Characterization of large area APDs for the EXO-200 detector*, Nucl. Instrum. Meth. A 608 (2009) 68-75.

[17] C.M.B. Monteiro *et al., Detection of VUV photons with large-area avalanche photodiodes*, Appl. Phys. B 81 (2005) 531-535.

[18] A. Delbart *et al., New developments of Micromegas detector*, Nucl. Instrum. Meth. A 461 (2001) 84-87.

[19] C.M.B. Monteiro *et al., Secondary scintillation yield from gaseous micropattern electron multipliers in direct dark matter detection*, Phys. Lett. B 677 (2009) 133-138.

[20] A. Buzulutskov, *Physics of multi-GEM structures*, Nucl. Instrum. Meth. A 494 (2002) 148-155.

[21] A. Bondar, A. Buzulutskov, L. Shekhtman, R. Snopkov and Y. Tikhonov, *Cryogenic avalanche detectors based on gas electron multipliers*, Nucl. Instrum. Meth. A 524 (2004) 130-141.

[22] T.H.V.T. Dias *et al., Full-energy absorption of X-ray energies near the Xe L-and K-photoionization thresholds in xenon gas detectors: Simulation and experimental results*, J. Appl. Phys. 82 (1997) 2742-2753.

[23] B. Zhou and M. Szawlowski, *An explanation on the APD spectral quantum efficiency in the deep UV range*, Interoffice Memo, Advanced Photonix Inc., 1240 Avenida Acaso, Camarillo, CA 93012, EUA (1999).

[24] G. Knoll, *Radiation Detection and Measurements*, third ed., Wiley, 2001.

[25] C.M.B. Monteiro *et al., Secondary Scintillation Yield in Pure Xenon*, 2007 JINST 2 P05001.

[26] C.M.B. Monteiro, J.A.M. Lopes, J.F. C.A. Veloso and J.M.F. dos Santos, *Secondary scintillation yield in pure argon*, Phys. Lett. B 668 (2008) 167-170.

[27] L.C.C. Coelho, *et al., Xenon GPSC high-pressure operation with a large-area avalanche photodiode readout*, Nucl. Instrum. Meth. A 575 (2007) 444-448.

[28] T. Dafni *et al., Energy resolution of alpha particles in a microbulk Micromegas detector at high pressure Argon and Xenon mixtures*, Nucl. Instrum. Meth. A 608 (2009) 259-266.

6.

HAMAMATSU SIPMS FOR XENON ELECTROLUMINESCENCE DETECTION

In this chapter, we evaluate the performance of several Hamamatsu S10362 MPPCs (S10362-SPL) to the detection of xenon electroluminescence light either by using direct VUV photon incidence or by using Tetraphenyl-Butadienne (TPB), a organic wavelength shifter, in direct coating on these sensors (S10362 series) or using TPB coated glasses placed in front of the photodiodes.

6.1. Introduction

For the unambiguous identification of true ββ events occurring in the TPC of NEXT experiment, it is necessary that we can distinguish these events from background. This can be possible because of their particular topology which makes them distinguishable from background resulting from neutron, alpha and gamma interactions [1]. The electroluminescence signals resulting from the interactions inside the high pressure xenon gas TPC, are going to be detected/recorded by a plane of UV sensitive photomultipliers (PMTs), located behind the TPC cathode, for primary scintillation readout and secondary electroluminescence readout with energy resolution below 1% at the $Q_{\beta\beta}$ (2458 keV) [1], while the pattern recognition will be performed by a

tracking readout matrix/plane of small solid-state sensors, located behind the TPC anode.

Silicon Photomultipliers (SiPMs), also called Multi Pixel Photon Counters (MPPCs), have been the main choice photosensor for the tracking readout plane of the NEXT TPC, in alternative to PMTs, APDs or Micromegas.

The MPPC is a new-type of photon-counting device consisting of multiple APD pixels, connected in parallel, that can operate in two different modes: normal and Geiger mode. The Normal mode is when the reverse voltage applied is set below the breakdown voltage; in this case the MPPC maximum gain is at the order of several hundred. The Geiger mode operation is achieved when the reverse voltage is higher than the breakdown voltage. In this mode, a high electric field is established in the APD and gains of $10^5 – 10^6$ can be achieved, making possible to detect single photon events. Each of these APD pixels, sends a output signal when a photon is detected in that pixel, so that the MPPC output is the total sum of the outputs from all APD pixels [2]. This new-type of device, is suitable for detecting light at the photon-counting level with excellent detection efficiency. Other important advantages of these devices are room temperature and low bias operation (the operating voltage at Geiger Mode is below 100 V), insensibility to magnetic fields, high gain and excellent time resolution, making it suitable for the present purpose.

For tracking purposes, SiPMs offer comparable detection capabilities as standard small PMTs and APDs with the additional advantages of high spatial resolution, ruggedness, radiopurity and cost-effectiveness, essential for a large-scale radiopure detector.

Although SiPMs offer important advantages, they have poor sensitivity in the emission spectrum of the xenon scintillation (~172 nm), needed for the NEXT experiment. So, it is necessary the use of a wavelength-shifter (WLS) to convert the VUV light into a wavelength in the spectral response of the SiPMs (300 to 900 nm) (figure 6.1), or else use VUV-sensitive SiPMs that are under development at Hamamatsu. SiPMs have their optimal detection efficiency, in the region corresponding to visible light (above 50%

photon detection efficiency in the wavelength region of 400-500 nm [2], for the Hamamatsu S10362-33-050C SiPMs).

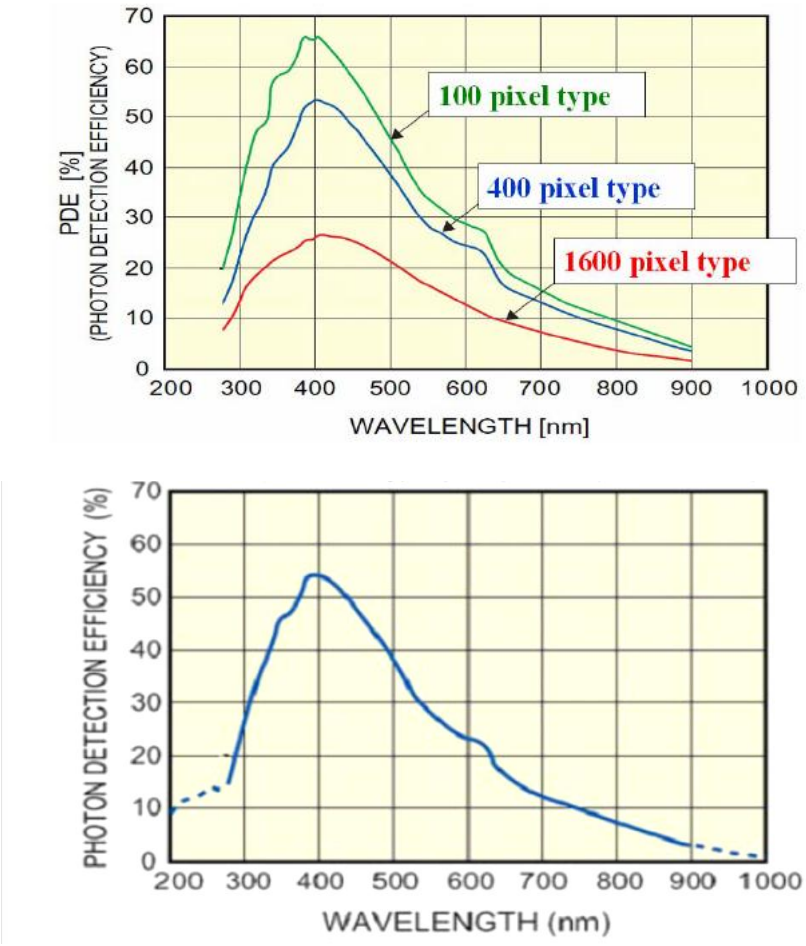

Figure 6.1. SiPM Photon detection efficiency (PDE) dependence on the photon wavelength: (a) S10362-11 series (1x1 mm^2 area SiPM and (b) S10362-33 series (3x3 mm^2 area SiPM) [3,4].

Tetraphenyl-Butadiene (TPB) is an organic WLS that can be used, as its emission spectrum (400-480 nm [5] see figure 6.2) when illuminated by VUV light, is the best match for the sensitivity spectrum of the SiPMs. This organic WLS, was already used in Dark Matter experiments with Liquid Argon (LAr), to coat PMT windows [6,7].

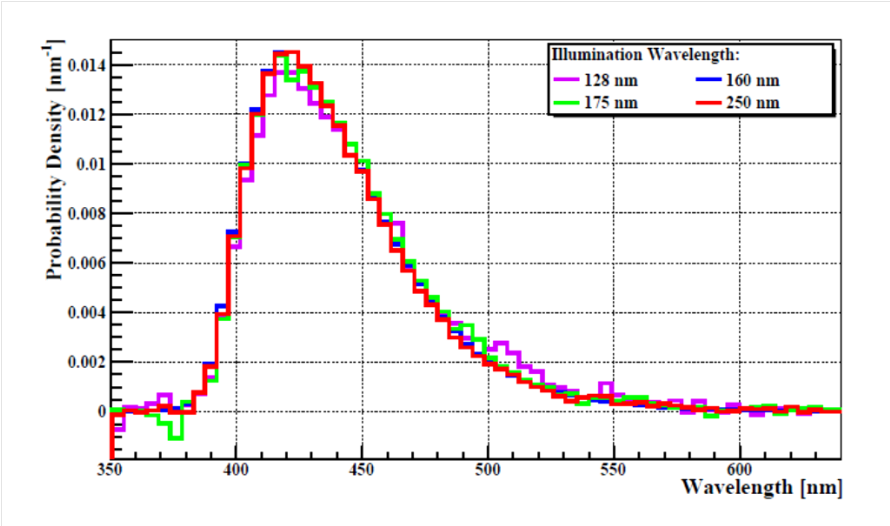

Figure 6.2. Visible re-emission spectrum for a TPB film illuminated with 128, 160, 175, and 250 nm light [5].

The main issues when coating these sensors with TPB are not just the choice of the coating thickness, as this is known to influence the conversion efficiency [8,9], but also the uniformity and the quality of the depositions and also how to ensure in time, the TPB characteristics stability.

Inside NEXT, it was necessary to evaluate the performance of several Hamamatsu S10362 MPPCs to direct xenon electroluminescence light (S10362-SPL) and evaluate the SiPM coated with TPB (directly deposited on the SiPM or by using a TPB coated glass slab covering the SiPMs. In addition, we assessed the stability and/or degradation of the TPB coating when manipulated in air and daylight illumination, which was not known at that time.

6.2. Experimental setup

In this work, we evaluate the performance of Hamamatsu S10362 MPPCs (or SiPMs), with 1 and 9 mm^2 sensitive area, in different configurations of 1, 4 and 5 units, coupled to a GPSC.

As SiPMs are not sensitive to VUV produced by xenon electroluminescence, it was necessary to shift the wavelength of the electroluminescence light, produced by the GPSC, to one wavelength possible to be read by the MPPC. The WLS chosen was Tetraphenyl Butadiene, because the emission spectrum of the TPB is on the sensitive range of the MPPC, it was inexpensive and easy to evaporate. Two alternatives were considered: the direct coating of the SiPM sensors with the WLS and the coating of glass slabs to be place between the electroluminescence region and the SiPMs, ensuring the wavelength shift of the 172 nm from the electroluminescence produced inside the GPSC to a wavelength between 400-480 nm. Several glasses, with different thickness of TPB deposited on them, have been used.

Several configurations of SiPMs were tested coupled to the GPSC. The configurations included SiPM boards, like in figure 6.3, with 4 and 5 MPPCs (S10632-11 series). The SiPMs of the 5 SiPM board were coated with TPB and a Teflon light concentrator was used to maximize the light focusing into each SiPM of the board (see figure 6.4). We found out that the cable of the SiPM board feeding was not vacuum tight and it was necessary to improve the boards used for the SiPMs, also in terms of outgassing. A new design of SiPM board was used and tested, made by Macor (figure 6.5) with 4 SiPM of 1mm^2 area. These SiPMs were not TPB coated and it was tested inside the GPSC with several TPB coated glasses on top of them, with different depositions between 0.05 and 0.2 mg/cm^2.

Figure 6.3. Example of a SiPM board, showing 5 Hamamatsu SiPMs (S10362 - 11 series), each one with 1x1 mm^2 area (a); storage of several SiPM boards and coated glasses with different TPB thickness (b).

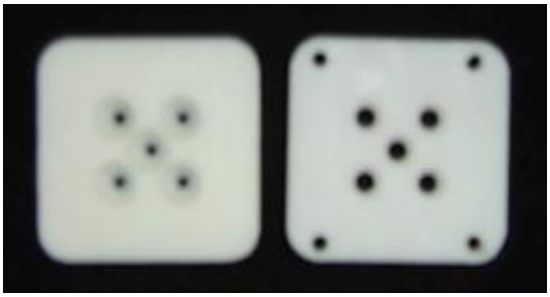

Figure 6.4. Teflon light concentrators, used for focusing the light into the 1mm^2 sensitive area of the SiPMs.

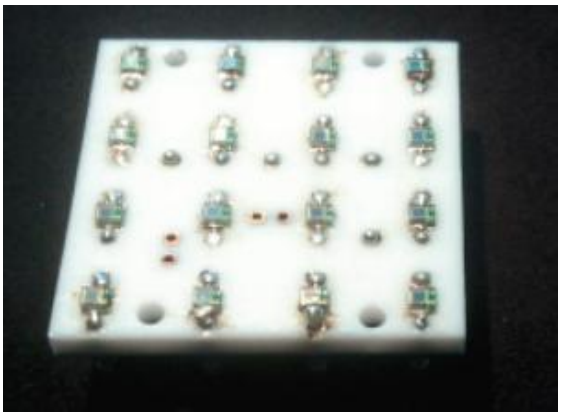

Figure 6.5. Example of a Macor SiPM board, showing 16 MPPCs of 1mm^2.

Figure 6.6 depicts the schematic of the GPSC used in this work, which is similar to that used in Chapter 3 for the studied of Hamamatsu APDs. The radiation window is kept at negative high-voltage -HV0, while mesh G1 and its holder are kept at -HV1; mesh G2 and detector body are grounded. The electric field in the absorption region was kept below the xenon scintillation threshold, throughout the work. The scintillation region is delimited by G1 and G2. In this GPSC prototype, the absorption/drift region and the scintillation region have 4-cm deep and 0.9-cm deep, respectively.

The detector was filled with 1.5 bar of xenon and it was kept constant during each set of measurements. Non-evaporable getter (SAES Getters, St707) purify the Xe by convection, keeping the operating temperature stable in the range of 140-180 ºC.

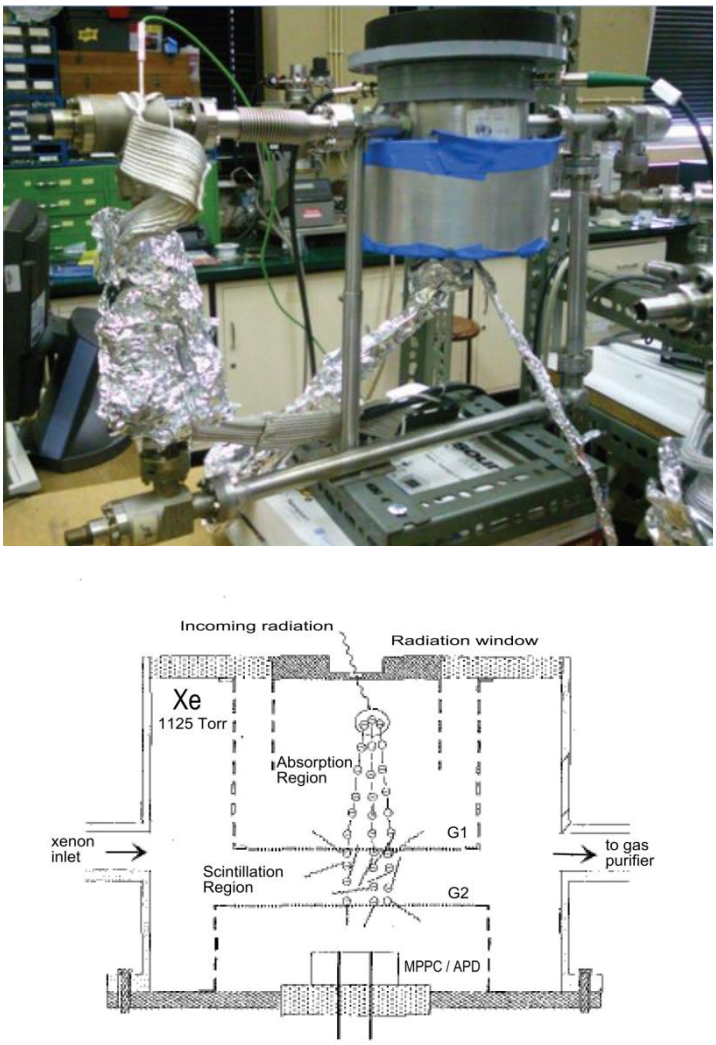

Figure 6.6. Photograph and schematic of the GPSC operation principle.

We used typical values of drift and scintillation electric reduced fields, when operating with the GPSC. We used both ^{109}Cd (22 keV) and ^{241}Am (60 keV) radioactive sources for the incident radiation. We tested two different pre-amplifiers, to fed through the SiPM: one was a lab made Pre-amplifier and the other a CANBERRA 2004.

We didn't see significant changes on the behaviour of the SiPMs, not even an effect on the background noise, during all of our work, even when operating on the Geiger Mode and on the optimal operations conditions of the GPSC.

To make sure that our GPSC was working fine, and to make sure we had electroluminescence inside the detector, we change the MPPC by a sensitive UV APD from Hamamatsu (S10937).

When operating the GPSC with the APD, in the same conditions as the GPSC + SiPM, we observed the presence of electroluminescence light on the APD, figures 6.7 and 6.8.

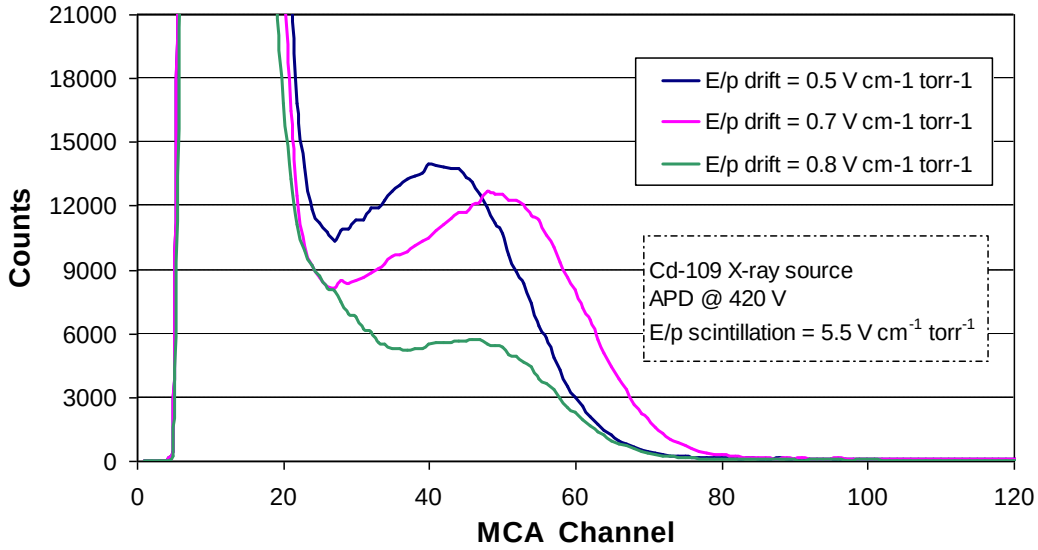

Figure 6.7. Pulse height spectra for different values of reduced drift electric field.

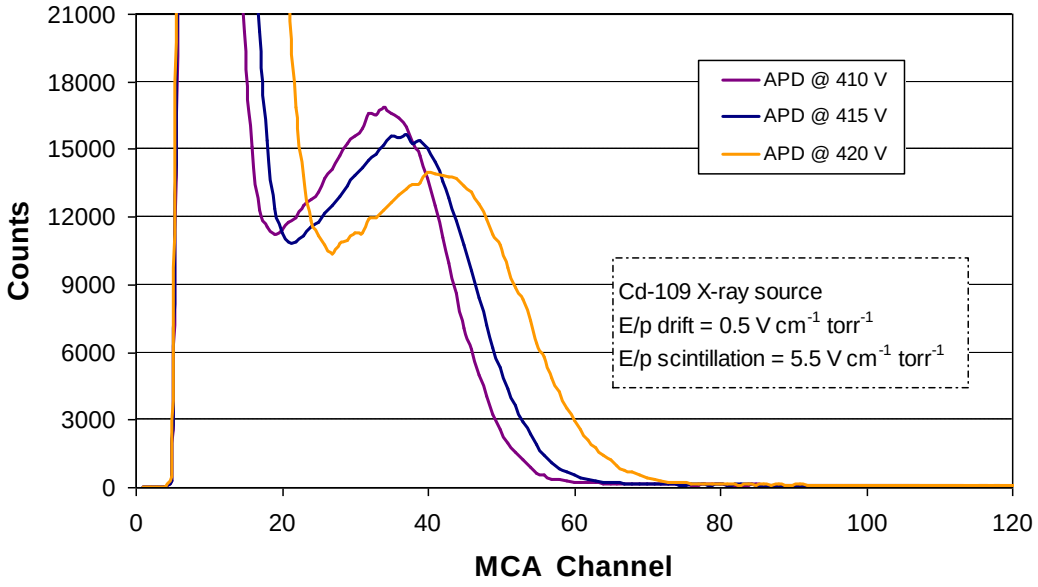

Figure 6.8. Pulse height spectra for different values of APD applied Voltage.

The response of the APD and the performance of the GPSC + APD are below our expectations. This was due to gas impurities due to the poor vacuum insulation of the feedthrough for the SiPMs bias supply and signal readout.

Nevertheless, we could confirm that electroluminescence was being produced in the GPSC but no light conversion was achieved in the TPB. The TPB coating was made at Instituto de Ciencia Molecular (ICMOL), IFIC, Valencia and transported to Coimbra without any special care for the accommodation of the TPB. We have learned in the hard way that handling TPB requires special attention for its protection to light and air, to prevent its degradation.

The investigation was, therefore, pursued in Valencia (IFIC) in a dedicated GPSC.

6.3. Response of coated MPPCs

The response of SiPMs coated with TPB when illuminated with VUV photons was investigated using a xenon lamp coupled to a band-filter for the selection of the Xe scintillation wavelength (173 ± 20 nm). The lamp and the photosensors were enclosed in a glove box filled with N_2, to avoid the absorption of the VUV light by the air. The lamp was placed at a long distance from the SiPM board, so that the light level reaching the sensors was low enough to avoid saturation. The gas box was placed inside a black box to avoid the exposure of the sensors to the ambient light. The current from the SiPMs was recorded with a picoammeter and also through the electronic chain (amplifier, ADC) developed specifically for NEXT tracking system. The Xe lamp was operated in pulsed mode (1 µs pulse width, 100 Hz maximum frequency) and the ADC sampling was performed at a rate of 1 MHz. The signal from the coated SiPMs was amplified and recorded in ADC channels. A typical ADC spectrum showing the response to VUV light of one of the TPB-coated SiPMs is shown in figure 6.9 and compared to the spectrum of a non-coated SiPM.

Finally, a response of the SiPMs to the GPSC electroluminescence could be observed. Figures 6.10 show the response of coated MPPC's placed inside the GPSC prototype at IFIC, using a ^{241}Am radioactive source to produce the primary electron cloud. SiPM signals induced by the electroluminescence pulses could be clearly identified.

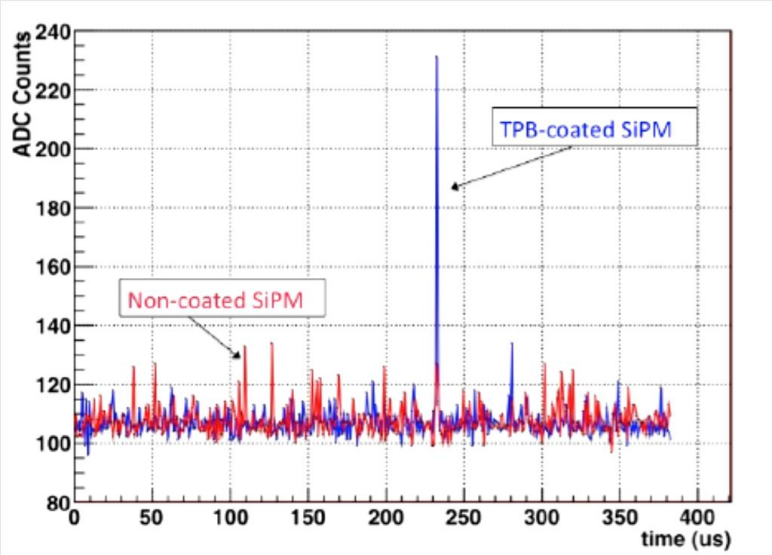

Figure 6.9. ADC spectrum of one SiPM coated with TPB (blue), illuminated with VUV photons, compared to the spectrum from a non-coated SiPM (red).

Figure 6.10. Oscilloscope measurements with a ^{241}Am source.

Once this step was overcome, it was possible for the collaboration to start the studies related with the TPB coating, for improved SiPM response to the xenon scintillation. In

particular, the TPB thickness, response uniformity, handling, accommodation and ageing of the SiPM boards coated with TPB have been carefully monitored [10,11].

6.4. Conclusions

The SiPMs offer important advantages for tracking purposes over other photosensors although they have poor sensitivity to the Xe scintillation. We have shown that TPB degrades when exposed to air and/or to ambient light.

A protocol for coating the SiPMs with TPB, used as WLS, has been developed with particular precautions in obtaining clean and uniform coatings, with optimal fluorescence efficiency. Furthermore, the coated SiPMs have shown a significant and uniform response to the Xe scintillation wavelength (172 nm) compared to the non-coated ones, which are completely non-sensitive to this wavelength. The response of coated SiPMs, after 9 months of storage in a moderate vacuum (< 1 mbar) and in dark conditions, has shown no evidence of ageing effects in the coatings.

References

[1] V. Álvarez *et al.* (NEXT collaboration), *The NEXT-100 experiment for neutrinoless double beta decay searches (Conceptual Design Report)*, http://arxiv.org/abs/1106.3630v1

[2] Hamamatsu Photonics Inc.; http://www.hamamatsu.com

[3] K. Yamamoto *et al., Development of Multi-Pixel Photon Counter (MPPC)*, IEEE Nucl. Sci. Symp. Conference Record (2006) vol.2, 1094-1097.

[4] K. Yamamoto *et al., Development of Multi-Pixel Photon Counter (MPPC),* IEEE Nucl. Sci. Symp. Conference Record (2007) vol.2, 1511-1515.

[5] V. M. Gehman *et al., Fluorescence Efficiency and Visible Re-emission Spectrum of Tetraphenyl Butadiene Films at Extreme Ultraviolet Wavelengths*, Nucl. Instrum. Meth A 654 (2011) 116-121.

[6] V. Boccone *et al., Development of wavelength shifter coated reflectors for the ArDM argon dark matter detector,* 2009 JINST 4 P06001.

[7] P. Benetti *et al., Detection of the VUV liquid argon scintillation light by means of glass-window photomultiplier tubes*, Nucl. Instrum. Meth.A 505 (2003) 89-92.

[8] C.H. Lally, G.J. Davies, W.G. Jones and N.J.T. Smith, *UV quantum efficiencies of organic fluors*, Nucl. Instrum. Meth B 117 (1996) 421-427.

[9] http://www.inficonvacuumcoating.com/en/index.html

[10] V. Álvarez *et al.* (NEXT collaboration), *SiPMs coated with TPB: coating protocol and characterization for NEXT*, 2012 JINST 7 P02010

[11] V. Álvarez *et al.* (NEXT collaboration), *Design and characterization of the SiPM tracking system of NEXT-100 demonstrator, to* be publish as a Technical Report in JINST (2013)

7.

IN SITU CALIBRATION OF PMTS

We have investigated the possibility of calibrating the PMTs of scintillation detectors, using the primary scintillation produced by X-rays to induce single photoelectron response of the PMT. The high-energy tail of this response, can be approximated to an exponential function, under particular conditions. In these cases, it is possible to determine the average gain for each PMT biasing voltage from the inverse of the exponent of the exponential fit to the tail, which can be done even if the background and/or noise cover-up most of the distribution. We have compared our results with those obtained by the commonly used single electron response (SER) method, which uses a LED to induce a single photoelectron response of the PMT and determines the peak position of such response, relative to the pedestal peak (the electronic noise peak, which corresponds to 0 photoelectrons). The results of the exponential fit method agree with those obtained by the SER method when the average number of photoelectrons reaching the first dynode per light/scintillation pulse is around 1.0. The SER method has higher precision, while the exponential fit method has the advantage of being useful in situations where the PMT is already in situ, being difficult or even impossible to apply the SER method, e.g. in sealed scintillator/PMT devices. The exponential fit can also be used to determine the relative gain response of individual PMTs in an array. This can be useful for obtaining correlation coefficients and correct the response uniformity.

7.1 Introduction

The knowledge of the PMT gain can be important in many different situations. Up to the present, PMTs have been widely used as photosensors of scintillation detectors, which are extensively applied to γ-ray spectrometry, particle detection for high-energy physics and rare event detection. The knowledge of the PMT gain allows the determination of the number of photoelectrons released by the photocathode, following the measurement of the total number of electrons collected in the anode. The determination of this number is an important parameter for the studies of the scintillator response to electromagnetic and charged particles and the respective dependence on energy. In particular, the absolute energy dissipated in the scintillators, is related to the number of the photons produced, which in turn is related to the number of photoelectrons emitted by the PMT photocathode.

An effective method for the PMT gain determination is achieved obtaining the PMT response to single photoelectron (SER) [1-3]. Usually, a LED is used to illuminate the PMT at very low light intensity in order to induce a single photoelectron response of the PMT. The position of the charge peak produced by single photoelectron emission is measured relative to the position of the pedestal peak (the electronic noise peak, which corresponds to zero induced photoelectrons). If the amount of light is small enough the single photoelectron emission is dominant over the multiple photoelectron emission cases. The peak distribution associated to events resulting from a given number of photoelectrons reaching the first dynode can be approximated to a Gaussian and the relative position of the centroid of this Gaussian presents a linear increase with the number of photoelectrons hitting the first dynode, while the value of the Gaussian area, which is related with the probability for the corresponding event, obeys to a Poisson distribution [1-3]. Therefore, either the SER is deconvoluted in order to determine the position of the peak corresponding to events with a single photoelectron emission, or the amount of the LED light hitting the PMT is reduced to a point where the probability of having multiple photoelectron emission is less than few

percent, when compared to the probability for the single photoelectron emission. In this case, the photoelectron peak in the charge spectrum is well described by a single Gaussian function. In many experiments, the PMT Gain is measured before assembling (e.g. see [4]) or even by placing one or more LEDs and/or optical fibres inside the detector, in order to allow the monitoring of the PMT gain with time, along the experiment (e.g. see [5]). However, there are many cases where the PMT is inside a sealed chamber inaccessible to a LED light, such is the case of most scintillation detectors, being impossible to use the above method.

In this work, we have investigated the possibility of calibrating a PMT of a scintillation detector using the primary scintillation produced by the radiation interaction in the scintillator. If the primary scintillation induces a single photoelectron response of the PMT that could be approximated to an exponential function in the high-energy region of this response, the PMT average gain can be determined from the inverse of the exponent of the exponential fit. The approximation of the PMT single electron response to an exponential-like distribution has already been done in the literature [6-10].

7.2. Experimental setup and method

The detector used in this work, described in detail in chapter 4, was built to study the performance of a Hamamatsu R8520-06SEL photomultiplier for readout primary and secondary scintillation produced as a result of X-ray absorptions in xenon, at room temperature [11]. The GPSC schematic is presented in figure 7.1 and it was described in chapter 4.

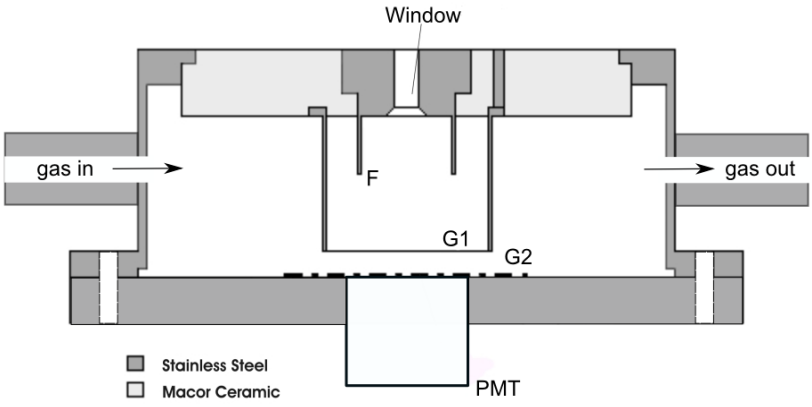

Figure 7.1. Schematic of the xenon GPSC with a R8520-06SEL PMT used as VUV scintillation photosensor.

The GPSC body is made of stainless steel. The R8520-06SEL PMT was glued with low vapour pressure epoxy (TRA-CON 2116) to the anode plane, the bottom base of the GPSC body as shown in figure 7.1. The GPSC upper base is a Macor disk having an aluminized Kapton X-ray window insulated from the detector body. The Macor is glued to the X-ray window holder and to the GPSC body using the epoxy already referred above. The bottom base is vacuum sealed to the GPSC upper part by compressing an indium gasket, allowing detector disassembling when necessary. The drift/conversion region is 3 cm long and it is located between the window and mesh G1, while the electroluminescence gap, 0.5 cm thick, is located between mesh G1 and the anode plane (mesh G2), placed on top of the PMT quartz window.

A ^{55}Fe radioactive source is positioned outside the chamber, on top of the detector window and a 1mm diameter lead collimator. A thin film of chromium was placed between the radioactive source and the collimator to efficiently reduce the interactions of 6.4 keV X-rays (Mn K_β line) in the gas volume. Primary scintillation resulting from the 5.9 keV X-ray interactions is produced in the xenon during the formation of the primary electron cloud. The amplitude of the primary scintillation pulses is very low, difficult to distinguish from the noise or background pulses.

Figure 7.2(a) depicts the pulse-height distribution recorded in the MCA for the primary scintillation resulting from 5.9 keV X-rays interactions in xenon, with no electric fields applied to the GPSC drift and scintillation regions. In order to access the contribution of background pulses resulting from the PMT dark current and/or from residual visible light entering the chamber, energy spectra with and without X-ray irradiation were recorded. This way, the pulse-height distribution for that background could be identified and subtracted from the raw spectrum. The count rate of this background decreases by improving the light shielding of the detector. In figure 7.2(b), is depicted the pulse-height distribution obtained irradiating the detector with 22.1 and 25.0 keV X-rays from a ^{109}Cd radioactive source. As shown, a similar distribution is obtained in the low-energy region, while a broader pulse-height distribution extends towards the high-energy region. This indicates that the pulse-height distribution obtained after the background subtraction has other contributions than the one resulting from the detection of the primary scintillation. We believe that the peak obtained in the low energy region results from luminescence and/or fluorescence of the detector materials, including the PMT, induced by the presence of the X-ray and/or VUV photon interactions. The distribution due to the primary scintillation is superimposed to this fluorescence peak, extending towards the higher energy region.

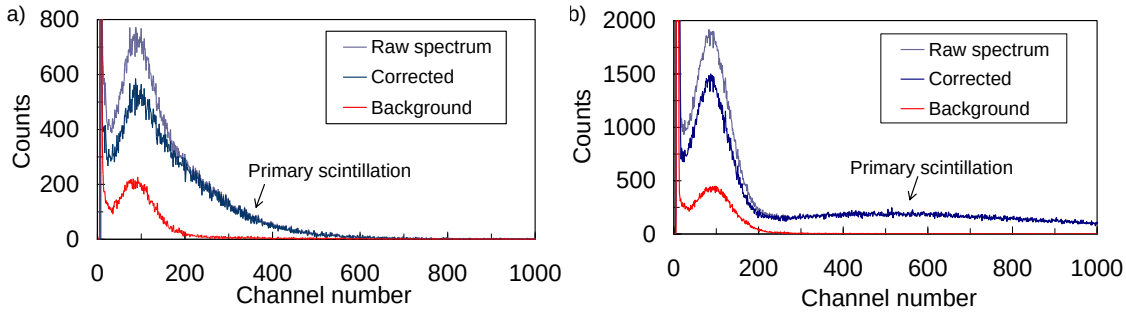

Figure 7.2. Pulse-height distribution obtained in the detector, with no electric fields applied to the drift and scintillation regions and for a PMT bias voltage of 730 V: a) for 5.9 keV X-rays and b) for the X-rays emitted from a ^{109}Cd radioactive source.

Assuming a Gaussian shape for the low energy peak, we can subtract it from the pulse-height distribution in order to obtain the primary scintillation pulse-height distribution as shown in figure 7.3. In chapter 4 we have shown that the primary scintillation is independent of the electric field present on the conversion region and independent of the xenon pressure. In addition, we have measured the Xe primary scintillation yield and the average number of primary scintillation photons hitting the PMT active area per 5.9 keV X-ray absorptions. In average, 82 VUV scintillation photons are produced per 5.9 keV X-ray absorption in the xenon and only an average of 2 of them reach the PMT active area in our setup [11]. Since the quantum efficiency of the present PMT is about 33% for the xenon VUV, the 5.9 keV X-ray interactions in our detector leads to a pulse-height distribution resulting from a single photoelectron response of the PMT.

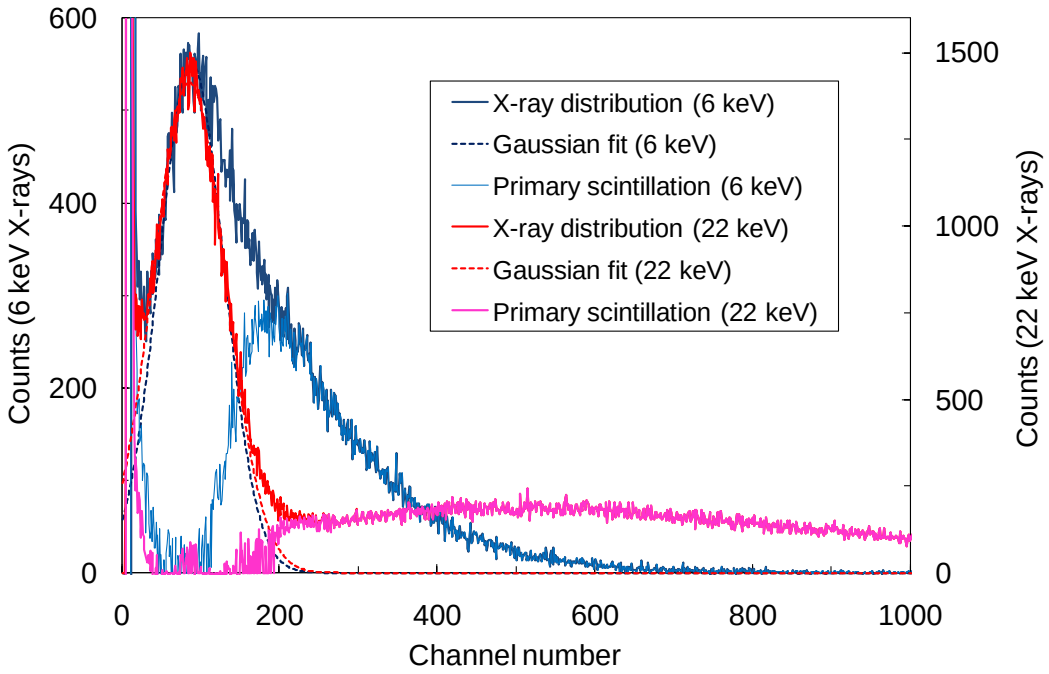

Figure 7.3. Pulse height distribution of the primary scintillation obtained by subtraction of the fluorescence peak, fitted by a Gaussian curve, in the low energy region of the distribution. Both primary scintillation spectra resulting from 5.9 keV and from the ^{109}Cd keV X-ray absorptions in xenon are shown.

7.3 Experimental results and discussion

As shown in figure 7.3, the pulse-height distribution resulting from the primary scintillation of 5.9 keV X-ray interactions and, thus, from a single photoelectron response of the PMT is overlapped by the low energy background peak. Only the tail on the high-energy side of this distribution is not contaminated by this background. Therefore, in this case, it is not possible to determine the PMT gain using the SER method described above. Nevertheless, if we can approximate this tail to an exponential function,

$$P(q) = a\, e^{-\frac{q}{q_{avg}}} \tag{7.1}$$

being q the charge collected at the PMT anode and q_{avg} the average charge obtained from all the primary scintillation events, it is possible to extract the PMT average gain from the exponential fit.

Figure 7.4 depicts the pulse-height distributions of the primary scintillation resulting from 5.9 keV X-ray interactions in Xe, for different PMT biasing voltages. These distributions were obtained after the subtraction of the low energy background peak mentioned above. The solid lines represent the exponential fits to the tail of the pulse-height distributions, in the high-energy region. Figure 7.4 shows that all the tails are very well described by an exponential function and, as the PMT voltage increases, the distributions have a smaller slope and extend to higher amplitudes. The MCA channel number was calibrated in number of electrons using a pulse generator to feed a calibrated capacitor directly coupled to the pre-amplifier input.

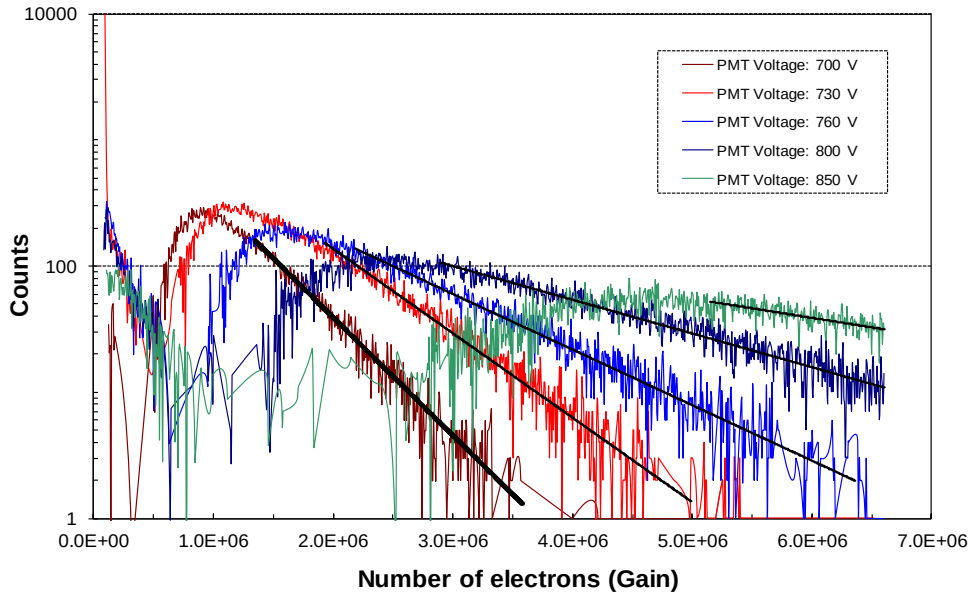

Figure 7.4. Pulse-height distributions resulting from 5.9 keV X-ray interactions in the detector, obtained after the subtraction of the low energy background peak, for different PMT biasing voltages. Solid lines are exponential fittings to the tails.

The experimental results obtained for the PMT gain are depicted in figure 7.5. To confirm the obtained results, we have disassembled the detector and measured the PMT gain using the SER technique. These latter values are also depicted in figure 7.5 for comparison, together with the value measured by Hamamatsu at 800V and supplied in the PMT datasheet. In figure 7.5 we also present the typical gain for the standard R8520 PMT series [12]. In our setup for the studies with the LED, the SER method cannot be applied for PMT voltages below 780 V, because the single-photoelectron peak of the pulse-height distribution gets under the electronic noise (pedestal) peak, while for the exponential tail measurements we can measure gains for PMT voltages lower than 700V. The results obtained using the exponential tail of the primary scintillation agree with those obtained using the SER method within 15%. However, a systematic deviation towards lower gain values is observed. The typical PMT gain value provided by Hamamatsu at 800 V is measured from the ratio of the anode and photocathode currents, which is the product of the interstage gains in the dynodes chain and the collection efficiency of the photoelectrons at the first dynode

[12]. This collection efficiency which is typically between 80 to 100% is not included in the average gain provided by the SER and scintillation methods since we measure the effective charge gain through the dynode chain.

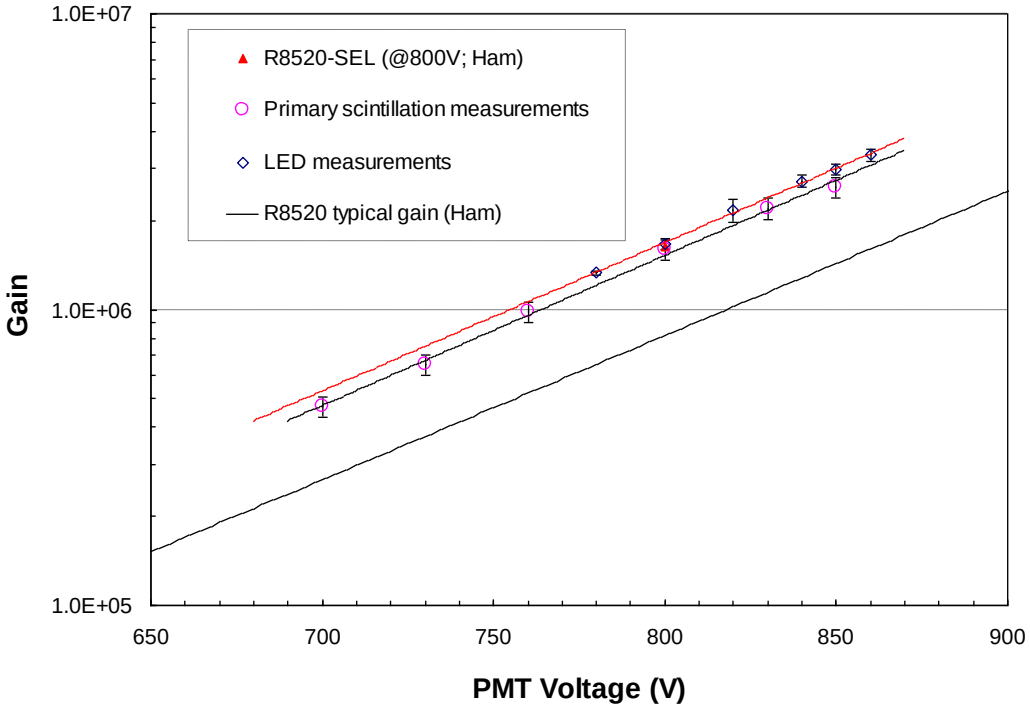

Figure 7.5. PMT Gain obtained using the SER method (blue diamonds) and using the exponential fit to the pulse-height distributions resulting from the detection of primary scintillation (pink circles). Also depicted is the value obtained by Hamamatsu at 800V (red triangle) and the typical gain curve for the standard, (no QE enhanced) R8520 PMT, provided by Hamamatsu [12].

This systematic difference between the SER and the scintillation methods could be due to the different amount of light hitting the PMT in primary scintillation and in LED light measurements. While in the primary scintillation measurements the amount of light hitting the PMT active area corresponds to a photocathode average emission of ~0.7 photoelectrons per scintillation pulse, this number is usually set below 0.1 for the LED light irradiation technique, in order to reduce to a negligible level the contribution of multiple photoelectron emission by the PMT photocathode. Therefore, to understand

the effect of the amount of light detected by the PMT on the measurements using the SER method, i.e. on the determination of centroid of the single photoelectron peak, we have measured the PMT gain versus the PMT biasing voltage for different levels of light emitted by the LED, in order to vary the corresponding average photoelectron emission per light pulse between 0.3 and 1.4. The results are presented in figure 7.6. As shown, the gains obtained by the SER method do not depend on the LED light level, within the studied range. For comparison, the PMT gain obtained by the exponential fit method, using the Xe primary scintillation, is also presented.

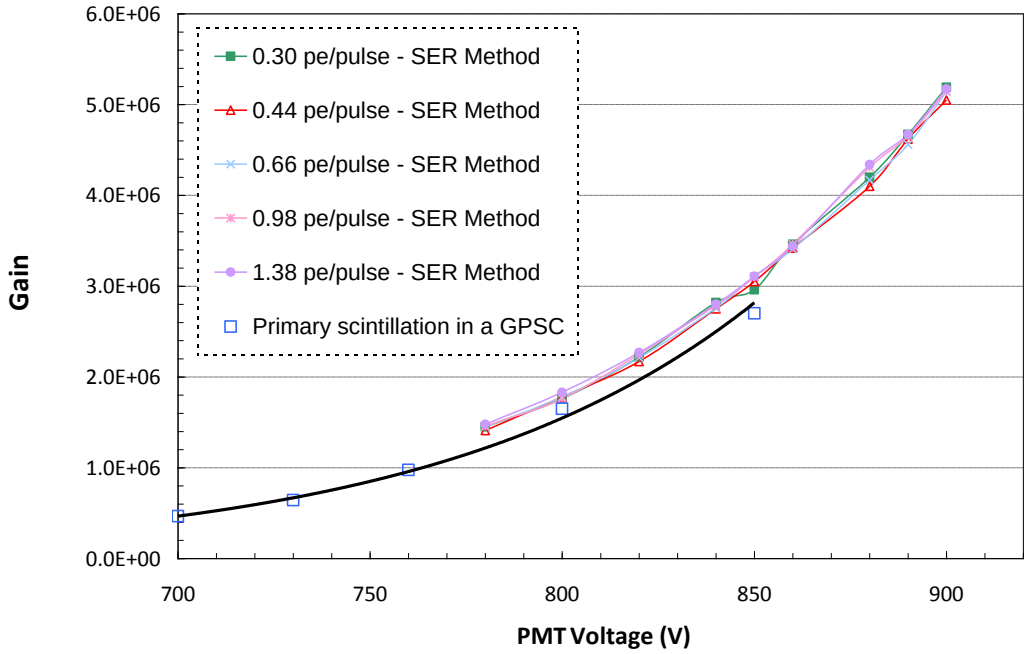

Figure 7.6. PMT gain obtained as a function of the biasing voltage, using the SER method for different LED light levels, corresponding to different average number of photoelectrons emitted by the photocathode. For comparison, the PMT gain obtained by the exponential fit method, using the Xe primary scintillation, is also presented.

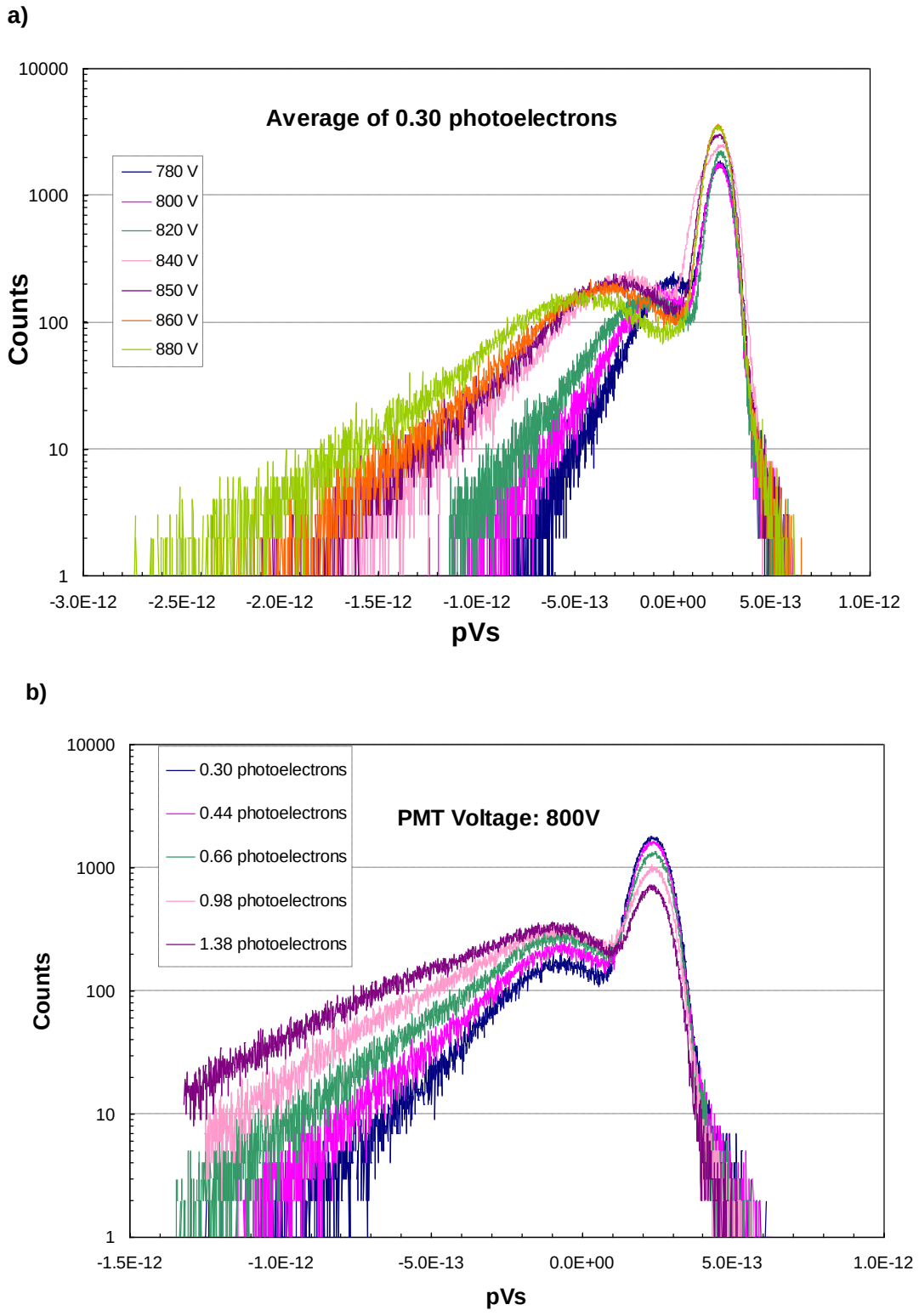

Figure 7.7. SER PMT pulse height distributions: (a) for a constant LED illumination level corresponding to an average of 0.3 photoelectrons emitted by the photocathode per light pulse and different PMT biasing voltages; (b) for a constant PMT biasing voltage of 800 V and different LED illumination levels.

After this study, we have applied the exponential fit method to the pulse-height distributions obtained with the LED irradiation for different PMT voltages and for different LED light levels. Figure 7.7(a) depicts typical pulse height distributions obtained for different PMT biasing voltages and for a LED illumination level corresponding to an average of 0.3 photoelectrons emitted by the photocathode per light pulse. Figure 7.7(b) depicts typical pulse height distributions obtained for different LED illumination levels and a constant PMT biasing voltage of 800 V.

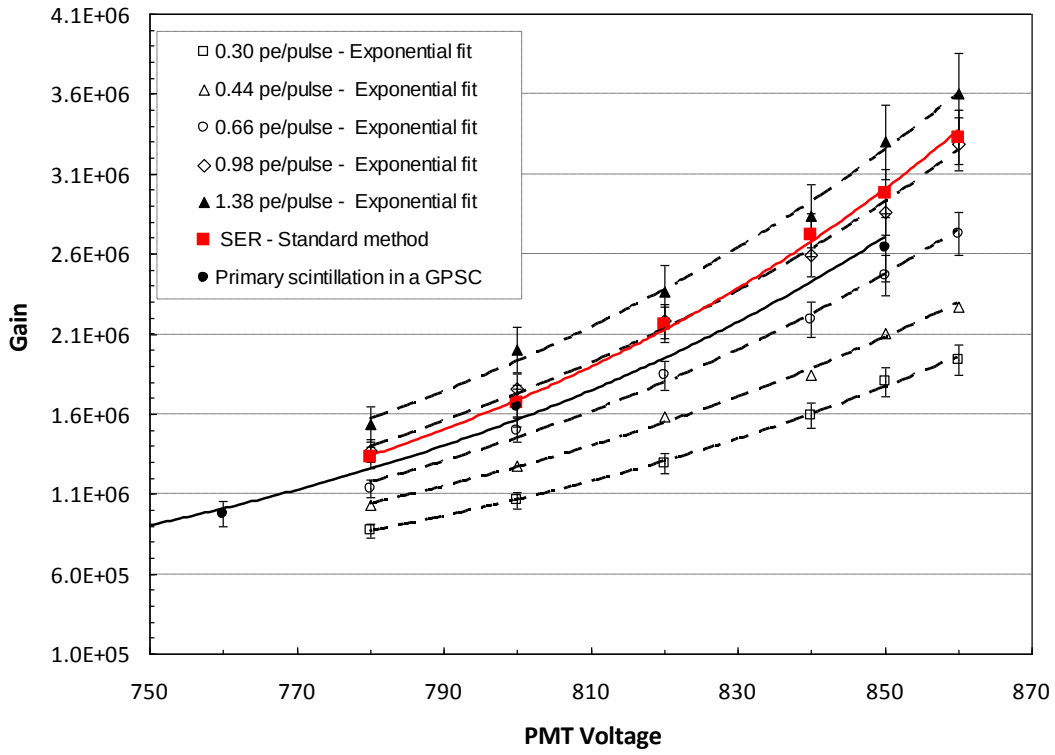

Figure 7.8. PMT average gain as a function of the PMT biasing voltage, obtained by the exponential fit to the tails of the SER pulse-height distributions resulting from the LED illumination with different light levels, corresponding to different average number of photoelectrons emitted by the photocathode. For comparison, the PMT average gain obtained by the exponential fit to the pulse-height distributions from Xe primary scintillation, as well as the PMT gain obtained through the SER single photoelectron peak determination, are also presented.

Figure 7.8 depicts the PMT average gain as a function of the PMT bias voltage for different LED light illumination levels, obtained through the exponential fit to the high-energy tails of the respective SER pulse-height distributions. For comparison, The PMT average gain obtained using the SER method as well as the average gain obtained using the exponential fit to the pulse-height distributions of the Xe primary scintillation induced by 5.9 keV X-Rays are also depicted. As seen, the PMT gain obtained by the exponential fit method depends on the LED light level, i.e. on the amount of light hitting the photocathode. Nevertheless, relative to the gain obtained measuring the single photoelectron peak, the obtained gains are within 20% for LED light levels in a range corresponding to an average of 0.7 – 1.4 photoelectrons amplified in the PMT dynode chain per light pulse.

This is not surprising taking into account that for low light illumination, e.g. below an average of 0.1 photoelectrons collected in the first dynode per light pulse, the SER pulse-height distribution of the PMT is well described by a Gaussian function [1-3], e.g. figure 7.9. As the amount of light illuminating the PMT increases the probability for multiple photoelectron emission increases and the pulse-height distribution consists of the sum of the different Gaussians corresponding to events with different number of photoelectrons hitting the first dynode, figure 7.10. The centroid of each Gaussian presents a linear increase with the number of photoelectrons hitting the first dynode, while the value of the Gaussian area, which is related with the probability for the corresponding event, obeys to a Poisson distribution [1,2]. Therefore, the sum of this multiple Gaussians results in a pulse-height distribution having a high-energy tail that can be approximated to an exponential function.

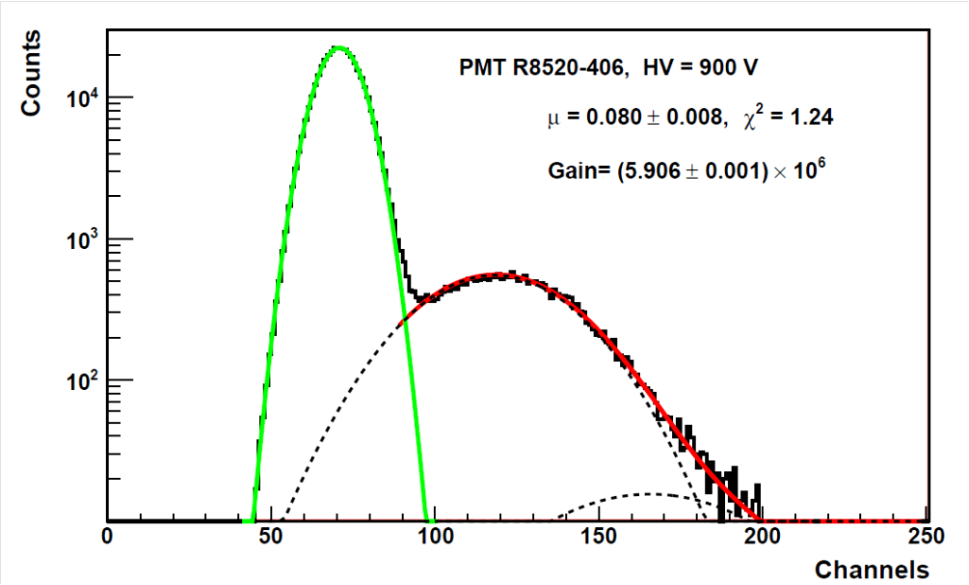

Figure 7.9. Typical PMT SER pulse-height distribution, for a LED illumination level corresponding to an average of 0.1 photoelectrons emitted by the photocathode per light pulse, for a PMT bias voltage of 900 V. The convolution fit to the pulse-height distribution is shown (red line), as well as the pedestal (green line) and the corresponding deconvoluted Gaussians of one and two photoelectron peaks (dashed-lines).

Figure 7.8 shows that if the light pulse induces an average photoelectron emission around 1.0 the tail of the pulse height distribution can be approximated to an exponential function and the PMT average gain can be obtained by the inverse of the exponent of this function. Lower scintillation levels will lead to lower gain values, when comparing to those obtained with the SER method. Nevertheless, the measured gain is still within a factor of two for scintillation levels inducing, in average, as low as 0.3 photoelectrons per scintillation pulse.

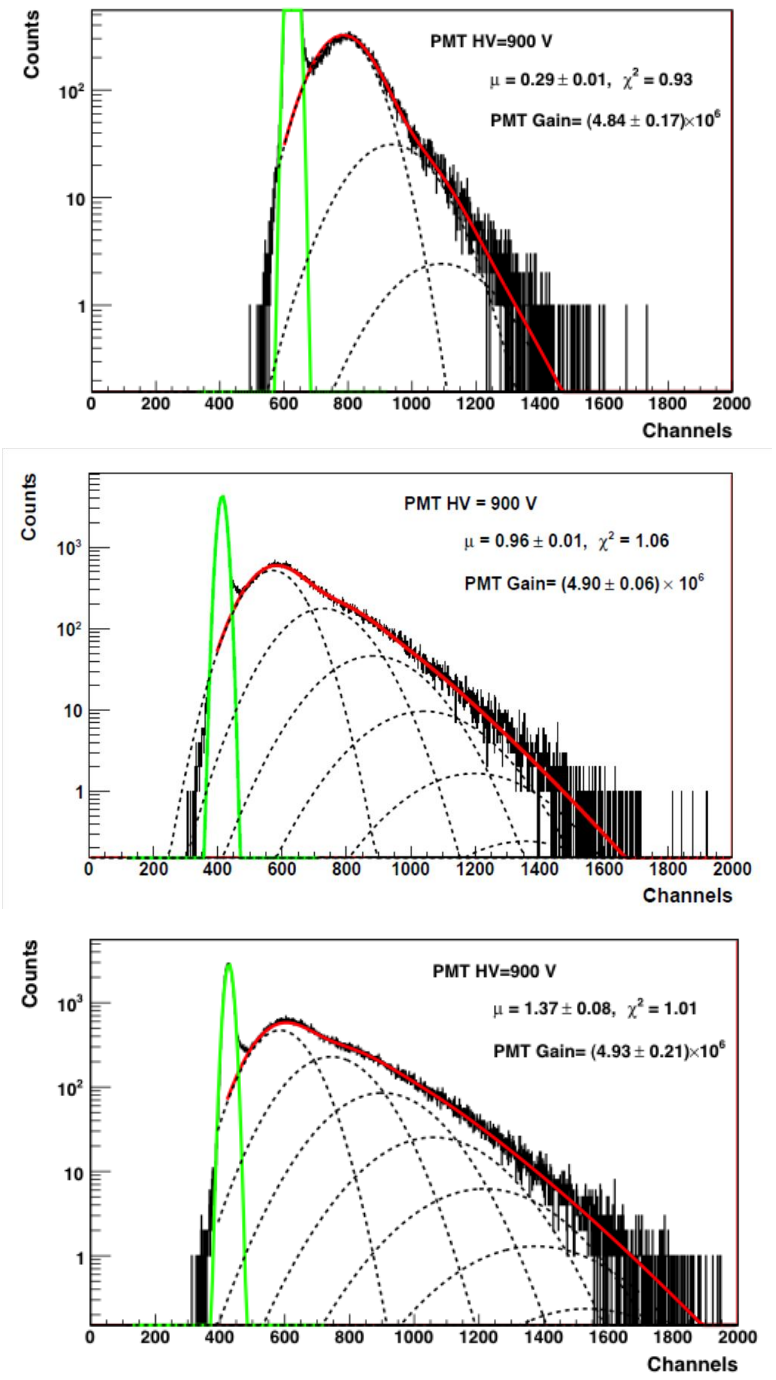

Figure 7.10. PMT SER pulse-height distribution, for a LED illumination levels corresponding to an average of: (a) 0.3, (b) 1.0 and (c) 1.4 photoelectrons emitted by the photocathode per light pulse, for a PMT bias voltage of 900 V. The convolution fit to the pulse-height distribution is shown (red line), as well as the pedestal (green line) and the corresponding deconvoluted Gaussians of multiple photoelectron emission events, one to seven photoelectron peaks (dashed-lines).

7.4. Conclusions

We have measured the average gain of a PMT assembled inside a xenon Gas Proportional Scintillation Counter by registering the pulse height distributions resulting from the primary scintillation light produced in xenon due to 5.9 keV X-Ray interactions. These primary scintillation pulses induce, in average, about 0.7 photoelectrons collected in the PMT dynode chain. The tail of these pulse height distributions were well described by an exponential function, being the PMT average gain given by the inverse of the exponent. The results obtained are consistent but about 15% lower than those obtained using the SER method, i.e. using LED light pulses to induce a single photoelectron response in the PMT and determining the peak of such response relative to the centroid of the noise peak (pedestal).

The present studies have shown that PMT gain calibration obtained through the fit of an exponential function to the high-energy tail of the PMT SER pulse-height distributions is a valid procedure for PMT illuminations within suitable levels, inducing in average around 1.0 photoelectrons per scintillation pulse. Lower scintillation levels will lead to lower gain values, when comparing to those obtained with the SER method. Nevertheless, the measured gain is still within a factor of two for scintillation levels inducing in average as low as 0.3 photoelectrons per scintillation pulse.

In NEXT-DEMO TPC [13], this calibration *in situ* was already successfully used to determine the relative pulse amplitude of the different PMTs and correct for the gain non-uniformity.

This method is very useful when the PMT is assembled and sealed together with the scintillator, like in many scintillation counters, and cannot be removed, being impossible to use the SER method. Also, this method can be used even when the detector background noise is high, covering the single electron response peak, as it was in the present experimental case, since only the high-energy tail is needed.

References

[1] E.H. Bellamy *et al., Absolute calibration and monitoring of a spectrometric channel using a photomultiplier*, Nucl. Instrum. and Meth. A 339 (1994) 468-476.

[2] R. Dossi, A. Ianni, G. Ranucci and O. Ju. Smirnov, *Methods for precise photoelectron counting with photomultipliers*, Nucl. Instrum. and Meth. A 451 (2000) 623-637.

[3] I. Chirikov-Zorin, I. Fedorko, A.Menzione, M. Pikna, I. Sýkora and S. Tokár, *Method for precise analysis of the metal package photomultiplier single photoelectron spectra*, Nucl. Instrum. and Meth. A 456 (2001) 310-324.

[4] A. Bueno, J. Lozano, A.J. Melgarejo, F.J. Muñoz, J.L. Navarro, S. Navas and A.G. Ruiz, *Characterization of large area photomultipliers and its application to dark matter search with noble liquid detectors*, 2008 JINST 3 P01006.

[5] E. Aprile *et al.* (XENON100 Collaboration), *The XENON100 dark matter experiment*, Astroparticle Physics, vol. 35, Issue 9 (2012) 573–590.

[6] G.F. Knoll, *Radiation Detection and Measurements*, 4th Ed., New York, Wiley, 2010, page 283.

[7] J. R. Prescott, *A statistical model for photomultipliers single-electron statistics*, Nucl. Instrum. and Meth. A 39 (1966) 173-179.

[8] F.W. Inman and J.J. Muray, *Variations in single photon pulse height distribution with focusing voltage in photomultipliers*, IEEE TNS 16 (1969) 62-64.

[9] A. Leisos, S. E. Tzamarias and A. Tsirigotis, *Performance of the NESTOR Calibration System*, NESTOR Internal Report HOU-NS-TR-2004-02-EN (2004), http://physicslab.eap.gr/tech_notes/HOU-NS-TR-2004-02-EN.pdf

[10] A.G. Tsirigotis, *NESTOR first results*, Eur. Phys. J. C 33, Supp. (2004) S956-S958.

[11] L.M.P. Fernandes *et al., Primary and secondary scintillation measurements in a Xenon Gas Proportional Scintillation Counter*, 2010 JINST 5 P09006.

[12] Hamamatsu Photonics Inc.; http://www.hamamatsu.com

[13] V. Álvarez *et al.* (NEXT Collaboration), *Initial results of NEXT-DEMO, a large-scale prototype of the NEXT-100 experiment*, 2013 JINST 8 P04002.

8.

CONCLUSIONS

From the electroluminescence readout, of the interactions of 22.1 and 59.6 keV X-rays in a Xe filled gas proportional scintillation counter (GPSC) coupled with a large area avalanche photodiode (LAAPD), it was possible to measured the number of secondary scintillation photons produced per drifting primary electron per unit path length, the xenon electroluminescence yield, as a function of the reduced electric field, for different pressures between 2 and 10 bar. The measurements have shown that the scintillation amplification parameter, i.e. the number of photons produced per drifting electron and per kilovolt, presented a small increase with pressure, increasing from 141±6 at 2 bar to 170±10 at 8 bar and above 8 bar the amplification parameter does not increase; we attribute this effect to non-negligible electron attachment that occurs at higher densities, due to impurities still present in our detector.

The response of the Hamamatsu S8664-SPL APD to the electroluminescence produced within the xenon GPSC and to direct X-rays of 22.1 keV and 5.9 keV, was studied. The best energy resolution achieved was 18% (FWHM) for the 22.1 keV X-rays interaction in xenon. The result for the quantum efficiency of this APD was 69±15% for xenon electroluminescence VUV photons, using a ^{109}Cd source, in agreement to the value given by the manufacturer. This QE makes these devices very attractive for the readout of xenon electroluminescence. On the other hand, the energy resolution achieved is worse than expected and the nominal gain of this type of photosensor is lower, compared to others silicon devices.

The results obtained from the study operation of a Micromegas operating in pure Xe for the pressure range from 1 to 10 bar. The maximum gain achieved was only of few hundreds but the MM showed a notable behaviour when compared to other

microstructures: the maximum gain achieved does not drop significantly with gas pressure. On the other hand, they proved to be unsuitable to be part of the tracking and of the energy plane of the NEXT TPC. Energy resolutions for the charge readout, obtained for x-rays of 22.1 keV exhibits a steady increase from 12% at 1bar to about 32% at 10 bar, worse than that obtained for the scintillation readout using a LAAPD or a PMT, for example. In addition, the charge gains obtained for pressures up to 5 bar, were around 4 x 10^2, decreasing slowly above this pressure down to values somewhat above 10^2 at 10 bar, the gain obtained is too low to be possible the detection of single electrons events. For the tracking capabilities of the MM, the number of photons exiting through the MM mesh holes per primary electron produced in the conversion region, the effective scintillation yield, was calculated. This yield is about 2x10^2 photons per primary electron at 1 bar, increasing to about 6x10^2 at 5 bar and, then, decreasing again to 2x10^2 at 10 bar. This effective scintillation yield is of the same order of magnitude as the yield produced in the scintillation gap and, consequently, it will degrade the energy resolution of the TPC.

From the investigation performed with the Hamamatsu S10362 and S10362-SPL MPPCs, in the detection of xenon electroluminescence light either by using direct VUV photon incidence or by using Tetraphenyl-Butadienne (TPB), a organic wavelength shifter, in direct coating on these sensors or using coated glasses, we have shown that these photosensors are insensitive to the VUV scintillation emitted by xenon and also that the wavelength shifter degrades when exposed to environmental agents, TPB requires stringent storage and operational conditions to prevent its degradation by air or by ambient light.

The performance of the Hamamatsu R8520-06SEL Photomultiplier, at room temperature, for the detection of primary and secondary scintillation produced inside a detector, was evaluated. Primary and secondary scintillation measurements have been carried out, at pressures up to 3 bar. Typical energy resolutions of 8.0% (FWHM) were obtained for the interaction of 5.9 keV X-rays in the xenon, showing the high performance for secondary scintillation detection of these PMTs. Amplitude

measurements of the primary scintillation produced by 5.9 keV X-rays, allowed the determination of the primary scintillation yield in xenon gas, obtaining an average of 81 ± 7 primary scintillation photons produced by 6 keV X-rays absorbed in the xenon. The average energy required to produce a primary scintillation photon in xenon was deduced, resulting W_s = 72 ± 6 eV. The Hamamatsu R8520-06SEL Photomultiplier showed that it is a good candidate for the scintillation readout in the TPC to be used in the NEXT experiment. However the maximum pressure that these PMTs can hold (below 10 bar) is a strong drawback.

Moreover, the possibility of calibrating PMTs, already inside the chamber, by using his response to single photoelectron, was studied. Usually, a LED is used to illuminate the PMT at very low light intensity in order to induce a single photoelectron response, where the gain is given by the relative position of the charge peak produced by single photoelectron emission to the position of the pedestal peak (SER method). The PMT gain was determined, using the primary scintillation produced by X-rays as a single photoelectron source, and the high-energy tail of the PMT response was approximated to an exponential function, where the average gain was determined from the inverse of the exponent of the exponential fit. We have shown that the results of the exponential fit method agree with those obtained by the SER method, being a valid procedure for PMT illuminations around 1.0 photoelectrons per scintillation pulse. Although the SER method has higher precision, the exponential fit method has the advantage of being useful in situations where the PMT is already placed and cannot be removed, when is impossible to apply the SER method or when the detector background noise is high, disturbing the single electron response peak, once only the high-energy tail is needed.

Future work

One of the pending issues in the NEXT collaboration, to be investigated in detail, deals with the possibility of using molecular additives with xenon in the NEXT TPC. Xe is a slow gas, allowing very large electron diffusion. These characteristics are a drawback for the pattern recognition required for the TPC. The addition, in small quantities, of a molecular gas such as CH_4 and CF_4 will have a great impact on the reduction of diffusion and on the increase of the drift velocity.

Recent studies done in Coimbra by Monte Carlo simulation have shown different trends for each gas: while the presence of CH_4 of the order of the percent or below does not have important impact on the electroluminescence (EL) reduction, the addition of CF_4 has a much stronger impact on the EL reduction, even at a level of few tenths of percent. These data has to be confirmed experimentally.

The addition of CH_4 or CF_4 to Xe-filled gas detectors will produce an increase in the electron drift velocity and a reduction of electron diffusion. This can be an asset, when large detectors are being considered and electrons must travel a long drift distance before reaching some kind of amplification stage. On the other hand, NEXT TPC is based on xenon electroluminescence and the presence of additives will reduce the electroluminescence yield.

A compromise must be found between the reduction of the scintillation and the addition of molecular content. Therefore, it is of great importance for the NEXT collaboration to perform these R&D studies.

Two different approaches should be implemented to readout the secondary scintillation in the mixtures, in order to decouple possible electron loss due to attachment during the primary electron drift path from the loss in the electroluminescence yield of the mixture, in order to fully understand the effect of the molecular additive.

Therefore, we plan to built a small driftless GPSC (gas proportional scintillation counter) capable of withstand few bar so to minimize the electron drift effect to a negligible contribution and have only present the effect of the molecular additive on the electroluminescence yield. After knowing correctly and in detail the electroluminescence yield obtained with the different mixtures, next measurements should be done in one of the two prototypes of NEXT-DEMO, which have large drift paths, of several tens of cm, to understand the role of primary electron attachment in the mixture and the consequently loss of secondary scintillation. In alternative, as an intermediary step, a small GPSC prototype with several centimeters of drift region should be used to access the impact of the electron attachment by the molecular additives, prior the tests in the large NEXT-DEMO prototypes.

Appendix A

Non-linear response to X-rays method

For the determination of the non-linear response of the S8664-SPL APD from Hamamatsu, to X-rays direct interactions, the method used, was the one used and described by Moszynski in Ref.[1].

At IFAE, the APD from Hamamatsu was mounted in a gas tight box (figure A.1), flushed with dry gas (N_2). Inside the box a radioactive source is positioned, ^{109}Cd or ^{55}Fe, and also a green LED (wavelength of about 520 nm). The radioactive source and the LED were installed in such a way that the APD could be illuminated simultaneously by both. The APD signal was processed with a charge sensitive ORTEC 142B preamplifier, an ORTEC 673 amplifier and the spectrum was recorded with an 8001A multichannel-analyzer from AMPTEK. During the measurements the temperature was stable within 2ºC.

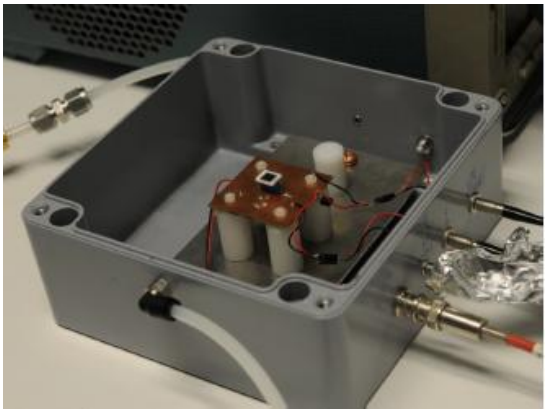

Figure A.1. Box used for the determination of the non-linearity of the APD to X-rays detection.

The method consists by simultaneous monitoring the amplitudes due to the interactions in the APD of the LED light pulses as well as the X-rays from the radioactive sources. The non-linear response can be determined from the ratio of the centroid positions of the LED and the X-ray interaction peaks as a function of the applied voltage (figure A.2). This ratio is also called the quenching factor.

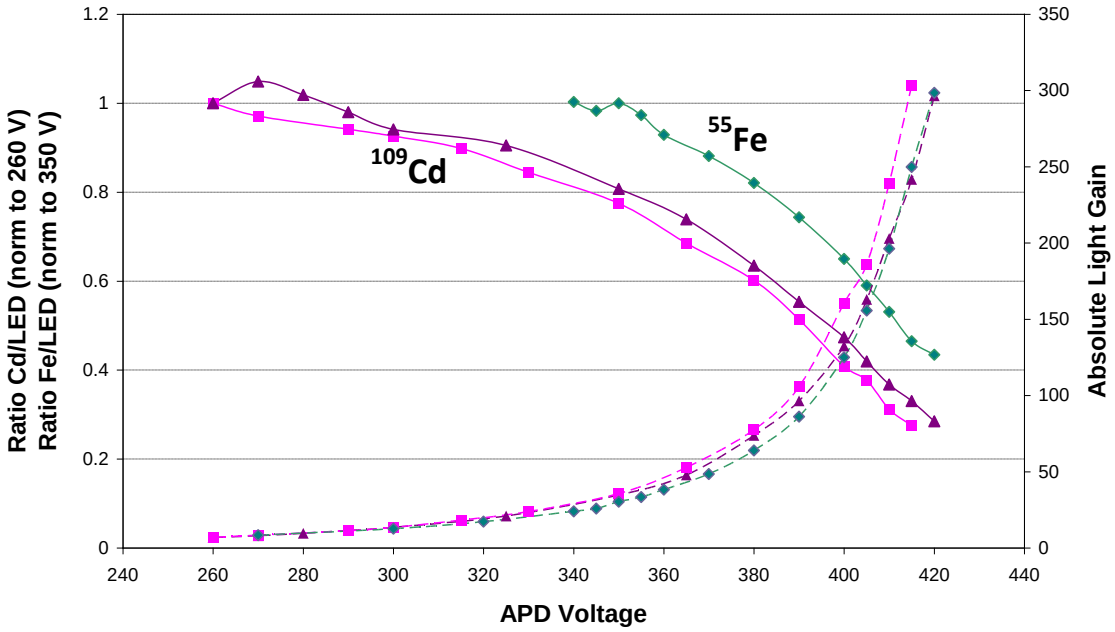

Figure A.2. Ratio of direct X-ray interaction peak position and LED peak position (solid lines) and LED light gain (dashed lines) as a function of the APD bias voltage. The interactions resulting from the 22.1 keV of the ^{109}Cd source are shown for two APDs (purple and pink lines) and are normalized to the values obtained at 260 V (APD bias voltage). The interactions of the 5.9 keV from the ^{55}Fe source (green line) were normalized to the value obtained, when the APD was biased at 350 V.

Figure A.2 shows the X-ray quenching factor and the LED light gain as a function of the APD bias voltage. The light gain was obtained normalizing the peak position of the light pulse to a gain of ~7 as it was obtained for 22.1 keV X-rays interactions for 260 V [2,3] and 350 V for 5.9 keV.

Figure A.3 shows the quenching factor or the non-linearity response dependence on the light gain. The differences between the two APDs (purple and pink lines) for the 22.1 keV x-rays, appear to be negligible because the quenching is caused by local high charge densities in the APD and it should depend only on the gain.

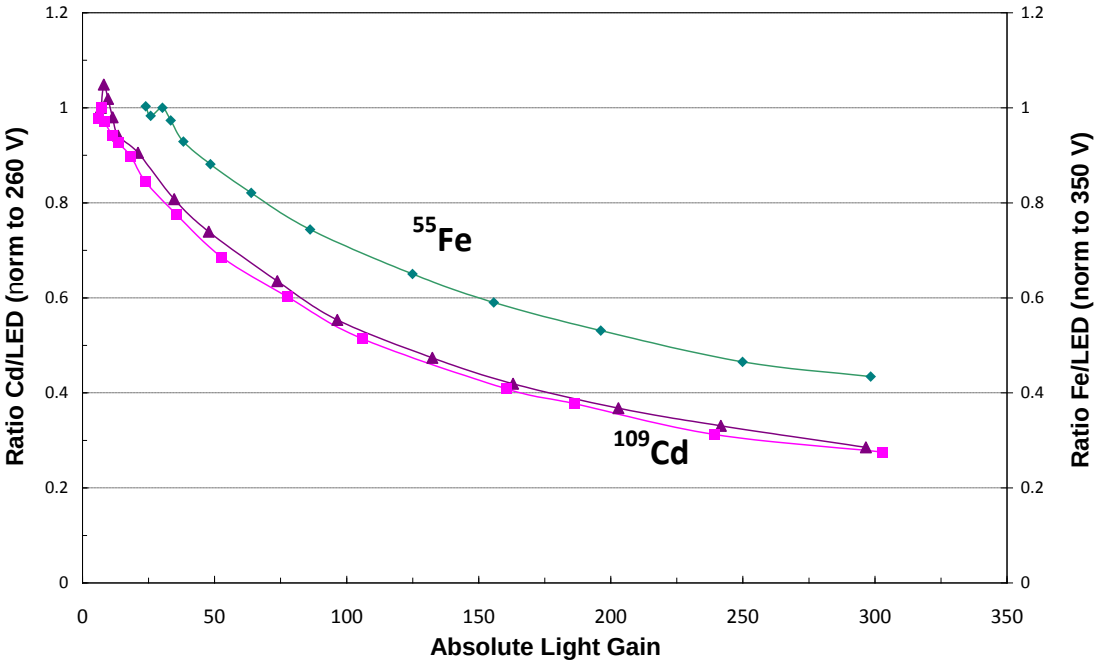

Figure A.3. The X-ray quenching factor as a function of LED light gain. As before the purple and pink lines show the results for 22.1 keV from a ^{109}Cd source for two S8664-SPL APDs, normalized to the value at 260 V, while the green line shows the result for 5.9 keV, normalized to the value at 350 V.

Below APD biasing voltages of 260 V, for 22.1 keV and of 340 V for 5.9 keV X-rays, the APD response for the X-rays direct interactions were superimposed in the noise background. We assume that non-linear effects are negligible below those biasing values, since the ratio between the X-ray and LED amplitudes do not change significantly within a voltage span of 30 and 15 V, for 22.1 and 5.9 keV X-rays, respectively. Also for light gains lower than 20 the variation of the quenching factor is less than few percent, for 5.9 keV X-rays, this is backed up by the literature [2,3].

The non-linearity response factor of this APD for a bias voltage of 415 V, is 0.29±0.04 for 22.1 keV and 0.46±0.07 for 5.9 keV X-rays.

References

[1] M. Moszynski, M. Szawlowski, M. Kapusta and M. Balcerzyk*, Large area avalanche photodiodes in scintillation and X-rays detection*, Nucl. Instrum. Meth. A 485 (2002) 504-521.

[2] T. Ikagawa *et al.*, *Performance of large-area avalanche photodiode for low-energy X-rays and γ-rays scintillation detection*, Nucl. Instrum. Meth. A 515 (2003) 671-679.

[3] T. Ikagawa *et al.*, *Study of large area Hamamatsu avalanche photodiode in a γ-ray scintillation detector*, Nucl. Instrum. Meth. A 538 (2005) 640-650.